# Subgrid-scale heat flux modeling for large eddy simulation of turbulent mixed convection

Zur Erlangung des akademischen Grades
**Doktor der Ingenieurwissenschaften**
der Fakultät für Maschinenbau
Karlsruher Institut für Technologie (KIT)

genehmigte
**Dissertation**
von

M. Sc. Dejan Morar

aus Perlez, Serbien

Tag der mündlichen Prüfung: 08. 12. 2014
Hauptreferent: Prof. Dr.-Ing. Xu Cheng
Korreferent: Prof. Dr.-Ing. Thomas Schulenberg

# Acknowledgements

First and foremost, I would like to express my gratitude to Dr. Ivan Otic and Professor Xu Cheng for accepting me into the PhD program and for their constant support and guidance in my research.

I also would like to thank Professor Thomas Schulenberg for his availability, invaluable comments and suggestions. Without his instructions this thesis could not have reached its present form.

I thank my colleagues from the Institute of Fusion and Reactor Technology for sharing their knowledge and being a source of friendship and help.

I am grateful to my friends for the moments of leisure shared together which helped to overcome some difficult moments.

Finally I would like to thank my family for their love and support during all these years.

Karlsruhe, December 2014

Dejan Morar

# Abstract

Turbulent mixed convection is a mode of heat transfer that combines both forced and natural convection. Temperature field acts as an active scalar, meaning that the momentum and the energy equations are closely coupled. In the numerical study of turbulent heat transfer, the common modeling approach is based on the concept of constant turbulent Prandtl number, $Pr_{sgs}$, which assumes similarity between velocity and temperature fields. However, this approach is insufficient for the flows of fluids whose molecular Prandtl number strongly deviates from one, or if the flow field experiences some additional source terms, e.g. buoyancy or Lorentz forces. When this is the case, alternative closure methods for energy equation should be considered.

In the present work, new subgrid-scale (SGS) model for turbulent heat flux based on the algebraic equations and dynamic procedure for evaluation of model coefficients is developed. The new model explicitly includes the buoyancy production term and is expected to improve quality of Large Eddy Simulation (LES) results for those modes of heat transfer where buoyancy effects play an important role. In addition, a dynamic model for turbulent Prandtl number is also derived. Here, $Pr_{sgs}$ is calculated dynamically in time depending on the flow and heat transfer conditions. Both models are implemented in Computational Fluid Dynamics (CFD) toolbox OpenFOAM. An experiment on turbulent mixed convection to water is chosen for validation of the new model. Moreover, influence of the $Pr_{sgs}$ on the heat transfer is investigated and it is found out that this parameter significantly affects both velocity and temperature fields. Simulation results showed that the new model can be successfully applied for simulation of turbulent mixed convection. It performed better than the standard models based on constant $Pr_{sgs}$ approach.

# Zusammenfassung

Turbulente Mischkonvetion ist die Kombination aus erzwungener und natürlicher Konvektion. Das Temperaturfeld verhält sich wie ein aktiver Skalar, dies bedeutet, dass die Momenten- und Energiegleichung stark miteinander gekoppelt sind. Bei der numerischen Simulation von turbulentem Wärmetransport wird gewöhnlich das Konzept einer konstanten Prandtl Zahl $Pr_{sgs}$ angewandt. Hierbei wird von einer Ähnlichkeit zwischen Geschwindigkeit- und Temperaturfeld ausgegangen. Diese Annahme ist jedoch unzureichend für Fluide deren molekulare Prandtl Zahl sich stark von eins unterscheidet oder wenn zusätzliche Quellen auf die Strömung einwirken wie Schwerkraft oder Lorenzkraft. In diesen Fällen werden alternative Schließungsmodelle für die Energiegleichung benötigt.

In dieser Arbeit wird ein neues Feinstruktur Modell für den Transport turbulenter Wärmeströme vorgestellt. Dieses Modell basiert auf algebraischen Gleichungen. Zur Bestimmung der Modellkoefizienten wurde eine dynamische Prozedur herangezogen. Das neue Modell beinhaltet explizit den Schwerkraft-Produktionsterm, woraus sich eine Verbesserung der Qualität von Ergebnissen aus Large Eddy Simulationen (LES) erhoffen lässt, wenn Schwerkraftseinflüsse bei dem Transport der Wärme eine wichtige Rolle spielen. Zusätzlich wurde ein dynamisches Modell zur Bestimmung der turbulenten Prandtl Zahl hergeleitet. Hierbei wird die $Pr_{sgs}$ dynamisch, in Abhängigkeit von den Strömungs- und Wärmetransportbedingungen, berechnet. Implementiert wurden diesen beide Modelle in die numerische Strömungsmechanik Bibliothek OpenFOAM. Zur Validierung der neuen Modelle wurde ein Experiment mit turbulentem Wärmetransport mit Wasser nachgerechnet. Des Weiteren wurde der Einfluss von $Pr_{sgs}$ auf den Wärmetransport untersucht. Dabei konnte festgestellt werden, dass dieser Parameter sowohl das Temperatur, als auch das Geschwindigkeitsfeld signifikant beeinflusst. Die Simulationsergebnisse zeigten, dass das neue Modell mit Erfolg zur Berechnung von Strömungen mit turbulenter Mischkonvektion verwendet werden kann. Es zeigte sich eine deutliche Verbesserung im Vergleich zu herkömmlichen Modellen, die auf dem Konzept einer konstanten $Pr_{sgs}$ beruhen.

# Contents

# List of Figures

# List of Tables

# Nomenclature

### Greek

| | | |
|---|---|---|
| $\beta$ | Coefficient of thermal expansion | $[\frac{1}{K}]$ |
| $\Delta t$ | Time step | $[s]$ |
| $\Delta x$ | Cell size in $x$ direction | $[m]$ |
| $\Delta$ | Filter width | $[m]$ |
| $\delta$ | Channel half width | $[m]$ |
| $\delta_{ij}$ | Kronecker delta | $[-]$ |
| $\epsilon$ | Turbulent kinetic energy dissipation rate | $[\frac{m^2}{s^3}]$ |
| $\epsilon_\theta$ | Temperature variance dissipation rate | $[\frac{K^2}{s}]$ |
| $\kappa$ | Thermal diffusivity | $[\frac{m^2}{s}]$ |
| $\kappa_{eff}$ | Effective diffusivity | $[\frac{m^2}{s}]$ |
| $\kappa_{sgs_{ij}}$ | Tensor subgrid-scale diffusivity | $[\frac{m^2}{s}]$ |
| $\kappa_{sgs}$ | Subgrid-scale diffusivity | $[\frac{m^2}{s}]$ |
| $\lambda$ | Thermal conductivity | $[\frac{W}{mK}]$ |
| $\mu$ | Dynamic viscosity | $[\frac{kg}{ms}]$ |
| $\mu_{eff}$ | Effective dynamic viscosity | $[\frac{kg}{ms}]$ |
| $\mu_{sgs}$ | Subgrid-scale dynamic viscosity | $[\frac{kg}{ms}]$ |
| $\nu$ | Kinematic viscosity | $[\frac{m^2}{s}]$ |
| $\nu_{eff}$ | Effective kinematic viscosity | $[\frac{m^2}{s}]$ |
| $\nu_{sgs}$ | Subgrid-scale kinematic viscosity | $[\frac{m^2}{s}]$ |
| $\Omega_{ij}$ | Rotation rate tensor | $[\frac{1}{s}]$ |
| $\rho$ | Density | $[\frac{kg}{m^3}]$ |
| $\tau_w$ | Wall shear stress | $[\frac{kg}{ms^2}]$ |
| $\tau_{ij}$ | Subgrid-scale stress tensor | $[\frac{m^2}{s^2}]$ |
| $\theta$ | Temperature | $[K]$ |
| $\theta'$ | Temperature fluctuation | $[K]$ |

| | | | |
|---|---|---|---|
| $\theta'^2$ | Temperature variance | | $[K^2]$ |

## Roman

| | | | |
|---|---|---|---|
| $\mathcal{L}_{ij}$, $L_{ij}$ | Resolved stress tensor | | $[\frac{m^2}{s^2}]$ |
| $C$ | Courant number | $= \frac{u^* \Delta t}{\Delta x}$ | $[-]$ |
| $C_S$ | Smagorinsky constant | | $[-]$ |
| $Cp$ | Specific heat capacity at constant pressure | | $[\frac{J}{kg\,K}]$ |
| $D_h$ | Hydraulic diameter | | $[m]$ |
| $G$ | Filter kernel | | $[-]$ |
| $g$ | Gravitational acceleration of Earth | | $[\frac{m}{s^2}]$ |
| $Gr$ | Grashof number | $= \frac{g\beta\lvert T_s - T_\infty\rvert L^3}{\nu^2}$ | $[-]$ |
| $Gr_z^*$ | Modified Grashof number | $= \frac{g\beta q_w Z^4}{\lambda \nu^2}$ | $[-]$ |
| $h$ | Specific enthalpy | | $[\frac{J}{kg}]$ |
| $K$ | Subtest-scale turbulent kinetic energy | | $[\frac{m^2}{s^2}]$ |
| $k$ | Turbulent kinetic energy | | $[\frac{m^2}{s^2}]$ |
| $k_{sgs}$ | Subrid-scale turbulent kinetic energy | | $[\frac{m^2}{s^2}]$ |
| $N_c$ | Number of cells | | $[-]$ |
| $Nu_z$ | Local Nusselt number | $= \frac{hZ}{\lambda_f}$ | $[-]$ |
| $p$ | Pressure | | $[\frac{kg}{m\,s^2}]$ |
| $P_j$ | Test-window heat flux | | $[\frac{m\,K}{s}]$ |
| $Pr$ | Prandtl number | $= \frac{\nu}{\kappa}$ | $[-]$ |
| $Pr_{sgs}$ | Subrid-scale turbulent Prandtl number | | $[-]$ |
| $Q_i$ | Subtest-scale heat flux | | $[\frac{m\,K}{s}]$ |
| $q_i$ | Subgrid-scale heat flux | | $[\frac{m\,K}{s}]$ |
| $q_w$ | Wall heat flux | | $[\frac{W}{m^2}]$ |
| $Ra$ | Rayleigh number | $= \frac{g\beta(T_s - T_\infty)L^3}{\nu\kappa}$ | $[-]$ |
| $Re$ | Reynolds number | $= \frac{uL}{\nu}$ | $[-]$ |
| $Re_\tau$ | Friction Reynolds number | $= \frac{u_\tau L}{\nu}$ | $[-]$ |
| $Re_d$ | Reynolds number based on the cylinder diameter | $= \frac{u_{in} d}{\nu_f}$ | $[-]$ |
| $Ri$ | Richardson number | $= \frac{Gr}{Re^2}$ | $[-]$ |
| $S_{ij}$ | Strain rate tensor | | $[\frac{1}{s}]$ |
| $Sc$ | Schmidt number | | $[-]$ |

| | | | |
|---|---|---|---|
| $T$ | Temperature | | $[K]$ |
| $t$ | Time | | $[s]$ |
| $T_b$ | Bulk temperature | | $[K]$ |
| $T_f$ | Film temperature | | $[K]$ |
| $T_w$ | Wall temperature | | $[K]$ |
| $T_{ij}$ | Subtest-scale stress tensor | | $[\frac{m^2}{s^2}]$ |
| $u$ | Velocity | | $[\frac{m}{s}]$ |
| $u'$ | Velocity fluctuation | | $[\frac{m}{s}]$ |
| $u^*$ | Characteristic velocity | | $[\frac{m}{s}]$ |
| $u_b$ | Bulk velocity | | $[\frac{m}{s}]$ |
| $u_\tau$ | Friction velocity | | $[\frac{m}{s}]$ |
| $u_{in}$ | Inlet velocity | | $[\frac{m}{s}]$ |
| $y$ | Wall distance | | $[m]$ |
| $y^+$ | Dimensionless wall distance | $= \frac{u_\tau y}{\nu}$ | $[-]$ |

## Abbreviations

| | |
|---|---|
| *CFD* | Computational Fluid Dynamics |
| *LDA* | Laser Doppler Anemometry |
| *LES* | Large Eddy Simulation |
| *SGS* | Subgrid-scale |
| *THF* | Turbulent Heat Flux |

# Chapter 1

# Introduction

## 1.1 Motivation

Most of the flows appearing in everyday life and engineering applications are turbulent. In some cases turbulence is favorable, in other not. Whatever the case is, a high level of knowledge about the physics of turbulence and related phenomena is necessary.

Due to the fast development in computational technology in the recent years, numerical techniques became a very promising tool for simulation of turbulent flows. A branch of fluid mechanics which deals with numerical simulations of fluid flows is known as *Computational Fluid Dynamics*, or short CFD. Depending on the level of description of the turbulent flows, these technique are divided into the three main branches: *Reynolds- Averaged Navier Stokes (RANS)* equations, *Large Eddy Simulation (LES)* and *Direct Numerical Simulation (DNS)*.

In RANS, instantaneous flow variables are decomposed into the mean and fluctuating quantity and the governing equations are averaged in time. As a consequence, the results obtained by using this type of simulation provide only the averaged fields and fluctuations cannot be reproduced. Turbulence effects are represented by the turbulence models. RANS simulations are fastest and require lowest computational power compared to the other two groups. They are very popular among the engineers interested in qualitative results that can be obtained in a short period of time.

The most accurate approach to solve the Navier-Stokes equations is to use sufficiently fine numerical grids that are able to resolve all relevant scales of turbulence down to the Kolmogorov microscales, the smallest scales of turbulent motions on which the kinetic energy is dissipated and eventually converted into heat. This approach is known as DNS. Apart form the requirement that the smallest scales of motions have to be captured, the computational domain has to be large enough to resolve the largest turbulent motions which are limited by the physical boundaries (e.g. geometry of the apparatus). These scales are very important since the most of the energy are contained in them. A measure of the largest scale in a turbulent field is the integral length scale, $L$, and the computational domain has to be at least as large as the integral length scale. The results available from a DNS are highly detailed and provide information about turbulence which cannot be obtained otherwise (e.g. by mean of experiment). The required number of grid cells, $N_c$, is extremely high, approximately $Nc \propto Re^{9/4}$, Leonard [65], or according to recent research of Choi and Moin [12], $Nc \propto Re^{37/14}$. Here $Re$ is the ratio of inertial to viscous forces, known as Reynolds number. The number of cells strongly depends on $Re$ which limits the applicability of DNS only to the flows of small to medium Reynolds numbers.

In DNS, most of the computational resources are used to resolve the smallest scales, those that are responsible for the dissipation of energy. However, in a turbulent flow, largest scales contain most of the energy and contribute the most to the transport of fluid particles. Hence, in order to decrease computational costs and at the same time keep the fidelity of the results at sufficiently high level, it makes sense to compute only the large scales directly, while modeling all other scales. Since only the large scales are simulated, this approach is called *Large Eddy Simulation*. LES has been appearing in turbulence research since the seminal work of Smagorinsky [98]. The scales are separated by applying a filtering operation on the governing equations. The filtering operation is defined as a convolution product of a flow variable and a filter function. Filter functions which are widely applied in LES are box or top-hat filter, Gaussian and sharp spectral filter. More details about the filtering operation in LES will be given in Chapter 2.

The subgrid scales are more uniform than the large ones, which means that, in general, can be represented by models which are more simple than those used in RANS. The models that account for the influence of the subgrid (unresolved) scales on the large (resolved) scales are called *subgrid-scale* (SGS) models. It is usually said that, if the large scales are completely resolved by the numerical grid, than is the role of the subgrid models only to dissipate the energy. However, this is not quite true since it was observed in the measurements that in some cases (see e.g. [90]) a backward transport of energy from small to the large scales is also important. This process is known as backscatter. Therefore, an ability to account for a backscatter is a favorable feature of SGS models. A popular way to improve the performance of eddy diffusivity models, which are purely dissipative, is to use a *dynamic procedure* to determine model coefficients depending on the flow conditions. However, such models are usually unstable because of the model coefficient which may become and stay negative for a long period of time. Stability issues are usually treated by *ad hoc* averaging of the model coefficients over the homogeneous direction. Improved version of the dynamic models include in addition a transport equation for subgrid-scale kinetic energy which is a measure of available energy contained in the subgrid scales.

Physical systems that are found in engineering applications very often include coupling of velocity and scalar fields, e.g temperature, mass concentration, concentration of reactants, etc. If there is no feedback of the scalar field on the momentum transport, it is said that the scalar field acts as a *passive scalar*. In this case, the scalar dynamics is completely governed by the velocity field. Isothermal flows or flows with small variations of fluid temperature (so that the molecular fluid properties are not significantly affected) are examples of velocity-passive scalar coupling.

If a flow field exhibits high scalar gradients, additional volumetric forces occur and affect the momentum transport. Influence of scalar on the velocity field is too important to be neglected and has to be included in the momentum equation. This is known as the *active scalar* case. A typical example are those flows where density gradients, caused by the temperature differences, generate buoyancy force which can either generate or suppress turbulence. Depending on the intensity of the buoyancy force, heat transfer can be regarded as a forced, natural or mixed (combined) convection. The focus of this work is on the turbulent mixed convection, which appears when the approaching flow is turbulent and the buoyancy effects play an important role. These flows are characterized by strong unsteadinesses and a wide variety of physical phenomena and flow structures. They are encountered very often in the engineering application, therefore is a detailed investigation of turbulent mixed convection necessary. For that purpose, LES is an attractive approach.

Most of the common models for SGS heat flux are based on the Reynolds analogy and use a SGS turbulent Prandtl number, $Pr_{sgs}$. However, this approach may be insufficient since the influence of the buoyancy force on $Pr_{sgs}$ is not clear. Analogously to the momentum

equation, models for SGS heat flux can be improved by using a procedure to calculate $Pr_{sgs}$ dynamically and/or to include the buoyancy production term in the equation for SGS kinetic energy. However, in natural and turbulent mixed convection, velocity and temperature field are coupled also on the subgrid level, i.e. buoyancy production appears in the transport equation for the SGS heat flux. Hence, the main idea in this work is that the models for SGS heat flux based on algebraic transport equations (analogously to the RANS algebraic models for turbulent heat flux) may be a better choice when simulating buoyant turbulent flows.

## 1.2 Turbulent mixed convection

Turbulent mixed convection is a mode of heat transfer which combines both natural and forced convection. It is frequently encountered in variety of engineering applications, e.g. nuclear reactor cooling systems, turbine blades, cooling of electronic equipment, heat exchangers, solar panels, ... as well as in the nature, e.g. dynamic of oceanic and atmospheric circulations. As a consequence of density and/or temperature gradients, the buoyancy force arise, changing the structure and intensity of both mean and turbulence fields. Effects of buoyancy enter the Navier-Stokes equation through a body force. Temperature acts as an active scalar so that the momentum and energy transport are closely coupled. Because the density variations directly depend on temperature, it is possible to use only the temperature differences to represent the buoyancy force. This approach is known as the Boussinesq approximation.

In some cases, buoyancy force may increase turbulence production, while in the other it leads to the suppression of turbulence fluctuations and laminarization of the flow. A typical example of the later is the thermal stratification, which appears when density increases in the direction of gravity (see e.g. [20]). Depending on the orientation, buoyancy can either increase or decrease overall heat transfer. If the buoyancy force acts in the same direction as forced convection (buoyancy-aided flow), the advection of heat is enhanced. However, the effectiveness of heat transfer is reduced with regard to corresponding forced or natural convection. This is explained by the reduction of shear stress in the layer near the surface (see e.g. [112]). With further increase of buoyancy influence, the effectiveness of heat transfer can be improved. If the buoyancy force acts in the opposite direction than the forced convection (buoyancy opposed flow), the advection of heat is decreased, but the effectiveness of heat transfer is increased.

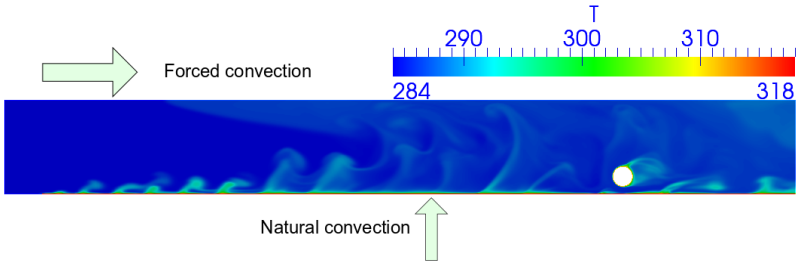


**Fig. 1.1:** LES of turbulent mixed convection heat transfer from a horizontal cylinder in a cross-flow, $Re_d = 189$, $Ri_d = 9.3$, $Gr_d = 3.5 \times 10^5$

Fig. 1.1 represents an example of turbulent mixed convection heat transfer to and from a horizontal cylinder in a cross-flow with heating from below. The original experiment was performed by Laskowski et al. [61] and here are shown LES results obtained by using the same setup as in the experiment. In the figure, the instantaneous temperature field is shown. Thermal plumes, which are consequence of buoyancy, are rising from the heated surfaces (bottom wall and cylinder) and cause transition to turbulence.

Before proceeding further, it is useful to define some of the dimensionless parameters related to the turbulent mixed convection.

- **Reynolds number**. Ratio of inertial to viscous forces

$$Re = \frac{uL}{\nu} \tag{1.1}$$

- **Prandtl number**. Ratio of kinematic viscosity to thermal diffusivity

$$Pr = \frac{\nu}{\kappa} \tag{1.2}$$

- **Grashof number**. Ratio of buoyancy to viscous forces

$$Gr = \frac{g\beta|T_s - T_b|L^3}{\nu^2} \tag{1.3}$$

- **Richardson number**. Ratio of natural to the forced convection

$$Ri = \frac{Gr}{Re^2} \tag{1.4}$$

In the equations (1.1) to (1.4) $u$ is fluid velocity, $L$ is characteristic length, $T_s$ and $T_b$ are surface and bulk temperatures respectively, $\nu$, $\kappa$ and $\beta$ are kinematic viscosity, thermal diffusivity and coefficient of thermal expansion, while $g$ represents gravitational acceleration.

## 1.3 Experimental and numerical investigations

Due to the common occurrence in engineering problems, turbulent mixed convection has received considerable attention in the last fifty years. Therefore, many researchers have investigated this problem both experimentally and numerically, and in the literature exists a large number of papers dealing with this topic. However, due to the complexity of the phenomena and difficulties in measurements, many of the experiments do not provide enough data that can be used for validation of new models. Therefore, numerical studies by means of direct numerical simulation represent an attractive approach to gain more insight in the physics of the phenomena. However, due to the high computational costs, direct numerical simulations are limited to the academical problems. Nevertheless, these simulations provide enough data which cannot be obtained experimentally, hence they are very popular and widely used for validation of models. Some of the experiments and numerical simulations available in the literature are given in Tab. 1.1.

### 1.3.1 Experimental investigations

Experimental study of mixed convection in an upward turbulent air flow through a vertical pipe heated with constant wall heat flux was performed by Carr et al. [11]. Inlet Reynolds numbers based on the pipe diameter and inlet velocity were varied between $5000$ and $14000$. The measurements were made at the streamwise location $L/D = 100$ (length/diameter). Data available from the experiment are velocity and temperature profiles and their fluctuations as well as turbulent shear stress and heat flux distribution, which are calculated from the experimental data. The measurements showed that, with increasing wall heat flux, buoyancy

**Tab. 1.1:** Experimental and numerical investigations.

| Author | Year | Method | Working fluid |
|---|---|---|---|
| Steiner [101] | 1971 | Experiment | Air |
| Carr et al. [11] | 1973 | Experiment | Air |
| Komori and Ueda [58] | 1982 | Experiment | Water |
| Jackson [43] | 1983 | Experiment | Liquid sodium |
| Osborne and Incropera [79] | 1985 | Experiment | Water |
| Fukui and Nakajima [29] | 1985 | Experiment | Water |
| Kitamura and Inagaki [55] | 1987 | Experiment | Water |
| Tanaka et al. [104] | 1987 | Experiment | Nitrogen |
| Polyakov and Shindin [87] | 1988 | Experiment | Air |
| Mori [76] | 1995 | Experiment | Air |
| Zhang and Dutta [120] | 1997 | Experiment | Water |
| Kasagi and Nishimura [50] | 1997 | DNS | Air |
| Iida and Kasagi [42] | 1997 | DNS | - |
| Knebel et al. [56] | 1998 | Experiment | Liquid sodium |
| Dutta et al. [21] | 1999 | Experiment | Water |
| You et al. [118] | 2003 | DNS | Air |
| Wang et al. [112] | 2004 | Experiment | Water |
| Laskowski et al. [62] | 2007 | Experiment | Water |
| Abu-Mulaweh [4] | 2009 | Experiment | Air |
| Poskas et al. [91] | 2011 | Experiment | Air |
| Marocco et al. [68] | 2012 | Experiment | Liquid lead bismuth |
| Maudou et al. [72] | 2013 | Experiment | Air |
| Zonta and Soldati [121] | 2014 | DNS | Water |

force increasingly affects the velocity and temperature fields. In the purely forced convection, velocity shows a flat profile in the bulk of the channel and maximum is in the channel center. However, with increasing heat flux, velocity is increased near the wall and decreased in the channel center and the maximum moved closer to the walls. For the lowest Grashof and the highest Reynolds number independently, influence of buoyancy on the velocity profile was negligible. Influence of buoyancy force is higher at lower Reynolds numbers (influence of natural convection is higher). Increasing buoyancy force suppresses the streamwise velocity fluctuations whose profile becomes flatter over the channel cross section. At fixed Reynolds number, the temperature gradient near the wall became steeper, while temperature fluctuations first decreased and then increased with increasing heat flux. The streamwise component of turbulent heat flux was monotonically increased over most of the cross section. Turbulent shear stress and wall-normal turbulent heat flux are calculated from the measured data. It is found that higher buoyancy force results in lower turbulent shear stress, while the wall-normal turbulent heat flux first decreases and then increases with buoyancy influence.

In the late 1980s, turbulent mixed convection in vertical pipes was experimentally investigated by Tanaka et al. [104] and Polyakov and Shindin [87]. In the study of Tanaka et al. [104], pressurized nitrogen gas is used as a working fluid. Two Reynolds numbers, $Re = 3000$ and $5000$ were considered, while the Grashof number was varied between $4.5 \times 10^3$ and $9.4 \times 10^6$ so that a regime map for mixed convection is provided. Experiments of Polyakov and Shindin [87] were carried out at higher Reynolds numbers, $Re = 5100$ and $Re = 9000$, while the working fluid was air. Both mean values and fluctuations of velocity and temperature fields were measured. The results showed that heat transfer coefficient along the channel wall strongly depends on buoyancy force. Starting from the isothermal case, the increase of the buoyancy force until some certain value ($Gr = 1.5 \times 10^7$ in this experiment) resulted in the monotonous

decrease of Nusselt number over the whole pipe length. Further increase of buoyancy force caused an increase of Nusselt number and at high Grashof numbers it exceeds the value for forced convection thus indicating the transition to free convection regime. Same as in the experiment of Carr et al. [11], the velocity profile showed an M-shape. The velocity and temperature fluctuations decreased when the buoyancy force was increased which is an indicator of partial flow laminarization. Turbulent shear stresses decreased and also became negative under the influence of higher buoyancy force, which is caused by the local maxima of velocity profile. Unlike the turbulent shear stress, turbulent heat flux remained always positive. A detailed review of mixed convection in vertical pipes is given in Jackson et al. [44].

Komori and Ueda [58] performed an experimental investigation of turbulent mixed convection in an open-channel (flume) flow. The idea was to investigate the influence of buoyancy on the turbulence structures and heat transport in unstably-stratified flow cooled from above. Reynolds numbers used in the experiment ranged from $Re = 10100$ to $41700$, and Richardson numbers ranged between $Ri = 0$ and $-490$. Among other conclusions, it is found that the ratio of the wall-normal to the streamwise turbulent heat flux significantly increases with increasing buoyancy force.

Experiments on turbulent convective heat transfer in horizontal channels have been performed by, e.g. Osborne and Incropera [79] and Fukui and Nakajima [29]. Air was used as a working fluid in [29], and water was used in [79]. Reynolds numbers ranged from $1400$ to $6500$ in [79] and from $6500$ to $13900$ in [29]. Grashof numbers ranged from $8.6 \times 10^5$ to $2.8 \times 10^8$ in [79], while the Richardson numbers used in [29] were between $-0.0059$ and $-0.0451$. When asymmetric heating conditions are used (only the bottom wall was heated), Nusselt numbers at the bottom wall were about $50\,\%$ larger than at the top wall, [79]. Time averaged values of velocity and temperature as well as their fluctuations are measured and given in [29] and an evident dependence on the buoyancy was observed. Streamwise velocity fluctuations were increased in the region $y^+ < 50$ with increasing buoyancy effect and no significant influence was detected in the outer region, $y^+ > 100$. A contrary behavior was observed for fluctuations in wall-normal direction. Temperature fluctuations decreased in the outer region, and remained almost constant in the region close to the wall, $y^+ < 25$.

Kitamura and Inagaki [55] conducted a series of experiments in order to investigate the buoyancy influence on the boundary layer developing at the hot vertical plate. In their experiments, water is used as a working fluid while the inlet velocity and wall heat flux were varying in order to achieve different heat transfer configurations. This experiment is used for validation and will be given in details in Chapter 4.

Turbulent mixed convection heat transfer to liquid metals was investigated by e.g. Jackson [43] and Jackson et al. [45] who investigated turbulent mixed convection to liquid sodium in an uniformly heated vertical pipe, Knebel et al. [56], who measured mean velocity, mean temperature and temperature fluctuations in a vertical axisymmetric turbulent buoyant sodium jets, or more recently by Marocco et al. [68], where experimental investigations of turbulent lead bismuth flow within a vertical annulus were performed. In [68] Reynolds number were between $1.45 \times 10^4$ and $2.37 \times 10^5$, while the wall heat flux was varied between $135\,kW/m^2$ and $905\,kW/m^2$ so that both forced and mixed convection regime were covered.

Wang et al. [112] investigated turbulent mixed convection heat transfer to air in a vertical channel heated from one side. Both buoyancy- aided and buoyancy-opposed flows were considered. Moreover, radiation played a significant role in this configuration since the radiative heat transfer between section walls was up to $20\,\%$. The heat emitted from the heated wall was absorbed by the unheated wall and removed from it by the air flowing through the channel. It is found that the process of heat removal from the unheated wall was also influenced by the buoyancy.

More recently Maudou et al. [72] studied the influence of eccentricity on the heat transfer in the mixed convection regime. The experimental configuration was annular channel with both internal surfaces uniformly heated. Three different inlet Reynolds numbers were considered: $Re = 1500, 2800$ and $5700$, so that laminar, transitional and turbulent flows were were included. The results showed that small eccentricities almost have no effects on the heat transfer, but at high eccentricities ($0.8 \leq e \leq 0.9$) the average heat transfer rate was up to $60\,\%$ lower than in the concentric annular channel.

### 1.3.2 Numerical investigations

Direct numerical simulations of turbulent mixed convection available in the literature are limited to the simple geometries like vertical or horizontal pipes or channels. The channel configurations are much more popular since it is easier to impose temperature boundary conditions at the wall: the walls are usually kept at constant but different temperatures, where one wall is heated and the other one is cooled. Furthermore, channels are very convenient for study of some external effects, e.g. magnetic field or radiation, on the flow and temperature fields. Another simplification, which however cannot be justified for higher temperature differences, is the assumption of uniform fluid properties which is used in almost every DNS found in the literature.

#### Turbulent channel flow

Kasagi and Nishimura [50] performed a direct numerical simulation of mixed convection in an infinite vertical plane channel, where the channel walls were kept at different temperatures - one heated and one cooled wall. In this configuration it is possible to investigate buoyancy-aiding and buoyancy opposing flows at the same time: aiding flow arises at the heated wall, while opposing flow arises on the cooled wall. The friction Reynolds number based on the channel half width and friction velocity calculated from the wall shear-stress averaged on both walls was $Re_\tau = 150$. The Grashof number based on the channel width and the wall temperature difference was between $0$ and $1.6 \times 10^6$. The Prandtl number was set to $0.71$, which corresponds to air. The Navier-Stokes equations with the Boussinesq approximation are solved together with continuity and energy equations on the $5\pi\delta \times 2\pi\delta \times 2\delta$ computational domain ($\delta$ represents the channel half width). Some of the main conclusions from the results are:

- The friction coefficient was increased in the aiding flow and decreased in the opposing flow with the increase of buoyancy
- The nusselt number was decreased in the aiding and increased in the opposing flow with the increase of buoyancy
- The velocity profile becomes more asymmetric with the increase of buoyancy
- The RMS values of velocity fluctuations are decreased in the aiding and increased in the opposing flow
- The mean temperature profile becomes asymmetric with the increase of buoyancy
- The mean temperature gradient is becomes larger in the aiding and smaller in the opposing flow
- The RMS of temperature fluctuations in the near-wall regionare decreased in the aiding and increased in the opposing flow

- The wall-normal component of the turbulent heat flux is decreased in the aiding and increased in the opposing flow with the increase of buoyancy
- The buoyancy force affects turbulent statistics and coherent structures in much the same way as the wall injection/suction or magnetic force.

The database provided in [50] is extensively used for validation of both RANS and LES models.

Iida and Kasagi [42] conducted a DNS of a fully developed horizontal turbulent channel flow under conditions of unstable thermal stratification. Bottom and top channel walls were kept at constant but different temperatures. The incompressible set of equations with Boussinesq approximation and constant fluid properties (except density which is treated as a function of temperature) is solved on the $5\pi\delta \times 2\pi\delta \times 2\delta$ computational domain (for some specific cases, computational domain was enlarged or decreased). Friction Reynolds number was set to $Re_\tau = 150$ which gave the bulk Reynolds number of $Re = 4580$. The Grashof number was varied between $Gr = 0$ and $4.8\times10^6$. Furthermore, the effect of the molecular Prandtl number on the heat transfer was investigated by increasing the Prandtl number from $Pr = 0.01$ to $2$ for constant Grashof number of $Gr = 1.3\times10^6$. Among other conclusions, it is found out that the Prandtl number significantly affects the flow field. For the lowest Prandtl number, $Pr = 0.01$, heat is transported mainly by the molecular diffusion and the buoyancy effects become less important.

DNS of turbulent dispersion of a non-buoyant scalar, mixed convection in a vertical channel and dispersion of a buoyant plume in a horizontal channel are performed by Fabregat et al. [23]. Friction Reynolds number and Grashof number for the cases of mixed convection and dispersion of a buoyant scalar was $Re_\tau = 150$ and $180$ and $Gr = 9.6^5$ and $10^7$ respectively. Again, incompressible set of equations with constant properties (except density) is solved. Working fluid was air. The main contribution of this work is the database for dispersion of a buoyant plume which can be interesting for validation of SGS models. Further studies on this topic were conducted by Karna and Papavassiliou [49], who investigated dispersion of a buoyant scalar at higher friction Reynolds number, $Re_\tau = 300$, which corresponds to $Re = 5320$ based on the channel half width. Five different Prandtl numbers were used: $Pr = 0.1$, $0.7$, $6$, $20$ and $50$.

The radiation effect on turbulent mixed convection in a horizontal channel is investigated by Sakurai et al. [95]. In their DNS, incompressible continuity, Navier-Stokes and energy equations are solved. Friction Reynolds, Prandtl and Grashof numbers were set to $150$, $0.71$ and $1.3\times10^6$ respectively. The Boussinesq approximation is used to represent buoyancy force and radiative source term is expressed as divergence of the radiative heat flux.

In most of the DNS of mixed convection, the incompressible set of equations with Boussinesq approximation is solved. The effects of non-constant fluid properties were recently investigated by Zonta and Soldati [121]. They have conducted DNS of a turbulent flow of water through a horizontal channel at three friction Reynolds numbers: $Re_\tau = 110$, $150$ and $180$ and Grashof number of $Gr = 1.12\times10^7$. Molecular Prandtl number was set to $Pr = 3$. The aim of the study was to assess the influence of fluid properties. For that purpose, three different cases were investigated, one with constant fluid properties, one with temperature dependent dynamic viscosity, $\mu$, and one with temperature dependent coefficient of thermal expansion, $\beta$. The authors found out that only $\beta$ is important, whereas the effect of $\mu$ can be negligible. However, a case where both dynamic viscosity and coefficient of thermal expansion are temperature dependent is not considered.

**Turbulent pipe flow**

Turbulent mixed convection in a vertical pipe heated with uniform wall heat flux was investigated by You et al. [118] by means of direct numerical simulation. Both upward (aiding) and downward (opposing) flows were simulated. A constant mass flow rate is imposed, and Reynolds number based on the pipe radius and bulk velocity was fixed at $Re = 2650$ which corresponds to the friction Reynolds number of $Re_\tau = 180$. Air is used as a working fluid, $Pr = 0.71$. The incompressible set of equations with the Boussinesq approximation is solved and fluid properties are treated as constant. Four different values of wall heat flux were applied which gave values for $Gr_q/Re^2 = 0$ (forced convection), $0.063$, $0.087$ and $0.241$. Some of the observations from the simulation results are:

- In upward heated (aiding) flow the velocity profile near the wall first decreases and then increases with increasing wall heat flux. M-shapes are observed at high wall heat fluxes
- In downward heated (opposing) flow the velocity profile increases monotonically in the bulk region
- RMS values of velocity fluctuations in upward flow first decrease and then increase with increasing wall heat flux, while in downward flow they monotonically increase
- The non-dimensional temperature profile first decreases and then increases with the increasing heat flux in upward flow, while it decreases monotonically in downward flow. RMS values of temperature fluctuations show similar behavior in upward flow, while a monotonous increase is observed in downward flow
- The magnitude of streamwise and wall normal turbulent heat fluxes first decreases and then increases in upward flow, while it monotonically increases in downward heated flow
- The heat transfer coefficient first decreases and then increases in upward heated flow and monotonically increases with increasing heat flux in downward flow.

Many researchers have used this database to validate their subgrid-scale models for heat flux in the mixed convection conditions (see e.g. [26]).

## 1.4 Subgrid-scale heat flux modeling - State of the art

In this section, we shell consider some of the models for subgrid-scale heat flux available in the literature. Generally, the subgrid-scale modeling is a fertile scientific field and in the literature exists a large number of models for both subgrid-scale momentum and temperature (scalar) fluxes. Sometimes it is very hard to make a clear division between different groups of models, since some of them represent a combination of different modeling approaches (mixed models). In this work, modeling approaches for subgrid-scale heat flux are simply divide into the three main categories:

- Scalar SGS diffusivity
- Tensor (anisotropic) SGS diffusivity
- Mixed models.

The most popular models for SGS heat flux are those which assume that turbulence affects the main field in a similar way as molecular diffusion does. In analogy to molecular diffusion, the effects of turbulence are represented by a scalar quantity, known as turbulent (subgrid-scale) diffusivity, $\kappa_{sgs}$. Likewise, the effects of turbulence on the momentum transfer can be represented by turbulent (subgrid-scale) viscosity, $\nu_{sgs}$. The ratio of $\nu_{sgs}$ to $\kappa_{sgs}$ is defined as subgrid-scale (turbulent) Prandtl number, $Pr_{sgs}$. Provided that $\nu_{sgs}$ is known, one only has to give a value for $Pr_{sgs}$ in order to evaluate $\kappa_{sgs}$. In most cases, $Pr_{sgs}$ is taken to be a constant value close to one. However, this approach may result in unsatisfactory results, in particular for flows where temperature field acts as an active scalar (e.g. natural or mixed convection). Therefore, many researchers have tried to improve the models based on the scalar SGS diffusivity: Eidson [22] has included buoyancy effects in his formulation of $\nu_{sgs}$; Moin et al. [75] and Lilly [66] derived models for $Pr_{sgs}$ which is calculated dynamically in time depending on the velocity and temperature fields. Other works where the models based on the scalar SGS diffusivity are improved for different heat transfer conditions are, e.g. Wong and Lilly [115], Peng and Davidson [84], You and Moin [117], or more recently, Otic [81], who derived a model that provides an estimate for $Pr_{sgs}$, which is calculated depending on the local fluid properties.

**Tab. 1.2:** Models for SGS heat flux

| | Author | Year |
|---|---|---|
| Scalar thermal diffusivity | Eidson [22] | 1985 |
| | Moin et al. [75] | 1991 |
| | Lilly [66] | 1992 |
| | Wong and Lilly [115] | 1994 |
| | Peng and Davidson [84] | 2001 |
| | You and Moin [117] | 2007 |
| | Otic [81] | 2010 |
| Anisotropic thermal diffusivity | Pullin [92] | 2000 |
| | Peng and Davidson [85] | 2002 |
| | Wang et al. [109] | 2007 |
| | Wang et al. [110] | 2007 |
| | Wang et al. [111] | 2008 |
| | Rasam et al. [93] | 2013 |
| Mixed models | Salvetti and Banerjee [96] | 1995 |
| | Porte-Agel et al. [89] | 2001 |
| | Porte-Agel et al. [90] | 2001 |

Models for subgrid-scale heat flux which are based on tensor (anisotropic) SGS diffusivity are derived to be applied for complex flows where anisotropy of turbulent (SGS) stresses and heat fluxes cannot be neglected. Several tensor SGS diffusivity models were developed in the first decade of this century, mostly for forced convection and rotational flows: Pullin [92] proposed a model for the flux of passive scalar; Peng and Davidson [85] developed a nonlinear SGS heat flux model which was tested for the buoyant flow in a vertical channel; Wang et al. [109, 110, 111] proposed a series of models where the SGS het flux includes strain-rate tensor, rotation rate tensor and gradient of large-scale temperature field; Rasam et al. [93] proposed a model for SGS heat flux which is capable to account for system rotation.

Mixed models represent a combination of different modeling approaches, for example, gradient diffusion and scale similarity model. In scale-similarity models, SGS heat flux is assumed to be proportional to the resolved (which can be directly calculated) heat flux. Same as for tensor SGS diffusivity models, SGS heat flux is not necessary aligned with the resolved temperature gradient. An example of such an scale-similarity model is the model of Salvetti and Banerjee [96], who added a term proportional to the resolved heat flux vector to the

scalar SGS diffusivity model. A mixed model which includes the gradient diffusion model and the nonlinear (SGS diffusivity) model is investigated in [89, 90]

Some of the models for SGS heat flux available in the literature are given in Tab. 1.2. A more detailed description for some of them is given in Sec. 2.5. For further details about the different modeling approaches in LES, interested reader is referred to Sagaut [94].

## 1.5 Objectives and approach

Objective of this work is to propose a novel approach to calculate subgrid-scale heat flux for turbulent mixed convection.

The new models is developed by extending the idea of algebraic heat flux models which is widely used in RANS to model turbulent heat flux. Buoyancy production term from the transport equation for SGS heat flux is explicitly included into the modeled equation for SGS heat flux. Instead of solving an additional equation for SGS temperature variance, it is approximated by a term proportional to its production rate. In addition, the dynamic procedure is applied to evaluate model coefficients which are calculated dynamically by solving a system of two linear equations.

It is expected from the new model to improve prediction for the turbulent flows where buoyancy effects play an important role, such as turbulent mixed convection. At the same time, the new model can be applied without any kind of *a priori* adjustment of model coefficients. For purely forced convection, the model will perform like the standard dynamic $Pr_{sgs}$ model.

This document is organized as follows. In Chapter 2, governing equations and necessary background for turbulent flows, large eddy simulation and finite volume discretization are given. Derivation of the new model for subgrid-scale heat flux is shown in Chapter 3, and validation is given in Chapter 4. Finally, conclusions are given in Chapter 5.

# Chapter 2

# Theoretical background

In this chapter, fundamentals of turbulence, large eddy simulation and numerical discretization are given. Basic introduction to turbulent flows is provided in the first section. Concept of LES and governing equations are described in 2.2 and 2.3. Some of the subgri-scale models for momentum and energy equations are given in 2.4 and 2.5. Finite volume method and numerical discretization are briefly presented in 2.6.

## 2.1 Turbulent flows

At the beginning of this chapter it is useful to mention some of the important properties of turbulent flows. According to Hinze [40], *"Turbulent fluid motion is an irregular condition of flow in which the various quantities show a random variation with time and space coordinates, so that statistically distinct average values can be discerned"*. Turbulent flows are governed by the Navier-Stokes equations whose solutions are random. The Navier-Stokes equations strongly depend on the initial and boundary conditions and even the smallest perturbation can produce quite different solutions.

A vast number of flows occurring in the nature and engineering applications are turbulent. In some applications turbulence is desirable but in other, not. Whatever the case is, turbulent flows have to be carefully investigated. It is hard to find an universal definition of turbulence, however, some of the main characteristics can be distinguished. Detailed introduction to turbulence is given in e.g. [16, 40, 88, 105].

- Turbulent flows are three-dimensional and rotational.
- They are irregular (random) in both space and time, and exhibit large level of fluctuations.
- They are dissipative in nature. Kinetic energy of flow is transformed into heat due to the viscosity effects. Without an external source, turbulence will decay.
- Turbulence increases the transport rate of fluid parcels. The process of mixing of fluid parcels under the influence of turbulence is known as turbulent diffusion.
- The smallest scales of turbulent motions are far larger the mean free path of molecules.
- Turbulence is characteristic of a flow and not of a fluid.

Turbulence occurs when inertial forces become too high compared to viscous forces (at high Reynolds numbers) as a consequence of flow instabilities. Reynolds number, $Re$, is a dimensionless quantity which relates inertial to viscous forces

$$Re = \frac{uD_H}{\nu} = \frac{\rho u D_H}{\mu}, \tag{2.1}$$

wherein $\rho$, $\nu$ and $\mu$ are density, kinematic and dynamic viscosity respectively, $u$ is velocity and $D_H$ is hydraulic diameter. Reynolds number is, among other things, used to distinguish different flow regimes. For a pipe flow, transition to turbulence occurs at $Re > 2300$ and the transitional region is usually between $2300 < Re < 4000$.

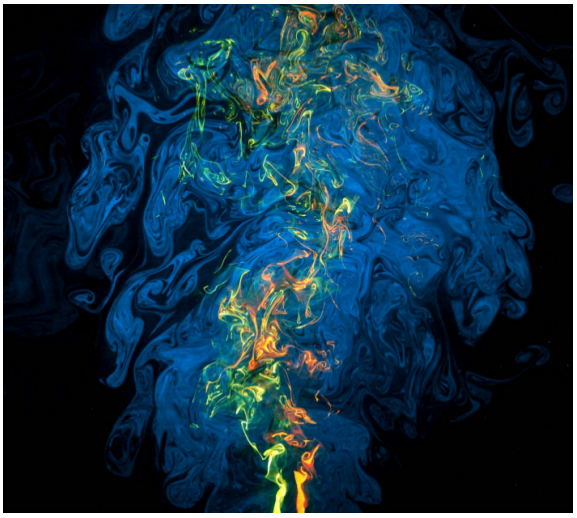

**Fig. 2.1:** Turbulent mixing of Fluorescein (green) and Rhodamine (red) in a water turbulent jet (blue), Kree et al. [59].

### 2.1.1 The statistical description of turbulence

Unlike laminar flow, turbulence is a random process which means that the values of flow variables are unpredictable in time. However, a scope of values which certain variable could have can be determined by a theory and for that purpose a statistical description of turbulence is required. Therefore it is useful do define some statistical tools which are used throughout this work (for more details see e.g. [20, 88, 105]).

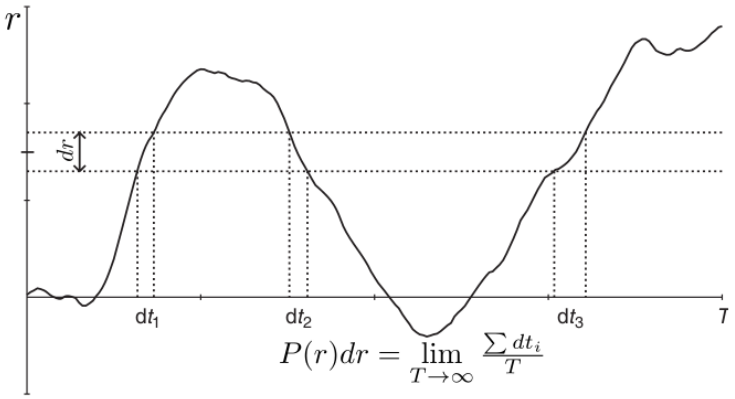


**Fig. 2.2:** Definition of PDF (adjusted from Durbin and Reif [20]).

- **Probability Density Function (PDF)**. PDF, $P(r)$, of a random function $x(t)$ is defined as a fraction of time that the function $x(t)$ spends in the range between $r - \frac{1}{2}dr$ and $r + \frac{1}{2}dr$, where $r$ represents a dummy variable that ranges between the possible values of $x$.

$$P(r)dr = \lim_{T\to\infty} \frac{1}{T} \sum dt', \tag{2.2}$$

in which $T$ represents the time coordinate. PDF is always positive and fulfills the normalization condition:

$$\int_{-\infty}^{\infty} P(r)dr = 1. \tag{2.3}$$

Fig. 2.2 shows a schematic definition of PDF. For isotropic turbulence (the one without a preferred direction) probability of amplitudes of fluctuations around a mean value shows the Gaussian distribution.

- **Mean value**. Most of the turbulence data available from the experiments are in the form of mean values. A mean value of a function $x(t)$ can be calculated as follows ([20]).

  - **Continuous case**.

$$\bar{x} = \int rP(r)dr. \tag{2.4}$$

  - **Discrete case**. In practice, it is more likely to use the discrete data sets so that the mean value of a discrete random function $x$, which takes the values $x_i = \{a_1, a_2, ..., a_J\}$, can be calculated as

$$\bar{x} = \frac{1}{N}\sum_{i=1}^{N} x_i = \sum_{j=1}^{J} \frac{N_j}{N} a_j = \sum_{j=1}^{J} p_j a_j, \tag{2.5}$$

    where $N_j$ is the number of times the value $a_j$ appears in the sample $x_i$ and $p_j$ is the probability of the value $a_j$ occurring.

For statistically stationary (independent of time) random processes, ensemble averaging and time averaging are equivalent. Properties of such an averaging operation are:

$$\overline{x+y} = \bar{x} + \bar{y}, \tag{2.6}$$

$$\overline{ax} = a\bar{x}, \tag{2.7}$$

$$\bar{\bar{x}} = \bar{x}, \tag{2.8}$$

$$\overline{x - \bar{x}} = 0, \tag{2.9}$$

where $a$ is a constant value.

- **Variance**. It is also known as second moment. Fluctuation of $x$ around mean value $\bar{x}$ is defined as

$$x' \equiv x - \bar{x}. \tag{2.10}$$

Now, variance is defined as a mean of square fluctuation

$$var(x) \equiv \overline{x'^2} = \int (r - \bar{x})^2 P(r)dr. \tag{2.11}$$

A very common in practice is a square-root of the variance, which is known as *standard deviation* or *rms* (root mean square) of $x$:

$$rms(x) \equiv \sqrt{var(x)}. \tag{2.12}$$

Higher moments, second and third, are also common in turbulence research. These are used to define *skewness* and *flatness* factor.

### 2.1.2 Numerical studies of turbulent flows

Because of the closure problem, numerical methods seem to be only possibility to solve Navier-Stokes equations. Depending on the Level of description, numerical studies of turbulent flows can be divided into the three main branches which will be briefly described here.

#### Reynolds-average Navier-Stokes equations (RANS)

A turbulent flow field obtained by solving the RANS equations contains lowest level of details compared to the other two approaches. Governing equations are averaged in time so that only the time-averaged fields come as results. This method is very popular among engineers which are interested mainly in quantitative properties of the turbulent flow and are limited by the computational time. Turbulence is completely modeled so that the models implemented in RANS suffer from high mathematical complexity.

The effects of turbulence are contained in Reynolds stress tensor, which has to be modeled in order to close the momentum equation, and in turbulent heat flux, which is needed to close the energy equation. Transport equations can be used for Reynolds stress tensor and turbulent heat flux, however, every additional transport equation includes new unknown terms that, again, need additional equations, and so on. This is known as closure problem. Therefore, approximations (turbulence models) are used to describe the unknown terms. Generally, turbulence models used in RANS can be divided into four main categories ([114]):

1. *Algebraic (Zero-Equation) Models*. These are the most simple turbulence models. No addition equation is needed.
2. *One-Equation Models*. They are based on the equation for turbulent kinetic energy. Length scale is the unspecified part, and it is assumed that the length scale is proportional to the mixing length.
3. *Two-Equation Models*. Beside the equation for turbulent kinetic energy, and additional equation to determine the turbulent length scale is solved. A common approach is to use the equation for dissipation rate of turbulent kinematic energy; this is the well-known $k-\epsilon$ model.
4. *Second-Order Closure Models*. Instead of applying the Boussinesqu approximation, a transport equation is used to compute the Reynolds stress tensor. The modes are more robust than the other RANS models but require higher computational costs.

Even though the RANS simulations provide only an averaged picture of turbulence, for many engineering problems, RANS method is still the only numerical tool that can be applied.

#### Large Eddy Simulation (LES)

Level of description of LES lays between RANS and DNS. Only the most energetic structures of the flow are resolved directly while the all other scales (usually called subrid-scales) are represented by models. Computational cost is higher than for RANS, but resolved fields contain more details. Mathematical models that represent effects of the subrid-scales are generally simpler than the models used in RANS. LES method will be presented in details in 2.2.

**Direct Numerical Simulation (DNS)**

Numerical grid spacing used in DNS is fine enough so that all relevant scales down to the Kolmogorov scale are directly resolved and there is no need for additional turbulence models. This means that (depending on the Reynolds number) a very large number of grid cells is required, which limits the applicability of DNS only to the flows at relatively low Reynolds numbers. Most of the computational power is used to capture the smallest scales which are responsible for dissipation of turbulence energy. With increasing Reynolds number, the scales that are expected to occur in the flow field becomes smaller. Moreover, numerical algorithm should produce low numerical dissipation, because otherwise small eddies can be smeared. On the other hand, numerical schemes that are not dissipative enough are very often unstable.

Beside the spatial resolution, time resolution has to be fine enough to capture life-times of all eddies, from smallest to largest, which means that the time step should be small enough and that the simulation time should be long enough. In addition, time step affects accuracy of the solution so that it is usually required that a path that fluid parcel travels in a single time step should be smaller than grid spacing. This criteria is defined by the *Courant number*

$$C = \frac{u^* \Delta t}{\Delta x}, \tag{2.13}$$

where $u^*$ is velocity in a computational cell, $\Delta t$ is a time step and $\Delta x$ is length of a cell in the flow direction. Suggestions are that the Courant number should be around $1/20$, [88].

Data obtained from DNS are very detailed and can replace experimental measurements, especially for the cases where measurements are complicated or even not feasible. DNS is very often used to generate data bases for validation of RANS and LES models.

## 2.2 Concept of Large Eddy Simulation

Turbulent flows are characterized by a wide range of length and time scales. The energy flows in a cascade process from large to the small scales, eventually being dissipated at the smallest scales, known as Kolmogorov microscales. In order to get highest quality of the results the discretization has to be fine enough so that all scales can be solved - direct numerical simulation. This means that a large number of cells is needed, $Nc \propto Re^{9/4}$, Leonard [65]. However, recent researches, Choi and Moin [12], showed that this number is even larger, $Nc \propto Re^{37/14}$. Moreover, time step should be smaller than the smallest time scale. Consequently, direct numerical simulations require high computational resources which, except for a limited number of academic cases, exceeds the present super computers capacities.

Since the large scales are more energetic and transport of the momentum and other conserved fluid properties are mostly carried out by these scales, it is reasonable to solve only the large scales directly by the numerical grid, while modeling all other scales. This is the basic idea of large eddy simulation. Small, or, unresolved scales are more uniform and it is possible to parametrize them by using the models which are simpler than the models used in RANS. By doing so, it is possible to significantly reduce the computational costs and at the same time to provide enough informations about the problem of interest so that the flow physics is resembled in a more realistic way. Regarding the computational requirements, LES is between RANS and DNS.

Fig. 2.3 shows a schematic view of scale separation in physical (left) and Fourier space (right). Large and small scales are naturally separated by the numerical grid: grid is fine enough to capture large scales, while all other scales smaller than cell size, $\bar{\Delta}$, are "invisible".

However, those subgrid scales affects the large (resolved) scales and this interaction has to be represented by SGS model. In the Fourier space, it can be seen that only the low-frequency modes, which are associated with the large scale motions, are computed directly.

It should be mentioned that the above discussion is referred to the *explicit* Large Eddy Simulation approach. In this approach, effect of the unresolved scales is represented through the subgrid-scale model which is included in the governing equations. In addition there is also the *implicit* Large Eddy Simulation approach, where the effects of the subgrid scales are included by numerical methods. More about this topic is given in Sagaut [94].

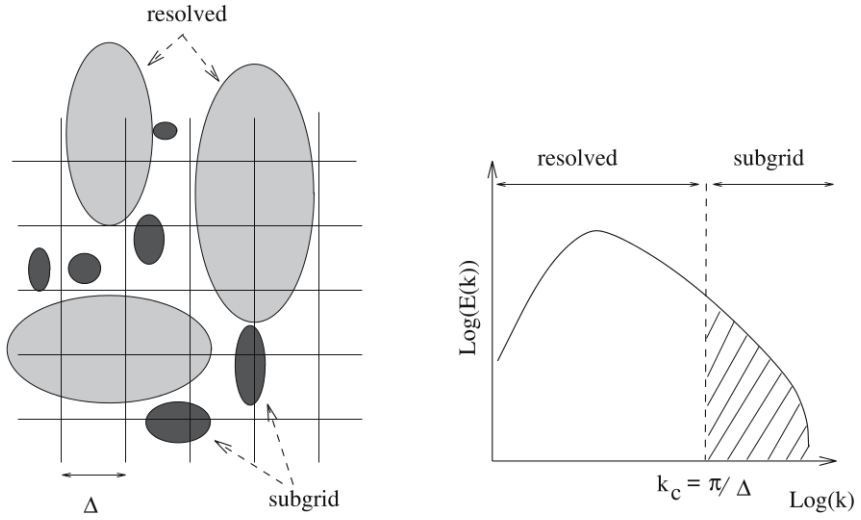


**(a)**

**Fig. 2.3:** Different scales in a turbulent flow (left) and scale separation in LES shown in Fourier space (right), Sagaut [94].

### 2.2.1 Filtering

#### Definition of filtering

In Large Eddy Simulation, scales are separated by applying a low-pass filtering operation which is defined as a convolution product. Given a field $\phi(x)$ which is a space variable (for the sake of brevity the time variable is not considered) and contains all scales of motions, then the filtered field $\bar{\phi}(x)$ is defined by the relation (see e.g. [25, 28, 65, 88, 94]):

$$\bar{\phi}(x) = \int_{\Omega} G(x-\xi)\,\phi(\xi)d\xi, \tag{2.14}$$

where $x$ and $\xi$ represent position vectors, $G(x-\xi)$ is the convolution kernel whose role is to damp fluctuations shorter than some characteristic filter width $\Delta$ and the integration is over the whole domain. The filter width has to be smaller than the size of the smallest energy-containing eddy so that the energy-containing scales can be directly resolved. Relation (2.14) is very often symbolically given by $\bar{\phi} = G \star \phi$. The convolution kernel (or filter function) $G$ has to fulfill the following criteria:

$$\int_{\Omega} G(x-\xi)d\xi = 1. \tag{2.15}$$

Then, the field $\phi(x)$ can be written in the terms of resolved and subgrid scales as:

$$\phi(x) = \bar{\phi}(x) + \phi'(x), \tag{2.16}$$

where $\phi'(x)$ represents unresolved or subgrid scales. It is important to mention that the resolved field $\bar{\phi}(x)$ is a random field.

### Filter properties

Filters used in LES must possess the following fundamental properties (see [94]):

1. Conservation of constants. Eq. (2.15) yields:
$$\bar{c} = c. \tag{2.17}$$
2. Linearity
$$\overline{\phi + \psi} = \bar{\phi} + \bar{\psi}. \tag{2.18}$$
3. Commutation with derivation
$$\frac{\overline{\partial \phi}}{\partial s} = \frac{\partial \bar{\phi}}{\partial s}, \qquad s = x, t, \tag{2.19}$$
where $t$ is a time variable.

It has to be mentioned that commutation with derivation property always holds if the derivation is with respect to time. However, if the derivation is with respect to spatial coordinate $x$, then the convolution and derivation do not commute in general (see e.g. [35, 88]). This can be shown by finding the partial derivative of (2.14) with respect to $x$. By integrating by parts, the following relation is obtained:

$$\frac{\partial \bar{\phi}}{\partial x} = \frac{\overline{\partial \phi}}{\partial x} + \int_{\Omega} \phi(\xi) G(x - \xi) d\xi, \tag{2.20}$$

which shows that filtering and derivation with respect to spatial variable do not commute in general. This means that in LES every spatial derivation generates additional unknown terms. Ghosal and Moin [35] found that the commutation error is of the order $\mathcal{O}(\Delta^2)$.

However, for homogeneous filters will second term on the RHS of Eq. (2.20) vanish so that the relation (2.19) holds also when $s$ is a spatial variable. In this work we assume that the filter is homogeneous (filter width is constant) $\Delta = const$. The commutation errors between filtering and spatial derivation are ignored. It should be noted that this idealized approach is widely used among the LES researchers, see e.g. [94].

Other important characteristics of the filter that have to be mentioned are:

- In general, the filter is not a Reynolds operator
$$\bar{\bar{\phi}} \neq \bar{\phi}. \tag{2.21}$$
- The filter is not idempotent
$$\overline{\phi\bar{\psi}} \neq \bar{\phi}\bar{\psi}. \tag{2.22}$$
- Filtered subgrid quantity does not vanish in general
$$\bar{\phi'} \neq 0. \tag{2.23}$$

### Standard filters in LES

The most common filters used in LES are (see [94]):

- Box or top-hat filter. Represents the average of a field over a box bounded by the filter width $\Delta$

$$G(x_i - \xi_i) := \begin{cases} \frac{1}{\Delta} & \text{if } |x_i - \xi_i| \leq \frac{\Delta}{2} \\ 0 & \text{otherwise} \end{cases}, \tag{2.24}$$

$$\hat{G}(k) = \frac{\sin(k\Delta/2)}{k\Delta/2}, \tag{2.25}$$

  where $\hat{G}(k)$ represents transfer function. For uniform grids, filter width can be easily chosen to be equal to the grid-spacing. It is smooth in spectral space.

- Gaussian filter. The Gaussian distribution is used for filter function

$$G(x_i - \xi_i) = \left(\frac{\gamma}{\pi\Delta^2}\right)^{1/2} \exp\left(\frac{-\gamma|x_i - \xi_i|^2}{\Delta^2}\right), \tag{2.26}$$

$$\hat{G}(k) = \exp\left(\frac{-\Delta^2 k^2}{4\gamma}\right), \tag{2.27}$$

  where $\gamma$ is a constant. It is smooth in both physical and spectral spaces.

- Sharp spectral filter. This filter is sharp in spectral space which means that it eliminates all wave-numbers above some chosen cutoff wave-number.

$$G(x_i - \xi_i) = \frac{\sin(k_c(x_i - \xi_i))}{k_c(x - \xi)}, \qquad \text{with} \quad k_c = \frac{\pi}{\Delta}, \tag{2.28}$$

$$\hat{G}(k) := \begin{cases} 1 & \text{if } |k| \leq k_c \\ 0 & \text{otherwise} \end{cases}. \tag{2.29}$$

Fig. 2.4 shows these three filters and their transfer functions. Throughout this work, the box filter will be used.

### Numerical representation of filters

For an arbitrary polyhedral computational domain element with $n$ faces, filtered field $\bar{\phi}$ can be evaluated as follows

$$\bar{\phi} = \sum_{i=1}^{n} a_i \phi_i, \tag{2.30}$$

in which $a_i$ are filter coefficients and $\phi_i$ is the value of unfiltered field $\phi$ at the $i$th cell face. Conservation of constant values, Eq. (2.17), is assured if coefficients $a_i$ obey the condition

$$\sum_{i=1}^{n} a_i = 1. \tag{2.31}$$

For a homogeneous filter, $\Delta = const$, coefficients $a_i$ are equal, $a_1 = a_2 = ... = a_n = const$. In practice, [1], ratio of face-surface area to cell-surface are can be used for coefficients $a_i$, so that the filtered field can be obtained from the following relation:

$$\bar{\phi} = \frac{\sum_{i=1}^{n} S_i \phi_i}{\sum_{i=1}^{n} S_i}, \tag{2.32}$$

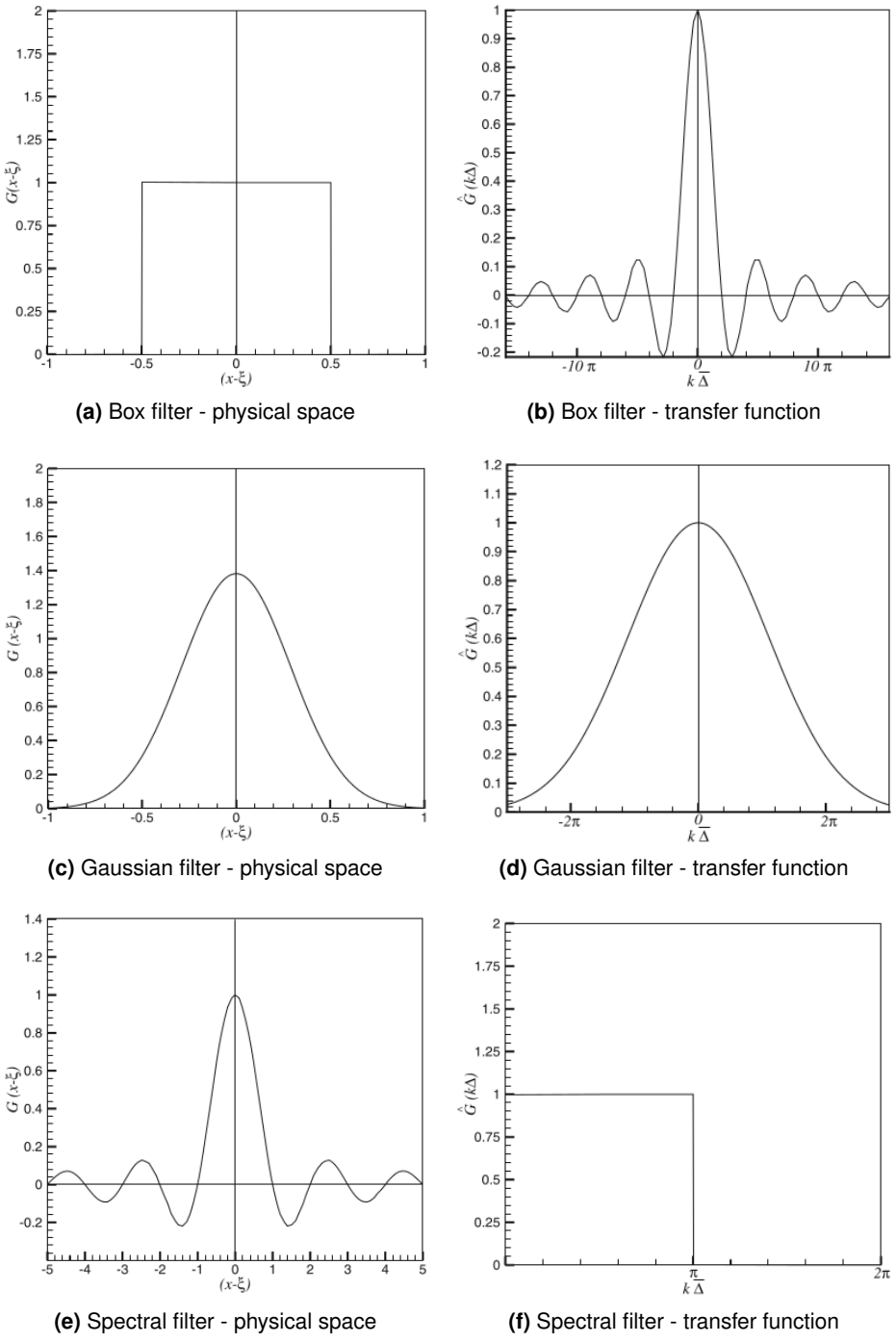


**(a)** Box filter - physical space

**(b)** Box filter - transfer function

**(c)** Gaussian filter - physical space

**(d)** Gaussian filter - transfer function

**(e)** Spectral filter - physical space

**(f)** Spectral filter - transfer function

**Fig. 2.4:** Standard filters in LES. Adapted from Sagaut [94].

where $S_i$ represent magnitude of face $i$ and $\phi_i$ is value of the unfiltered field at the face $i$. Eq. (2.32) automatically assures conservation of constants.

### An example of filtering

In order to complete the definition of the filtering operation, an example of filtering in one dimension will be shown here.

A box filter given by Eq. (2.24) is applied to filter the function $\phi(x) = \sin\left(\frac{2\pi x}{l}\right) +$

$0.1 \sin\left(\frac{30\pi x}{l}\right)$. Fig. 2.5 shows filtered function $\bar{\phi}(x)$ obtained by applying different filter sizes.

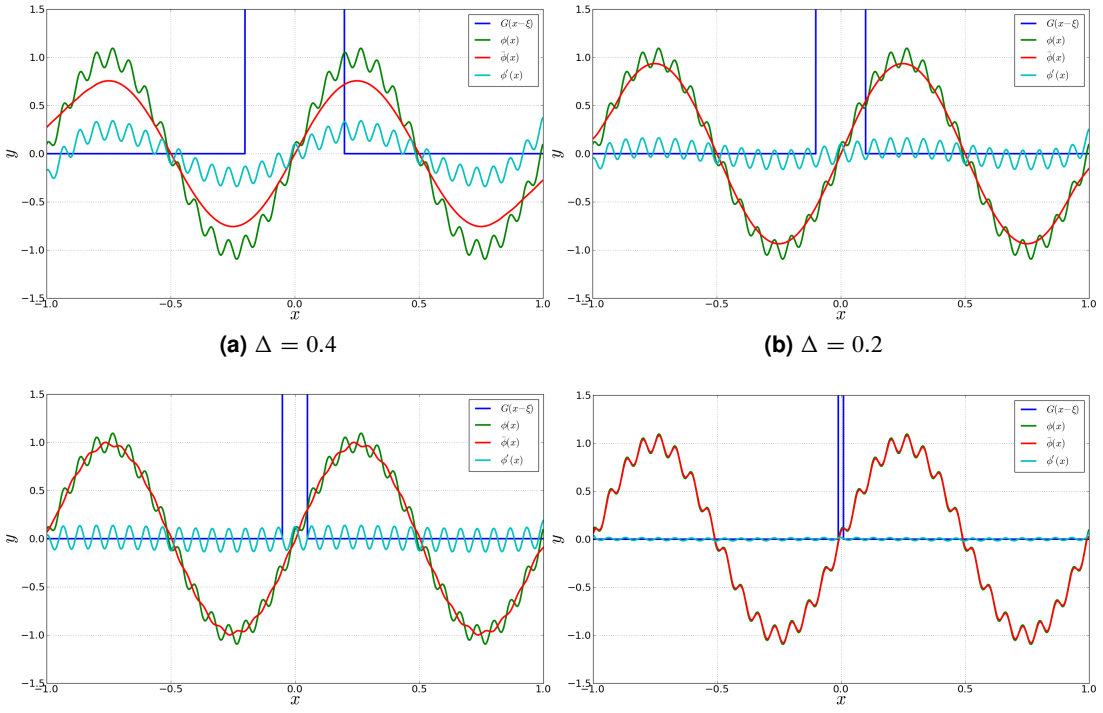


**(a)** $\Delta = 0.4$ **(b)** $\Delta = 0.2$

**(c)** $\Delta = 0.1$ **(d)** $\Delta = 0.02$

**Fig. 2.5:** An example of filtering for different filter sizes.

For the highest filter width $\Delta = 0.4$, Fig. 2.5 (a), filtered (or resolved) field contains only the large (most energetic) scales of motion. Subgrid-scales, $\phi'(x)$ need to be represented by a model. On the other hand, if the filter width is fine enough, $\Delta = 0.02$, resolved field contains almost all scales of motions, Fig. 2.5 (c). In this case, the effects of subgrid-scales are close to zero and our simulation approaches the level of direct numerical simulation.

The number of cells required for LES can be estimated. In wall-bounded flows, Choi and Moin [12] found that the number of cells required for wall-modeled LES is proportional to $Nc \propto Re_{L_x}$, and for wall-resolved LES $Nc \propto Re_{L_x}^{13/7}$, where $L_x$ represents the length of flat plate.

### Favre filtering

A typical way to simplify compressible equation set in LES is to use Favre-filtering, [24, 75]. In RANS framework, this method is known as Favre-averaging (see e.g. Wilcox [114]). For a transportable quantity $\phi$, Favre-filtering is defined as:

$$\tilde{\phi} = \frac{\overline{\rho\phi}}{\bar{\rho}}. \tag{2.33}$$

Favre-filtering of a product of two variables $\phi$ and $\psi$ is defined as:

$$\widetilde{\phi\psi} = \frac{\overline{\rho\phi\psi}}{\bar{\rho}}. \tag{2.34}$$

By using the Favre-filtering, compressible equations can be written in an analogous form

as incompressible equations:

$$\overline{\rho\phi} := \begin{cases} \rho\bar{\phi} & \text{if} \quad \rho = const \\ \bar{\rho}\tilde{\phi} & \text{if} \quad \rho \neq const \end{cases}. \tag{2.35}$$

## 2.3 Governing equations

### 2.3.1 Filtered equations

Governing equations in a compressible Newtonian fluid in a reference Cartesian coordinate system are continuity, momentum and energy equation, which can be written in the following form:

$$\frac{\partial \rho}{\partial t} + \frac{\partial(\rho u_i)}{\partial x_i} = 0, \tag{2.36}$$

$$\frac{\partial(\rho u_i)}{\partial t} + \frac{\partial(\rho u_i u_j)}{\partial x_j} = -\frac{\partial p}{\partial x_i} + \frac{\partial \sigma_{ij}}{\partial x_j} + \rho g_i, \tag{2.37}$$

$$\frac{\partial(\rho h)}{\partial t} + \frac{\partial(\rho u_i h)}{\partial x_i} = \kappa \frac{\partial^2(\rho h)}{\partial x_i \partial x_i}, \tag{2.38}$$

where

$$\sigma_{ij} = \mu\left(\frac{\partial u_i}{\partial x_j} + \frac{\partial u_j}{\partial x_i}\right) - \frac{2}{3}\mu\frac{\partial u_k}{\partial x_k}\delta_{ij}. \tag{2.39}$$

In equations (2.36) to (2.39) $\rho$, $\mu$, $\kappa$ and $C_p$ represent density, dynamic viscosity, thermal diffusivity and specific heat at constant pressure respectively; $u_i$, $h$ and $p$ are the Cartesian components of velocity vector, enthalpy and pressure, while $\delta_{ij}$ is the Kronecker delta.

Application of filtering on the above set of equations yields the following filtered equations:

$$\frac{\partial \tilde{\rho}}{\partial t} + \frac{\partial(\tilde{\rho}\bar{u}_i)}{\partial x_i} = 0, \tag{2.40}$$

$$\frac{\partial(\tilde{\rho}\bar{u}_i)}{\partial t} + \frac{\partial(\tilde{\rho}\overline{u_i u_j})}{\partial x_j} = -\frac{\partial \tilde{p}}{\partial x_i} + \frac{\partial \tilde{\sigma}_{ij}}{\partial x_j} + \tilde{\rho} g_i, \tag{2.41}$$

$$\frac{\partial(\tilde{\rho}\bar{h})}{\partial t} + \frac{\partial(\tilde{\rho}\overline{u_i h})}{\partial x_i} = \kappa \frac{\partial^2(\tilde{\rho}\bar{h})}{\partial x_i \partial x_i}. \tag{2.42}$$

Please note that in the remainder of this document a "bar" over a symbol, $\bar{\phi}$, represents the Favre filtering. In the equations (2.41) and (2.42) terms $\overline{u_i u_j}$ and $\overline{u_i h}$, also known as nonlinear terms, are not known and need to be further decomposed.

### 2.3.2 Decomposition of unknown terms

#### Momentum equation

First, we start with the decomposition of the term appearing in the filtered momentum equation (2.41). If we write the velocity field in the form of resolved and subgrid-scale quantities,

$$u_i = \bar{u}_i + u_i', \tag{2.43}$$

then, according to Leonard [65] (see also Sagaut [94]), nonlinear term can be decomposed as follows:

$$\begin{aligned}\overline{u_i u_j} &= \overline{(\bar{u}_i + u_i')(\bar{u}_j + u_j')} \\ &= \overline{\bar{u}_i \bar{u}_j} + \overline{\bar{u}_i u_j'} + \overline{u_i' \bar{u}_j} + \overline{u_i' u_j'},\end{aligned} \tag{2.44}$$

where

$$C_{ij} = \overline{\bar{u}_i u_j'} + \overline{u_i' \bar{u}_j}, \tag{2.45}$$

$$R_{ij} = \overline{u_i' u_j'}, \tag{2.46}$$

are the cross-stress tensor and the Reynolds subgird stress tensor respectively. The effects of subgrid-scales are grouped into the subgrid-scale stress tensor $\tau_{ij}$:

$$\tau_{ij} = \left(\overline{\bar{u}_i u_j'} + \overline{u_i' \bar{u}_j}\right) + \overline{u_i' u_j'} = C_{ij} + R_{ij}. \tag{2.47}$$

This decomposition is known as double decomposition. However, term $\overline{\bar{u}_i \bar{u}_j}$ cannot be directly calculated in LES and therefore it has to be decomposed further [I].

In order to express the nonlinear part only in the form of resolved fields ($\bar{u}_i$ and $\bar{u}_j$), Eq. (2.44) can be further decomposed as follows

$$\overline{u_i u_j} = \left(\overline{\bar{u}_i \bar{u}_j} - \bar{u}_i \bar{u}_j\right) + \overline{\bar{u}_i u_j'} + \overline{u_i' \bar{u}_j} + \overline{u_i' u_j'} + \bar{u}_i \bar{u}_j \tag{2.48}$$

$$= L_{ij} + C_{ij} + R_{ij} + \bar{u}_i \bar{u}_j, \tag{2.49}$$

where $L_{ij}$ is the Leonard tensor and it represents interaction among the large scales

$$L_{ij} = \left(\overline{\bar{u}_i \bar{u}_j} - \bar{u}_i \bar{u}_j\right). \tag{2.50}$$

This decomposition is known as Leonard, or triple decomposition. The subgrid-scale stress tensor is now

$$\tau_{ij} = \overline{u_i u_j} - \bar{u}_i \bar{u}_j \tag{2.51}$$

$$= L_{ij} + C_{ij} + R_{ij}. \tag{2.52}$$

Relation (2.51) is then substituted in Eq. (2.41) and the final form of the filtered momentum equation is obtained

$$\frac{\partial \tilde{\rho} \bar{u}_i}{\partial t} + \frac{\partial (\tilde{\rho} \bar{u}_i \bar{u}_j)}{\partial x_j} = -\frac{\partial \tilde{p}}{\partial x_i} + \frac{\partial \tilde{\sigma}_{ij}}{\partial x_j} - \frac{\partial (\tilde{\rho} \tau_{ij})}{\partial x_j} + \tilde{\rho} g_i. \tag{2.53}$$

Unknown term $\tau_{ij}$ has to be represent by a SGS model. Different approaches for modeling $\tau_{ij}$ will be discussed in the next section.

An important modification of the Leonard decomposition is presented in [32]. Since the Leonard term and subgrid-scale cross term are not Galilean invariant, Germano [32] proposed a modification of the original decomposition. According to Germano [32], SGS stress tensor is rewritten as follows

$$\tau_{ij} = \mathcal{L}_{ij} + \mathcal{C}_{ij} + \mathcal{R}_{ij}. \tag{2.54}$$

[I] At the early beginning of LES the usual approach was to approximate $\overline{\bar{u}_i \bar{u}_j} \simeq \bar{u}_i \bar{u}_j$. For further details about this approach and associated deficiencies see Leonard [65].

The modified Leonard stress, SGS cross stress and SGS Reynolds stress are

$$\mathcal{L}_{ij} = \overline{\bar{u}_i \bar{u}_j} - \bar{\bar{u}}_i \bar{\bar{u}}_j, \tag{2.55}$$

$$\mathcal{C}_{ij} = \overline{\bar{u}_i u_j' + u_i' \bar{u}_j} - \bar{\bar{u}}_i \overline{u_j'} - \overline{u_i'} \bar{\bar{u}}_j, \tag{2.56}$$

$$\mathcal{R}_{ij} = \overline{u_i' u_j'} - \bar{u}_i' \bar{u}_j'. \tag{2.57}$$

By redefining the SGS stresses on this manner, the Galilean invariance is assured.

This decomposition, known as consistent decomposition, represents the cornerstone for the dynamic procedure which will be introduced several years later. A connection between Leonard decomposition and consistent decomposition, as well as dynamic model, will be given in the next section.

#### Energy equation

The enthalpy from Eq. (2.42) is equal to $h = C_p \theta$, where $C_p$ and $\theta$ are specific heat at constant pressure and temperature respectively. Furthermore, it is assumed that $C_p$ can be taken out of the filtering operation, so that the unknown term in Eq. (2.42) can be written as follows:

$$\overline{u_i h} = C_p \overline{u_i \theta}, \tag{2.58}$$

Same as it was done for the momentum equation, velocity and temperature field can be expressed in the form of resolved and subrid quantities. Therefore, temperature is given as:

$$\theta = \bar{\theta} + \theta'. \tag{2.59}$$

Now, nonlinear term $\overline{u_i \theta}$ can be written as:

$$\overline{u_i \theta} = \overline{\bar{u}_i \bar{\theta}} + \overline{\bar{u}_i \theta'} + \overline{u_i' \bar{\theta}} + \overline{u_i' \theta'}, \tag{2.60}$$

which is further decomposed in the manner of triple decomposition to yield

$$\overline{u_i \theta} = \left( \overline{\bar{u}_i \bar{\theta}} - \bar{u}_i \bar{\theta} \right) + \overline{\bar{u}_i \theta'} + \overline{u_i' \bar{\theta}} + \overline{u_i' \theta'} + \bar{u}_i \bar{\theta}. \tag{2.61}$$

Subgrid-scale heat flux is then defined as follows:

$$q_i = \overline{u_i \theta} - \bar{u}_i \bar{\theta} \tag{2.62}$$

$$= \left( \overline{\bar{u}_i \bar{\theta}} - \bar{u}_i \bar{\theta} \right) + \overline{\bar{u}_i \theta'} + \overline{u_i' \bar{\theta}} + \overline{u_i' \theta'}. \tag{2.63}$$

Finally, upon substituting (2.58) and (2.62) into Eq. (2.42), the final form of the filtered energy equation is obtained

$$\frac{\partial (\tilde{\rho} C_p \bar{\theta})}{\partial t} + \frac{\partial (\tilde{\rho} C_p \bar{u}_i \bar{\theta})}{\partial x_i} = \kappa \frac{\partial^2 (\tilde{\rho} C_p \bar{\theta})}{\partial x_i \partial x_i} - \frac{\partial (\tilde{\rho} C_p q_i)}{\partial x_i}. \tag{2.64}$$

In order to close the filtered energy equation, subgrid-scale heat flux has to be modeled.

### 2.3.3 Test filtering and Germano identity

Germano Identity is the fundamental theory behind the dynamic procedure, a method which is widely used to calculate unknown model coefficients dynamically in time. The identity relates subgrid-scale momentum fluxes at two different filtering levels: test and grid filter. The test

filter, which is denoted by $\hat{()}$ throughout this work, is defined on the same way as the grid filter, Eq. (2.14),

$$\hat{\phi}(x) = \int_{\Omega} \hat{G}(x-\xi)\,\phi(\xi)d\xi. \tag{2.65}$$

The test filter width, $\hat{\Delta}$, is larger than that of grid filter, and it is a usual choice that the ratio of the filters is two, i.e. $\hat{\Delta}/\Delta = 2$. The test-filtering operation is then applied on the grid-filtered momentum equation, Eq. (2.41), which produces a test-filtered momentum equation. Afterwards, by analogy to the grid-filtered momentum equation, the turbulent stresses at test-filtering level (subtest-scale stress tensor) are defined as:

$$T_{ij} = \widehat{\overline{u_i u_j}} - \hat{\bar{u}}_i \hat{\bar{u}}_j. \tag{2.66}$$

Germano [33] observed that the resolved stress tensor, $\mathcal{L}_{ij}$, is equal to the difference of the turbulent stresses at the test-filtering level and the test-filtered value of turbulent stresses at the grid-filtering level. This statement reads as follows:

$$\mathcal{L}_{ij} = T_{ij} - \hat{\tau}_{ij} \tag{2.67}$$

The expression (2.67) is known as Germano identity and will be extensively used in this work. The resolved stress tensor, $\mathcal{L}_{ij}$, can be explicitly evaluated from the large scales

$$\mathcal{L}_{ij} = \widehat{\bar{u}_i \bar{u}_j} - \hat{\bar{u}}_i \hat{\bar{u}}_j. \tag{2.68}$$

Germano identity, (2.67), is the cornerstone of the dynamic modeling. In his further work, Germano et al. [34] exploited it to derive equations for the constant appearing in the Smagorinsky model, Smagorinsky [98].

Example of grid and test filtering is given in Fig. 2.6. Cutoff wave numbers $k_g$ and $k_t$ correspond to the grid and test filters respectively, $\tau_{ij}$ and $T_{ij}$ represent subgrid- and subtest-scale stress tensors, while $u_i^g$ and $u_i^t$ are resolved velocities.

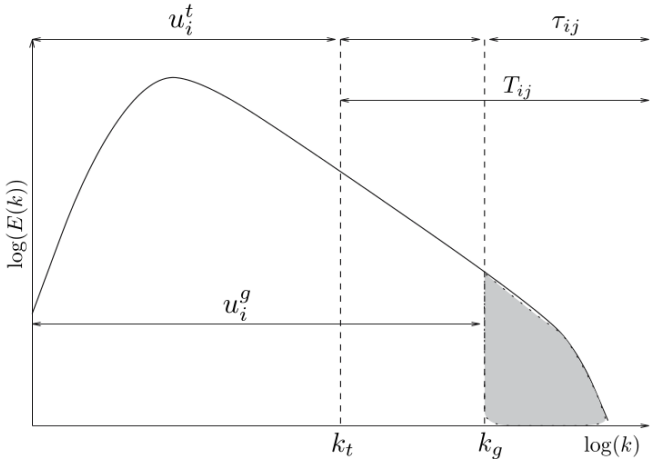


**Fig. 2.6:** Schematic view of two filtering levels; lower-case letters g and t stand for grid and test filter. Adjusted from [94].

**Extension for the energy equation**

Germano identity can be also written for the subgrid-scale heat (scalar) fluxes. SGS heat fluxes at grid and test filtering levels are

$$q_i = \overline{u_i\theta} - \bar{u}_i\bar{\theta}, \tag{2.69}$$

$$Q_i = \widehat{\overline{u_i\theta}} - \hat{\bar{u}}_i\hat{\bar{\theta}}. \tag{2.70}$$

Substituting the test-filtered subgrid-scale heat flux (2.69) from the heat flux at subtest level, (2.70), yields

$$P_i = Q_i - \hat{q}_i = \widehat{\bar{u}_i\bar{\theta}} - \hat{\bar{u}}_i\hat{\bar{\theta}}. \tag{2.71}$$

"Test window" (resolved) heat flux, $P_i$, can be directly calculated from the resolved fields. Relation (2.71) can be applied to determine subgrid-scale turbulent Prandtl number dynamically. In the present work, relation (2.71) is utilized to determine coefficients of the new model which will be proposed in Chapter 3.

## 2.4 Subgrid-scale modeling for momentum equation

In order to close the filtered momentum, (2.53), and energy equations, (2.64), unknown terms $\tau_{ij}$ and $q_i$, which represent the influence of the unresolved on the resolved scales, have to be modeled. This process is known as subgrid-scale modeling and it can be divided in two modeling strategies (see [94])

- Structural modeling. Unknown terms are represented by approximations constructed from resolved scales.
- Functional modeling. Instead of modeling the unknown terms, the action of subgrid on the resolved scales is modeled.

When developing a new SGS model it has to be kept in mind that the model has to fulfill some of the physical and numerical constraints (see [31]):

- Physical constraints
  - Contribution of the SGS model has to vanish if the grid resolution is fine enough to resolve even the smallest scales or if there is no fluctuations of the considered field (velocity, temperature, ...);
  - The model has to produce effects of the same kind as the modeled terms.
- Numerical constraints
  - Computational costs have to be acceptable;
  - Computational stability should not be affected.

### 2.4.1 Smagorinsky model

The Smagorinsky model represents a pioneering work in LES, originally proposed by Smagorinsky [98] in 1963. The model is based on two steps (see e.g. [28, 88]): first, linear SGS viscosity model is used to parametrize SGS stress tensor; second, analogy to the mixing length hypothesis is used to model SGS viscosity.

SGS stress tensor is related to the resolved scales by the following relation

$$\tau_{ij} = -2\nu_{sgs}\bar{S}_{ij}, \tag{2.72}$$

where

$$\bar{S}_{ij} = \frac{1}{2}\left(\frac{\partial \bar{u}_i}{\partial x_j} + \frac{\partial \bar{u}_j}{\partial x_i}\right). \tag{2.73}$$

In the second step, SGS viscosity is defined as

$$\nu_{sgs} = l^* q^*, \tag{2.74}$$

where, $l^*$ and $q^*$ are characteristic length and velocity respectively. For characteristic velocity a product of the characteristic length and norm of $\bar{S}_{ij}$ is used $q^* = l^*|\bar{S}|$, where $|\bar{S}| = \sqrt{2\bar{S}_{ij}\bar{S}_{ij}}$. A natural choice for characteristic length in LES is filter width $\Delta$. In the Smagorinsky model, filter width multiplied by a model coefficient $C_S$ is used for the characteristic length, $l^* = C_S\Delta$. Hence, SGS viscosity is defined as

$$\begin{aligned}\nu_{SGS} &= l^* l^* |\bar{S}| \\ &= (C_S\Delta)^2|\bar{S}|.\end{aligned} \tag{2.75}$$

SGS viscosity from Eq. (2.72) is replaced with (2.75), which yields the relation for SGS stress tensor:

$$\tau_{ij} = -(C_S\Delta)^2|\bar{S}|\bar{S}_{ij}. \tag{2.76}$$

Model coefficient $C_S$ is known as Smagorinsky coefficient, and its value can be determined depending on the flow type. However, there is no an universal value for $C_S$ which is suitable for all flow types and different values can be found in the literature. For example, in the case of isotropic turbulence, $C_S$ can vary between $0.19$ and $0.24$, while for the sher flows the value has to be reduced up to $0.065$ or $0.1$ (see [28]). Reduction of the $C_S$ value in shear flows was necessary due to the excessive dissipation produced by the model.

Another disadvantage of the Smagorinsky model considers the transfer of energy between scales. The rate of transfer of energy from the resolved to the unresolved scales is given by the relation (see [88])

$$\mathcal{P}_{sgs} \equiv -\tau_{ij}\bar{S}_{ij}, \tag{2.77}$$

and after using the Smagorinsky model (2.72) for $\tau_{ij}$

$$\mathcal{P}_{sgs} = 2\nu_{sgs}\bar{S}_{ij}\bar{S}_{ij}. \tag{2.78}$$

Since the SGS viscosity is always positive, $\mathcal{P}_{sgs}$ is also always positive, which means that it appears as a source term in the equation for SGS kinetic energy. Hence, the energy is transfered only from the resolved to the subgrid scales and the revers process is not possible. Reverse transfer of energy (from small to large scales) is known as backscatter and it is experimentally confirmed.

The Smagorinsky model can be improved by combining it with other models or by providing methods to calculate model coefficient independently of flow type.

### 2.4.2 Dynamic models

#### Dynamic Smagorinsky model

The idea of using the identity (2.67) to construct more sophisticated SGS models was firstly introduced by Germano et al. [34] and it is also the first dynamic model published in the literature. Led by inability of the Smagorinsky model to predict correctly with a single universal constant different flow types (shear, rotating, transitional flows, etc.), Germano and co-workers developed a new eddy viscosity model in which the smallest resolved scales are utilized to determine the subgrid-scale momentum fluxes. Rather than being prescribed, the Smagorinsky model coefficient was calculated dynamically in time allowing the model to adjust to different flow regimes.

To derive a new model for SGS stress tensor, Germano and co-workers assumed that the same closure approximation, in this case the Smagorinsky [98] model, can be used for both $\tau_{ij}$ and $T_{ij}$:

$$\tau_{ij} - \frac{\delta_{ij}}{3}\tau_{kk} \simeq m_{ij} = -2C\bar{\Delta}^2|\bar{S}|\bar{S}_{ij}, \tag{2.79}$$

$$T_{ij} - \frac{\delta_{ij}}{3}T_{kk} \simeq M_{ij} = -2C\hat{\bar{\Delta}}^2|\hat{\bar{S}}|\hat{\bar{S}}_{ij}, \tag{2.80}$$

where $\hat{\bar{S}}_{ij} = \frac{1}{2}\left(\frac{\partial\hat{\bar{u}}_i}{\partial x_j} + \frac{\partial\hat{\bar{u}}_j}{\partial x_i}\right)$ is test filtered strain rate tensor and its norm is $|\bar{S}| = \sqrt{2\bar{S}_{ij}\bar{S}_{ij}}$ and $|\hat{\bar{S}}| = \sqrt{2\hat{\bar{S}}_{ij}\hat{\bar{S}}_{ij}}$. Model coefficient $C$ is equal to the square of the original Smagorinsky coefficient $C_S$ and is assumed to be equal for the both filtering levels.

Equations (2.79) and (2.80) are substituted into (2.67) (which is again given here for completeness)

$$\mathcal{L}_{ij} = T_{ij} - \widehat{\tau}_{ij},$$

and the resulting expression is contracted with $\bar{S}_{ij}$ to yield:

$$\mathcal{L}_{ij}\bar{S}_{ij} = -2C\Big(\hat{\bar{\Delta}}^2|\hat{\bar{S}}|\hat{\bar{S}}_{ij}\bar{S}_{ij} - \bar{\Delta}^2|\bar{S}|\bar{S}_{ij}\bar{S}_{ij}\Big). \tag{2.81}$$

In general, model coefficient $C$ can be determined from the above equation. However, initial tests showed that the quantity in parentheses can become zero making the $C$ indeterminate or ill-conditioned. Therefore, to alleviate this problem, authors have averaged Eq. (2.81) over the homogeneous directions, so that for the case of turbulent channel flow it was assumed that $C$ is only a function of the wall-normal direction. Dynamic equation for model coefficient in its averaged form is given as follows:

$$C(y,t) = -\frac{1}{2}\frac{\langle\mathcal{L}_{kl}\bar{S}_{kl}\rangle}{\hat{\bar{\Delta}}^2\langle|\hat{\bar{S}}|\hat{\bar{S}}_{mn}\bar{S}_{mn}\rangle - \bar{\Delta}^2\langle|\bar{S}|\bar{S}_{pq}\bar{S}_{pq}\rangle}, \tag{2.82}$$

where $\langle\rangle$ represents averaging over a plane parallel to the wall and $t$ stands for time. Finally, by substituting (2.82) into (2.79), the new dynamic eddy-viscosity model is derived:

$$m_{ij} = \frac{\langle\mathcal{L}_{kl}\bar{S}_{kl}\rangle}{\frac{\hat{\bar{\Delta}}^2}{\bar{\Delta}^2}\langle|\hat{\bar{S}}|\hat{\bar{S}}_{mn}\bar{S}_{mn}\rangle - \langle|\bar{S}|\bar{S}_{pq}\bar{S}_{pq}\rangle}|\bar{S}|\bar{S}_{ij}. \tag{2.83}$$

Since its beginning, the dynamic model given by (2.83) showed some favorable properties. It vanishes in the case of laminar flow or at solid boundaries and has correct asymptotic

behavior without the use of damping functions. Furthermore, it is reported that the model can account for backscatter. However, the rather arbitrary averaging over the homogeneous direction reduces the functionality of the model for the flows within complex geometries, i. e. flows without homogeneous directions.

#### Dynamic Smagorinsky model - Lilly's modification

Even though that the dynamic Smagorinsky model showed some promising results and drew significant attention at the beginning, the model suffered because of the stability reasons. Namely, it was found that the denominator of Eq. (2.82) could vanish or become very small eventually leading to the computational instability. Averaging of the model coefficient over the planes parallel to the channel walls were proposed in order to stabilize the computation. However, this method reduces some fundamental advantages of the model and restricts its applicability to the flows with at least one homogeneous direction. In order to remove the singularity associated with the original formulation, Lilly [66] modified the original model by using a least squares technique to minimize the error between the closure approximations and resolved stresses.

Starting from the Germano identity and after the Smagorinsky model was applied for $T_{ij}$ and $\tau_{ij}$, Eq. (2.81) can be rewritten in a slightly modified form:

$$\mathcal{L}_{ij} - \frac{1}{3}\delta_{ij}\mathcal{L}_{kk} = 2CM_{ij}, \tag{2.84}$$

$$M_{ij} = \hat{\Delta}^2|\hat{\bar{S}}|\hat{\bar{S}}_{ij} - \Delta^2\widehat{|\bar{S}|\bar{S}_{ij}}. \tag{2.85}$$

Since the system of equations (2.84) is overdetermined (five independent equations in one unknown) Lilly [66] proposed to find an optimal value for $C$ by minimizing the error of (2.84) by applying a least squares method. To do so, a square of the error in (2.84) has to be defined:

$$Q = \left(\mathcal{L}_{ij} - \frac{1}{3}\delta_{ij}\mathcal{L}_{kk} - 2CM_{ij}\right)^2. \tag{2.86}$$

Now, since $Q$ is a function of the model coefficient $C$ it is necessary to find an optimal value for $C$ which yields the minimum of $Q$. This is done by setting the first derivative of $Q$ with respect to $C$ to zero:

$$\frac{\partial Q}{\partial C} = 0. \tag{2.87}$$

Finally, expression for $C$ is obtained as:

$$C = \frac{1}{2}\frac{\mathcal{L}_{ij}M_{ij}}{M_{ij}^2}. \tag{2.88}$$

Equation (2.88) gives either positive or negative $C$ values meaning that the model does not exclude backscatter.

Advantage of the model (2.88) over (2.82) is, as reported in [66], that the denominator of (2.88) can vanish only if each of the five independent component of $M_{ij}$ vanish separately. However, the author also reported that when applied to individual grid points the method can produce high $C$ values which leads to computational instability. Therefore, some sort of local averaging or truncation of the isolated large values were suggested by the author.

### Localized dynamic model

Dynamic Smagorinsky, Eq. (2.82), and its modified version, Eq. (2.88) are derived assuming that the model coefficient $C$ does not depend on the position which is, in fact, an arbitrary assumption. Ignoring that $C$ is spatially dependent, makes possible to exclude it from the filtering operations in (2.81) and (2.85), so that the integral equations are reduced to the algebraic equations.

This mathematical inconsistency is removed in the work of Ghosal et al. [36] who proposed a method based on the variational formulation. As a result, an integral equation, whose solution determines $C$ as a function of position and time, is derived. New model is applicable also to the flows without homogeneous directions and does not require any kind of local averaging. In order to improve the computational stability, model coefficient $C$ is restricted only to the positive values. Furthermore, the authors demonstrated that the expressions for $C$ obtained by Germano et al. [34] and Lilly [66] can be derived by adopting some constraints in the variational formulation.

If $C$ is a function of position, than it cannot be removed from filtering operations in (2.81) and (2.84), so that the Germano identity yields:

$$\mathcal{L}_{ij} - \frac{1}{3}\delta_{ij}\mathcal{L}_{kk} = \alpha_{ij}C - \widehat{\beta_{ij}C}, \tag{2.89}$$

where

$$\alpha_{ij} = -2\hat{\Delta}^2|\hat{\bar{S}}|\hat{\bar{S}}_{ij}, \tag{2.90}$$

$$\beta_{ij} = -2\Delta^2|\bar{S}|\bar{S}_{ij}. \tag{2.91}$$

The error in (2.89) can be defined as:

$$E_{ij}(x) = \mathcal{L}_{ij} - \frac{1}{3}\delta_{ij}\mathcal{L}_{kk} - \alpha_{ij}C + \widehat{\beta_{ij}C}, \tag{2.92}$$

where $x$ is a position vector. Optimal function $C(x)$ which minimizes the error $E_{ij}(x)$ is obtained by solving the variational problem and for the further details please refer to Ghosal et al. [36].

Solution of the variational problem leads to the Fredholm's integral equation of the second kind which has to be solved numerically. By using this approach to formulate a dynamic SGS model, mathematical inconsistency associated with the assumption of the uniform, spatially-independent, model coefficient is removed, thereby putting the modeling on a strong mathematical background. However, instability associated with the negative eddy viscosity (caused by the negative $C$ values) remained, and Ghosal and co-authors eliminated it by constraining $C$ only to positive values, i.e. $C \geq 0$. Finally, an expression for model coefficient $C$ as a function of position is derived:

$$C(x) = \left[ f(x) + \int \mathcal{K}(x,y)dy \right]_+, \tag{2.93}$$

where $+$ denotes the positive part and:

$$\mathcal{K}(x,y) = \frac{\mathcal{K}_{\mathcal{A}}(x,y) + \mathcal{K}_{\mathcal{A}}(y,x) - \mathcal{K}_{\mathcal{J}}(x,y)}{\alpha_{kl}(x)\alpha_{kl}(x)}, \tag{2.94}$$

$$\mathcal{K}_{\mathcal{A}}(x,y) = \alpha_{ij}(x)\beta_{ij}(y)G(x,y), \tag{2.95}$$

$$\mathcal{K}_{\mathcal{J}}(x,y) = \beta_{ij}(x)\beta_{ij}(y)\int G(z,x)G(z,y)dz. \tag{2.96}$$

Negative $C$ values, which may occur in some grid points, are simply replaced with zero. By doing so, eddy viscosity is limited to positive values and computational stability is increased. Unfortunately, since the eddy viscosity cannot become negative, the model is purely dissipative and cannot predict backscatter.

### Localized dynamic one equation

By allowing the model coefficient $C$ to have either signs, the model is able to reproduce backscatter of energy. However, the Smagorinsky model does not contain the information about the available energy in the subgrid scales. This means that, theoretically, negative SGS viscosity can drain more than available amount of energy from the subgrid scales. In order to solve this problem, Ghosal et al. [36] have included the transport equation for subgrid-scale kinetic energy and made the SGS viscosity dependent on it. By doing so, the information regarding the total amount of energy contained in the subgrid scales is included in the model. If in some point in the flow field backscatter appears, SGS kinetic energy will decrease toward zero eventually quenching the backscatter and removing the numerical instabilities. This model is also known as dynamic one equation model and is very often used in LES.

In the same manner as in the Smagorinsky model, SGS viscosity can be defined as a product of characteristic length scale and characteristic velocity. In LES, an obvious choice for the characteristic length is a grid filter width, $\Delta$, while, unlike the Smagorinsky model, a square root of the SGS kinetic energy is used for the characteristic velocity. Hence, SGS viscosity can be written as

$$\nu_{sgs} = C\Delta k^{1/2}, \tag{2.97}$$

which yields

$$\tau_{ij} - \frac{1}{3}\delta_{ij}\tau_{kk} = -2C\Delta k^{1/2}\bar{S}_{ij}, \tag{2.98}$$

$$T_{ij} - \frac{1}{3}\delta_{ij}T_{kk} = -2CK^{1/2}\hat{\bar{S}}_{ij}, \tag{2.99}$$

where subgrid-scale and subtest scale kinetic energies $k$ and $K$ are given as follows

$$k = \frac{1}{2}\left(\overline{u_i u_i} - \bar{u}_i\bar{u}_i\right) = \frac{1}{2}\tau_{ii}, \tag{2.100}$$

$$K = \frac{1}{2}\left(\widehat{\overline{u_i u_i}} - \hat{\bar{u}}_i\hat{\bar{u}}_i\right) = \frac{1}{2}T_{ii}. \tag{2.101}$$

Both of these quantities are unknown, but they are related by the relation which can be derived by taking the trace of the Germano identity (2.67), which yields

$$K = \hat{k} + \frac{1}{2}\mathcal{L}_{ii}. \tag{2.102}$$

Now, equations (2.100) and (2.101) are used in (2.67) to obtain Eq. (2.89), but with $\alpha_{ij}$ and $\beta_{ij}$ being calculated as

$$\alpha_{ij} = -2\hat{\Delta}K^{1/2}\hat{\bar{S}}_{ij}, \tag{2.103}$$

$$\beta_{ij} = -2\Delta k^{1/2}\bar{S}_{ij}. \tag{2.104}$$

The only unknown term, beside the model coefficient $C$, is SGS kinetic energy, which is obtained by solving the modeled transport equation

$$\frac{\partial k}{\partial t} + \bar{u}_j\frac{\partial k}{\partial x_j} = -\tau_{ij}\bar{S}_{ij} - C^*\frac{k^{3/2}}{\Delta} + \frac{\partial}{\partial x_j}\left(D\Delta k^{1/2}\frac{\partial k}{\partial x_j}\right) + \frac{1}{Re}\frac{\partial^2 k}{\partial x_j \partial x_j}, \tag{2.105}$$

in which are $C^*$ and $D$ non-negative dimensionless functions of position and time. These coefficients are dynamically calculated (see [36] for details).

The method is independent of any subgrid-scale model and can be applied to determine one or more model coefficients, depending on the SGS model used. However, when applied to high Reynolds number flows in complex geometries, high wall layer resolution is needed.

#### Localized dynamic one equation model - scale similarity assumption

Implementation of the Localized dynamic model - k equation (see above) requires an expensive iterative procedure. Kim and Menon [54] proposed a localized dynamic one equation model based on the scale similarity assumption which does not require considerably larger computational resources than the simple dynamic Smagorinsky model.

Kim and Menon [54] have considered other form of stress tensor at test filtering level; the one that does not contain additional unknown terms

$$\begin{aligned} t_{ij} &= \widehat{\bar{u}_i \bar{u}_j} - \hat{\bar{u}}_i \hat{\bar{u}}_j \\ &= 2C\hat{\Delta}\left[\frac{1}{2}\left(\widehat{\bar{u}_i \bar{u}_i} - \hat{\bar{u}}_i \hat{\bar{u}}_i\right)\right]^{1/2} \hat{\bar{S}}_{ij} + \frac{2}{3}\delta_{ij}\left[\frac{1}{2}\left(\widehat{\bar{u}_i \bar{u}_i} - \hat{\bar{u}}_i \hat{\bar{u}}_i\right)\right] \end{aligned} \tag{2.106}$$

Coefficient $C$ is then obtained by applying a least square method which yields

$$C = \frac{1}{2}\frac{t_{ij} M_{ij}}{M_{ij} M_{ij}}, \tag{2.107}$$

where

$$M_{ij} = \hat{\Delta}\left[\frac{1}{2}\left(\widehat{\bar{u}_i \bar{u}_i} - \hat{\bar{u}}_i \hat{\bar{u}}_i\right)\right]^{1/2} \hat{\bar{S}}_{ij}. \tag{2.108}$$

It is reported in [30, 54] that the denominator of (2.107) is always nonzero which removes possible singularities.

Dissipation rate from transport equation for SGS kinetic energy is given as

$$\epsilon = c_\epsilon \frac{k^{3/2}}{\Delta}, \tag{2.109}$$

and the unknown coefficient is calculated form the following relation

$$c_\epsilon = \frac{\nu\left[\widehat{\frac{\partial \bar{u}_i}{\partial x_j}\frac{\partial \bar{u}_i}{\partial x_j}} - \frac{\partial \hat{\bar{u}}_i}{\partial x_j}\frac{\partial \hat{\bar{u}}_i}{\partial x_j}\right]}{\left[\frac{1}{2}\left(\widehat{\bar{u}_i \bar{u}_j} - \hat{\bar{u}}_i \hat{\bar{u}}_j\right)\right]^{3/2} / \bar{\Delta}}, \tag{2.110}$$

which completes the model.

### 2.4.3 Scale similarity and mixed models

Other type of models, which are very often used in LES, are scale similarity and mixed models. Similarity models assume that the SGS stress tensor is proportional to the resolved stress:

$$\tau_{ij} = c_b\left(\widehat{\bar{u}_i \bar{u}_j} - \hat{\bar{u}}_i \hat{\bar{u}}_j\right), \tag{2.111}$$

where $c_b$ is a constant of proportionality. However, the model given by the Eq. (2.111) is not dissipative enough which can lead to the numerical instabilities. Therefore, similarity models are very often combined with other dissipative models.

When combined with the Smagorinsky model, resulting mixed model reads

$$\tau_{ij} - \frac{\delta_{ij}}{3}\tau_{kk} = -2C\Delta^2|\bar{S}|S_{ij} + \mathcal{L}_{ij} - \frac{\delta_{ij}}{3}\mathcal{L}_{kk}, \tag{2.112}$$

where $C$ represents a square of the original Smagorinsky coefficient. Model coefficients can be prescribed or, alternatively, the dynamic procedure can be used for their evaluation in time, see e.g. Zang et al. [119].

## 2.5 Subgrid-scale modeling for energy equation

A brief description of existing SGS heat flux models is showed in the previous chapter. More details are given next.

### 2.5.1 Scalar subgrid-scale diffusivity

This is the most common approach to calculate subgrid-scale heat flux, which is given as a product of a scalar subgrid-scale diffusivity and gradient of the resolved temperature field:

$$q_j = -\kappa_{sgs}\frac{\partial\bar{\theta}}{\partial x_j}, \tag{2.113}$$

in which $\kappa_{sgs}$ is subgrid-scale diffusivity and $\bar{\theta}$ is the resolved temperature field.

#### Constant $Pr_{sgs}$ approach

This approach is based on the Reynolds analogy and the concept of subgrid-scale turbulent Prandtl number, $Pr_{sgs}$. Here, one has to provide a single constant value for $Pr_{sgs}$ which is, in most cases, assumed to be between $0.3$ and $1$. SGS diffusivity is calculated as the ratio of SGS viscosity and $Pr_{sgs}$:

$$\kappa_{sgs} = \frac{\nu_{sgs}}{Pr_{sgs}}, \tag{2.114}$$

where $\nu_{sgs}$ is subgrid-scale viscosity. SGS heat flux is then obtained from the following relation:

$$q_j = -\frac{\nu_{sgs}}{Pr_{sgs}}\frac{\partial\bar{\theta}}{\partial x_j}. \tag{2.115}$$

Very often is the one equation model used to close the momentum equation. This yields the following expression for SGS diffusivity:

$$\kappa_{sgs} = \frac{c_\nu}{Pr_{sgs}}\Delta k^{1/2}. \tag{2.116}$$

Subgrid-scale turbulent Prandtl number for forced convection heat transfer to air in turbulent channel ranges from $Pr_{sgs} = 0.4$ in the center of the channel to $Pr_{sgs} = 1$ near the walls, Kim and Moin [53]. Investigations, e.g. Pallares and Davidson [82], showed that a simple choice of $Pr_{sgs} = 0.4$ usually gives good agreement with DNS data and experimental measurements. However, if we consider some other fluids than air, for example water or liquid metals, whose molecular Prandtl number significantly differs from one, the proper choice of $Pr_{sgs}$ is not known. Moreover, if the fluid experiences action of some volumetric forces, like buoyancy force, additional modeling of turbulent heat flux should be considered. According to Sagaut [94], values for $Pr_{sgs}$ found in the literature range from 0.1 to 1.

This approach provides satisfactory good results for forced convection heat transfer and for flows which do not experience some external effects, e.g. system rotation or buoyancy force. However, the constant $Pr_{sgs}$ approach may be insufficient if the mesh resolution is fine enough to resolve the velocity field, while the temperature still remains unresolved, which may happen if working fluid has molecular Prandtl number larger than one - water is a typical example. If this is the case, Eq. (2.114) will yield a zero thermal diffusivity even though that subgrid-scale heat flux still exists. Moreover, the $Pr_{sgs}$ is case sensitive and it depends on both molecular

fluid properties and flow parameters. Despite the aforementioned shortcomings, this method is still the most popular one among engineers.

Based on the well known Smagorinsky model, Smagorinsky [98], Eidson [22] derived a new model for natural convection by including a buoyancy contribution in the subgrid-scale turbulent kinetic energy production term. Eq. (2.114) is used to calculate subgrid-scale diffusivity and the effects of buoyancy are included in an equation for SGS viscosity:

$$\nu_{sgs} = \frac{(C\Delta)^2}{2^{1/2}} \left( \bar{S}^2 - 2\frac{Pr\, Ra}{Pr_{sgs}} \frac{\partial \bar{\theta}}{\partial x_3} \right)^{1/2}, \tag{2.117}$$

where $C$ is the Smagorinsky constant and $x_3$ is the coordinate in the direction of gravity. Values of $C$ and $Pr_{sgs}$ used in the simulation were $C = 0.21$ and $Pr_{sgs} = 0.4$. First part of the expression (2.117) represents the original Smagorinsky model. The model was evaluated by performing a large eddy simulation of turbulent natural convection. Working fluid was air ($Pr = 0.71$) and six different Rayleigh numbers are used $Ra = 1 \times 10^4$, $3.8 \times 10^5$, $6.3 \times 10^5$, $1.4 \times 10^6$, $2.5 \times 10^6$ and $1.0 \times 10^7$ The simulation results showed good agreement with the experimental measurements. Furthermore, the author suggested that the use of a transport equation for SGS kinetic energy, which could be used as a velocity time scale, would improve modeling.

### Dynamic models for $Pr_{sgs}$

Applicability of the model Eq. (2.113) can be increased by providing the methods to calculate $Pr_{sgs}$ depending on the fluid properties and on the flow and heat transfer characteristics. This means that the subgrid-scale turbulent Prandtl number will be made space and time dependent. Very popular and effective methods to calculate $Pr_{sgs}$ and other model coefficients are based on the dynamic procedure initially introduced by Germano et al. [34] and subsequently revised by Moin et al. [75] and Lilly [66]. $Pr_{sgs}$ evaluated by the dynamic procedure is time dependent and, if averaging and constraints on the model coefficients are not applied, it is also space dependent.

Moin et al. [75] extended the dynamic model of Germano et al. [34] to the compressible flows and transport of passive scalar. This is also the first published application of dynamic procedure to calculate SGS turbulent Prandtl number. By means of dynamic procedure, $Pr_{sgs}$ is calculated as:

$$Pr_{sgs} = C \left\langle \hat{\Delta}^2 \hat{\bar{\rho}} |\hat{\tilde{S}}| \frac{\partial \hat{\tilde{\theta}}}{\partial x_k} \frac{\partial \tilde{\theta}}{\partial x_k} - \widehat{\Delta^2 \bar{\rho} |\tilde{S}| \frac{\partial \tilde{\theta}}{\partial x_k} \frac{\partial \tilde{\theta}}{\partial x_k}} \right\rangle \times \left\langle \left( \frac{1}{\hat{\bar{\rho}}} \widehat{\bar{\rho}\tilde{v}_k} \widehat{\bar{\rho}\tilde{\theta}} - \widehat{\bar{\rho}\tilde{v}_k \tilde{\theta}} \right) \frac{\partial \tilde{\theta}}{\partial x_k} \right\rangle^{-1}, \tag{2.118}$$

where $C$ is model coefficient from momentum equation, $\Delta$, $\rho$ and $\theta$ are filter width, density and temperature, $v_k$ is the velocity component in the $k$ th direction and $|S|$ is the second norm of the SGS stress tensor. Grid filtering is given by $\bar{(\cdot)}$, $\hat{(\cdot)}$ represents test filtering and $\tilde{(\cdot)}$ is Favre filtering. Then, subgrid-scale heat flux can be calculated as follows

$$q_k = \frac{\bar{\rho \nu}_T}{Pr_{sgs}} \frac{\partial \tilde{\theta}}{\partial x_k} \tag{2.119}$$

However, because of the numerical instability, appropriate averaging, i.e. over the homogeneous directions, is applied. The expression for $Pr_{sgs}$ is analyzed using DNS data of isotropic turbulence, homogeneous shear flow and turbulent channel flow. For the case of isotropic turbulence it is found out that initial temperature spectrum has significant effect on

the $Pr_{sgs}$. The value of $Pr_{sgs}$ for the case where the initial temperature field was obtained from the equation of state and had an initial spectrum similar to the pressure spectrum, was around $0.4$. For the flow field obtained from the simulation started with zero-fluctuations pressure and temperature fields, the evaluated $Pr_{sgs}$ was approximately $0.85$. The results pointed out to a deficiency of the model with fixed, constant subgrid-scale turbulent Prandtl number which is independent of the instantaneous flow conditions. Furthermore, the influence of the mesh resolution and molecular Prandtl number on $Pr_{sgs}$ is investigated for the case of homogeneous shear flow. Three different molecular Prandtl numbers were tested, $Pr = 0.2, 0.7$ and $2$. $Pr_{sgs}$ varied between $0.6$ and $1.6$ for the extreme case: coarse grid and high molecular Prandtl number, $Pr = 2$. Variations of $Pr_{sgs}$ were reduced for the finer grids. For the case of turbulent channel flow, again three different molecular Prandtl numbers were tested: $Pr = 0.1, 0.7$ and $2$. Behavior of $Pr_{sgs}$ is investigated in the direction normal to the wall and averaging is applied over the homogeneous directions. Contrary to the homogeneous shear flow test case, it was observed that the lowest molecular Prandtl number, $Pr = 0.1$, generates highest variations of $Pr_{sgs}$. These results add to the importance of flow configuration on the $Pr_{sgs}$.

Both dynamic SGS stress model of Germano et al. [34] and dynamic model for SGS turbulent Prandtl number flawed from being numerically unstable. To avoid the stability problem, the authors applied averaging of numerator and denominator of the equations for model coefficients over homogeneous directions. Lilly [66] recognized that additional averaging perhaps eliminates some of the conceptual advantages of their formulations. In his work, Lilly [66], applied a least squares technique to minimize the difference between the closure assumptions and resolved stresses. This method improved numerical stability of the original dynamic model without introducing additional averaging. In the same paper, Lilly [66] also proposed a method to calculate subgrid-scale turbulent Prandtl number where a least squares technique is used to find an optimal value for $Pr_{sgs}$:

$$\frac{1}{Pr_{sgs}} = \frac{M_{ik}^2}{L_{ik}M_{ik}} \frac{P_j R_j}{R_j^2}, \tag{2.120}$$

where

$$L_{ik} = -\widehat{\bar{u}_i \bar{u}_k} + \hat{\bar{u}}_k \hat{\bar{u}}_k, \tag{2.121}$$

$$M_{ik} = \Delta^2 |\hat{\bar{S}}| \hat{\bar{S}}_{ik} - \Delta^2 \widehat{|\bar{S}| \bar{S}_{ik}}, \tag{2.122}$$

$$R_j = \hat{\Delta}^2 |\hat{\bar{S}}| \widehat{\frac{\partial \bar{\theta}}{\partial x_j}} - \Delta^2 \widehat{|\bar{S}| \frac{\partial \bar{\theta}}{\partial x_j}}. \tag{2.123}$$

$P_j$ is calculated from Eq. (2.71).

The Lilly's method has drawn a lot of attention among researchers and in the next twenty years many of them applied the idea of minimizing the error between resolved heat fluxes and closure approximations by means of the least squares technique in order to determine model coefficients of their models.

Wong and Lilly [115] proposed two dynamic subgrid-scale closure methods for turbulent thermal convection: stratification and scaling formulations. In stratification formulation, [10, 102], it is assumed that the dissipation rate balances the SGS energy production rate that includes a buoyancy term. SGS viscosity and diffusivity are modified to account for buoyancy

effects explicitly:

$$\nu_{sgs} = C\bar{\Delta}^2 \left( \bar{S}^2 - \frac{1}{Pr_{sgs}} \frac{g}{\theta_0} \frac{\partial \bar{\theta}}{\partial z} \right)^{1/2}, \tag{2.124}$$

$$\kappa_{sgs} = \frac{C}{Pr_{sgs}} \bar{\Delta}^2 \left( \bar{S}^2 - \frac{1}{Pr_{sgs}} \frac{g}{\theta_0} \frac{\partial \bar{\theta}}{\partial z} \right)^{1/2}, \tag{2.125}$$

where $g$, $\theta_0$ and $z$ are the gravitational acceleration, reference temperature and vertical coordinate respectively. Buoyancy force is represent by the second term in parentheses in equations (2.124) and (2.125). Because of the buoyancy coupling, an iterative scheme is needed to solve the system of equations. However, it turned out that it is impossible to find a real converged solution and in practice the iterative scheme is terminated after ten iterations. In their work, Wong and Lilly [115] proposed a simplified model, scaling formulation, based on the Kolmogorov scaling, Kolmogorov [57]. SGS diffusivity is given as

$$\kappa_{sgs} = \frac{C^{2/3}}{Pr_{sgs}} \bar{\Delta}^{4/3} \epsilon^{1/3}, \tag{2.126}$$

where $\epsilon$ is the dissipation rate. This model excludes the assumption that the dissipation rate equals the SGS energy production rate. Dynamic procedure of Germano et al. [34] and Lilly [66] is utilized to determine model coefficient $C$ and $Pr_{sgs}$ and it is assumed that these do not depend on the filter width. Advantage of the model (2.126) over (2.125) is considerable reduction of computational effort, and in their study the ratio of the total computational times was 1.7. However, the model (2.126) does not account for buoyancy effects. Furthermore, spatial averaging was required to prevent the numerical instability. The two models were evaluated both *a priori*, by using a DNS database, and *a posteriori* by conducing a LES of turbulent Rayleigh-Benard convection. Interesting result from their simulation is the behavior of subgrid-scale turbulent Prandtl number. It is found out that the scaling formulation produces $Pr_{sgs}$ values that are smaller than the values suggested from the literature. For example, Deardorff [18, 19] reported that the spectrum for temperature became similar to the velocity spectra at high wavenumbers only after the SGS eddy diffusivity had been increased by a factor of three over SGS viscosity; in his work, Eidson [22] suggests a value of $0.4$; Schmidt and Schumann [97] have calculated from the coefficients of 'one dimensional' longitudinal velocity and temperature spectra that the value for $Pr_{sgs}$ should be around $0.42$. The values of $Pr_{sgs}$ evaluated from the DNS database with the scaling formulation were around $0.1$ in the bulk, but, near the walls the values turned negative. When computed from LES study, $Pr_{sgs}$ showed flat profile in the bulk with the values around $0.2$, and increased near the wall with the maximal values below $0.6$. On the other hand, $Pr_{sgs}$ values from the stratification formulation are higher than the values from literature. $Pr_{sgs}$ values according to the stratification formulation evaluated from DNS data were between $0.6$ and $1$ in the bulk of the channel and around $1.5$ close to the walls. For LES, study $Pr_{sgs}$ ranges between $0.4$ and $0.8$ in the bulk and increases sharply, up to $4$, near the walls. Since the stratification formulation includes buoyant effects explicitly, this may be the reason for higher subgrid-scale turbulent Prandtl numbers.

Peng and Davidson [84] investigated a turbulent natural convection flow in a confined cavity with two differentially heated side walls. This kind of flows is characterized by a large span of scales interacting with each other: the boundary layer, which forms along the enclosure surfaces, interacts with the wall shear and with the core region. Mainly due to the complexity of physics associated with this kind of flows, previous simulations performed by the same authors failed to give satisfactory good agreement with the experimental measurements. As a cause of a disagreement, Peng and Davidson [84] pointed to the inability of the SGS model "*... to capture the underlying physics of the energy backscatter phenomenon, which is regarded*

*as an essential ingredient in reproducing the transition regime in the boundary layer near the vertical heated/cooled wall*". Based on the previous work of Eidson [22], who included a buoyancy production term in the production of subgrid-scale kinetic energy, Peng and Davidson [84] proposed a modified model for SGS time scale and hence for the SGS viscosity. The original formulation of Eidson [22] is given by Eq. (2.117) and, as it can be seen, if the term in parentheses becomes negative, i.e. $|\bar{S}|^2 < 2\frac{Pr\,Ra}{Pr_{sgs}}\frac{\partial\bar{\theta}}{\partial x_3}$, then the equation for SGS viscosity has a non-real solution. If this occurs, the issue is usually treated by fixing the SGS viscosity to zero. Peng and Davidson [84] overcame the problem of non-real solutions by dividing the time scale used in the Eidson model by the magnitude of the resolved strain rate tensor, so that a new expression for time scale was proposed:

$$\mathcal{T} = \left(|\bar{S}| - \frac{g\beta}{Pr_{sgs}|S|}\frac{\partial\bar{\theta}}{\partial x_j}\delta_{2j}\right)^{-1}, \tag{2.127}$$

where $\delta_{2j}$ defines the coordinate in the direction of gravity. Afterwards, this time scale is used to calculate subgrid-scale viscosity, $\nu_{sgs} = C\Delta^2/\mathcal{T}$. Negative $\nu_{sgs}$ values are allowed in the range $[0, -\nu]$. Since the effective viscosity, $\nu_{eff} = \nu + \nu_{sgs}$, should not be negative, higher negative $\nu_{sgs}$ values need to be clipped in order to retain numerical stability. Model coefficient $C$ represents a square of the of the original Smagorinsky coefficient and it has been determined using the dynamic procedure. The authors have mentioned that the dynamic procedure can also be applied to calculate $Pr_{sgs}$, however, in the simulation they have used a fixed value, $Pr_{sgs} = 0.4$. The new model coupled with the dynamic procedure showed better behavior than the original Smagorinsky and Eidson models. However, a disadvantages is that a fixed value for $Pr_{sgs}$ is used. There is a possibility to calculate subgrid-scale turbulent Prandtl number dynamically, but this would lead to a system of non-linear equations which cannot be solved directly and it would be necessary to find the best among the multiple possible roots of the system, see Sagaut [94]. To solve the resulting system of non-linear equations, an iterative scheme would be needed, but this is associated with numerical problems, see e.g. Wong and Lilly [115].

You and Moin [116, 117] derived a dynamic global-coefficient subgrid-scale model where the model coefficients are globally uniform in space but vary in time. The model is based on the "global equilibrium" assumption between the subgrid-scale scalar diffusion and the molecular diffusion. Previously, based on the model proposed by Vreman [107], Park et al. [83] derived a subgrid-scale momentum flux model with global model coefficients and "global equilibrium" assumption. However, the model of Park et al. [83] required two test-filter levels which reduced the model applicability. The model of You and Moin [117] requires only one test filter and does not require any numerical stabilization procedure. The dynamic equation for the model coefficient $D_T$, which appears in the subgrid scale scalar flux, is obtained by extracting the test filtered transport equation for the scalar variance at the grid-filter level from the transport equation for scalar variance at test-filter level. The resulting transport equation is then volume-averaged over the entire computational domain and in addition it was assumed that the volume averages of the redistribution term and the time variation term are negligible. The dynamic equation for $Pr_{sgs}$ is given as follows:

$$Pr_{sgs} = \frac{\left\langle \nu_T^t \frac{\partial\hat{\bar{\theta}}}{\partial x_j}\frac{\partial\hat{\bar{\theta}}}{\partial x_j} - \widehat{\nu_T^g \frac{\partial\bar{\theta}}{\partial x_j}\frac{\partial\bar{\theta}}{\partial x_j}} \right\rangle}{\alpha\left\langle \widehat{\frac{\partial\bar{\theta}}{\partial x_j}\frac{\partial\bar{\theta}}{\partial x_j}} - \frac{\hat{\bar{\theta}}}{\partial x_j}\frac{\hat{\bar{\theta}}}{\partial x_j} \right\rangle}, \tag{2.128}$$

where $\nu_T^g$ and $\nu_T^t$ are SGS viscosities at grid and test filter levels and subgrid-scale scalar flux is $q_j = -\frac{\nu_T^g}{D_T}\frac{\partial\bar{\theta}}{\partial x_j}$. It should be noted that model coefficient $D_T$ corresponds to the subgrid-scale

turbulent Prandtl number. Equation (2.128) represents relation of the subgrid-scale scalar diffusivity to the molecular diffusivity. As a benchmark test, turbulent flow through a plane channel at two different friction Reynolds numbers of $Re_\tau = 180$ and $300$ and two different molecular Prandtl numbers of $1$ and $25$ is investigated. As expected, it is found out that model coefficient $D_T$ (or $Pr_{sgs}$) strongly depends on molecular diffusivity. The results show that for $Re_\tau = 150$ and high molecular Prandtl number, $Pr = 25$, the model coefficient was much larger than the value obtained for $Pr = 1$: $D_T \approx 11$ compared to $D_T \approx 1$.

### Temperature dependent $Pr_{sgs}$ (*Otic 2010*)

Otic [81] developed a method to estimate $Pr_{sgs}$ which accounts for the effect of molecular fluid properties on the energy transfer. The method is based on the one equation model for the velocity field and temperature and velocity spectra of the unresolved scales.

In a simplified model, one assumes a similarity of the velocity and temperature fields over all flow scales. However, this can be justified only for the flows of fluids whose molecular Prandtl number does not strongly differ from one, e.g. air. In other cases, difference between velocity and temperature field spectra, see Fig. 2.7, can be significant so that the molecular fluid properties have to be considered when choosing an appropriate value for $Pr_{sgs}$ in order to fulfill different requirements on SGS models. In order to improve modeling, Otic [81] ap-

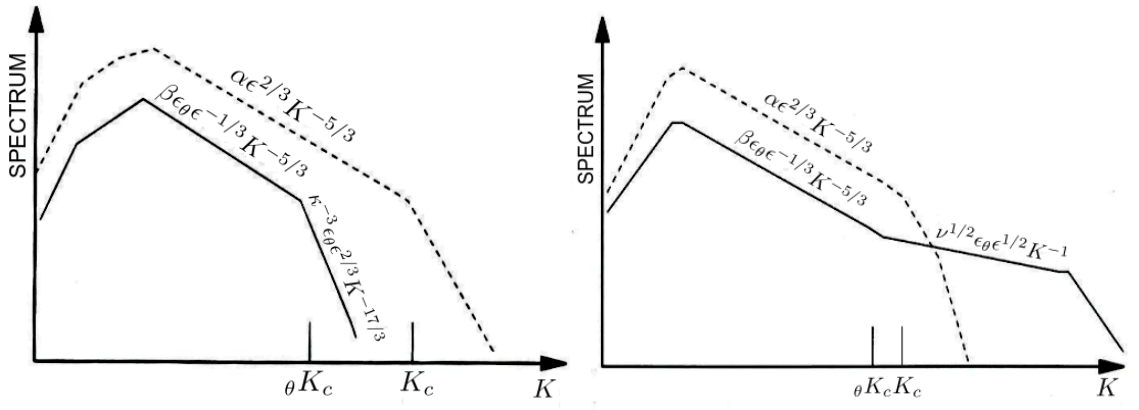


**(a)** $Pr << 1$ **(b)** $Pr >> 1$

**Fig. 2.7:** Schematic of the kinetic energy spectrum (dashed line) and the temperature variance spectrum (solid line). Adjusted from [94].

plied the idea of temperature and velocity parametrization as a geometric mean of both fields instead of assuming the similarity of the both fields. A short derivation of the model is given next.

The model is based on the simple gradient diffusion hypothesis for subgrid-scale heat flux, Eq. (2.113). If the one equation eddy viscosity model is applied to close the momentum equation, then subgird-scale viscosity $\nu_{sgs}$ and corresponding subgrid-scale diffusivity, $\kappa_{sgs}$ can be written in the following form:

$$\nu_{sgs} = c'_\nu \tau k, \tag{2.129}$$

$$\kappa_{sgs} = c'_\kappa \tau k, , \tag{2.130}$$

where $\tau$ is a time-scale and $\Delta$ is the characteristic length. Equation (2.114) can be easily derived form Eq. (2.130) if the mechanical time-scale $\tau = k/\epsilon$ is used in combination with the Rotta's model, Eq. (2.132), for dissipation of turbulent kinetic energy, $\epsilon$.

Instead of using the mechanical time-scale, a concept of mixed time-scale is applied:

$$\tau = \sqrt{\frac{k}{\epsilon}\frac{\overline{\theta'^2}}{\epsilon_\theta}}, \tag{2.131}$$

where $\overline{\theta'^2}$ and $\epsilon_\theta$ are SGS temperature variance and its dissipation rate. Turbulent kinetic energy dissipation rate is approximated by the Rotta's model

$$\epsilon = c_\epsilon \frac{k^{3/2}}{\Delta}. \tag{2.132}$$

Further on, author have derived an averaged approximation of Eq. (2.131) and this will be briefly shown in the following equations. For details about the derivation of the model, see [81].

In the inertial-convective subrange of isotropic turbulence, the spectra of kinetic energy and temperature variance integrated over all wave numbers $K$ give

$$E(K) = \alpha \langle\epsilon\rangle^{2/3} K^{-5/3}, \tag{2.133}$$

$$E_\theta(K) = \beta \langle\epsilon_\theta\rangle \langle\epsilon\rangle^{-1/3} K^{-5/3}, \tag{2.134}$$

where $\langle\rangle$ represents the ensemble average of a quantity. The coefficients $\alpha$ and $\beta$ of the three-dimensional are approximated as:

$$\alpha \sim 1.6, \quad \beta \sim 1.3. \tag{2.135}$$

From the equations (2.133) and (2.134), the subgrid-scale kinetic energy and temperature variance are:

$$\langle k\rangle = \int_{K_c}^{\infty} E(K)dK = \frac{3}{2}\alpha\langle\epsilon\rangle^{2/3}\left(\frac{1}{K_c}\right)^{2/3}, \tag{2.136}$$

$$\langle\overline{\theta'^2}\rangle = \int_{{}_\theta K_c}^{\infty} E_\theta(K)dK = \frac{3}{2}\beta\langle\epsilon_\theta\rangle\langle\epsilon\rangle^{-1/3}\left(\frac{1}{{}_\theta K_c}\right)^{2/3}, \tag{2.137}$$

where $K_c$ and ${}_\theta K_c$ are the effective cutoff wave numbers of the kinetic energy spectrum and temperature variance spectrum respectively. According to Corrsin [13], the ratio of the cutoff wave numbers can be estimated as:

$$\frac{{}_\theta K_c}{K_c} = Pr^{3/4}. \tag{2.138}$$

Finally, from (2.136), (2.137), (2.138) and (2.132) follows

$$\sqrt{\frac{k}{\epsilon}\frac{\overline{\theta'^2}}{\epsilon_\theta}} = \frac{1}{c_\epsilon}\left(\frac{\beta}{\alpha}\right)^{1/2} Pr^{4/9}\Delta\langle k\rangle^{-1/2}. \tag{2.139}$$

Furthermore, since $k$ and hence $\langle k\rangle$ are locally defined positive quantities, there exists a locally defined positive coefficient $c_\kappa'$ such that $c_\kappa' k^{-1/2} = \langle k\rangle^{-1/2}$. This statement is used in (2.139) and together with (2.130) yields

$$\kappa_{sgs} = c_\kappa\left(\frac{\beta}{\alpha}\right)^{1/2} Pr^{4/9}\Delta k^{1/2}, \tag{2.140}$$

where $\alpha$ and $\beta$ are given in (2.135) and $Pr$ is molecular Prandtl number. The model (2.140) is further simplified by using the results from Schmidt and Schumann [97]

$$c_\kappa = (2\alpha/\beta)c_\nu, \tag{2.141}$$

which yields:

$$\kappa_{sgs} = c_\nu \left(\frac{4\alpha}{\beta}\right)^{1/2} Pr^{4/9} \Delta k^{1/2}. \tag{2.142}$$

From the above equation, $Pr_{sgs}$ is calculated as follows

$$Pr_{sgs} = \frac{\nu_{sgs}}{\kappa_{sgs}} = \left(\left(\frac{4\alpha}{\beta}\right)^{1/2} Pr^{4/9}\right)^{-1}. \tag{2.143}$$

Subgrid-scale turbulent Prandtl number calculated on this way depends on the molecular fluid properties. Therefore, this model should bring improvements when simulating turbulent flows with strong temperature variations. In addition, it can be used to estimate $Pr_{sgs}$ for different fluids.

### 2.5.2 Tensor subgrid-scale diffusivity

The concept of scalar subgrid-scale diffusivity is usually sufficient for homogeneous flows, where both velocity and temperature (scalar) fields are isotropic. However, for more complex flow configurations, which are likely to appear in real engineering problems, velocity and/or temperature fields are anisotropic. For these types of flows, modeling can be improved by applying a concept of tensor (anisotropic) SGS viscosity/diffusivity. In this case, subgrid-scale heat flux is determined from the following equation

$$q_j = -\kappa_{sgs_{ij}} \frac{\partial \bar{\theta}}{\partial x_j}, \tag{2.144}$$

where $\kappa_{sgs_{ij}}$ is tensor SGS diffusivity. The concept of tensor eddy diffusivity was originally proposed by Batchelor [8] for RANS modeling.

Pullin [92] developed an anisotropic subgrid-scale diffusivity model for SGS flux of a passive scalar. The model is based on an analytical solution for convection of passive scalar field by the axisymmetric model of a subgrid vortex. In addition, it was assumed that the effects of scalar diffusivity are negligible small compared to convection within the vortex. Pullin [92] argued that this is a physically reasonable assumption if the order of magnitude of molecular diffusivity is not larger than the order of magnitude of molecular viscosity, i.e. if molecular Schmidt (or Prandtl) number is $Sc = \mathcal{O}(1)$. The equation for SGS diffusivity reads as follows

$$\kappa_{sgs_{pj}} = \frac{\gamma \pi}{2 k_c} K^{1/2} \left(\delta_{jp} - e_j^v \, e_p^v\right), \tag{2.145}$$

where $K$ is subgrid energy, $\gamma$ is a dimensionless constant (the author used $\gamma = 1$ for the calculations), $e_j^v$ and $e_p^v$ are the direction cosines of the vortex axis and $k_c$ is cutoff wave number. The model requires input of one coefficient, $\gamma$. Recently, Mattner [71] applied this model for LES of turbulent mixing layers.

Peng and Davidson [85] investigated Rayleigh-Benard convection in an infinite vertical channel (infinite cavity). Characteristic of this flow types is that the mean temperature gradient vanishes in the streamwise direction, which means that the conventional SGS models, which are based on the linear subgrid-scale diffusivity assumption, will give a zero SGS heat flux in this direction. This is, however, contrary to the experimental investigations which showed that the resolved turbulent heat flux component in this direction is considerably larger than in the wall-normal direction. In order to improve modeling of subgrid-scale heat flux, particularly for Rayleigh -Benard convection problem, Peng and Davidson [85] developed a dynamic non-linear SGS heat flux model where the SGS viscosity is represented by a tensor. The idea of

Peng and Davidson [85] was to represent the SGS heat flux by a term which is proportional to the production term of the SGS heat flux transport equation. This production term includes shear production and buoyancy production. Moreover, the buoyancy production includes the subgrid-scale scalar variance, which is not known and therefore requires additional equation. The authors have concluded that such kind of modeling would result in a very complicated implicit algebraic formulation for SGS heat flux vector since the model invokes more than one coefficient that has to be determined. Hence, the authors have simplified the equation for SGS heat flux by excluding the production terms due to the buoyancy and large scale velocity gradient. The only production term which is left, the production due to the large scale temperature gradient, is modified by considering only the deviatoric part of the SGS stress tensor. SGS time scale is defined in terms of filter size and SGS viscosity. Finally, the following model for SGS heat flux is proposed:

$$q_i = C_t \bar{\Delta}^2 \bar{S}_{ij} \frac{\partial \bar{\theta}}{\partial x_j}, \tag{2.146}$$

where $C_t$ is a model coefficient which can be determined dynamically:

$$C_t = \frac{P_j Q_j}{Q_j Q_j}, \tag{2.147}$$

where

$$Q_j = \hat{\Delta}^2 \hat{\bar{S}}_{jk} \frac{\partial \hat{\bar{\theta}}}{\partial x_k} - \widehat{\Delta^2 \bar{S}_{jk} \frac{\partial \bar{\theta}}{\partial x_k}}, \tag{2.148}$$

and $P_j$ is given in Eq. (2.71). The proposed model provides non-zero SGS heat flux in the streamwise direction even in the case of zero temperature gradient.

The model is tested *a posteriori* for a buoyant flow in an infinite vertical channel with differentially heated side walls and the results are compared with those obtained by using a scalar SGS diffusivity model. Two models produced almost identical results for the mean velocity and temperature as well as for their fluctuations. The only significant difference was in the streamwise component of velocity fluctuations and SGS heat flux where the proposed model gave better prediction. Since the Smagorinsky model was used in both cases, the analysis showed that the modeling of SGS heat flux also affects the large scale velocity field. A disadvantage of the model is that, even if it is proposed for buoyancy driven flows, the production term due to the buoyancy is excluded.

The tensor SGS thermal diffusivity in the model of Peng and Davidson [85] is a linear homogeneous function of the resolved strain rate tensor and large scale temperature gradient. By applying a theory of tensor invariants and tensor functions, Wang et al. [109] developed a new model, where the SGS heat-flux is described as a vector function of a strain rate tensor, $\bar{S}_{ij}$, rotation rate tensor, $\bar{\Omega}_{ij}$ and gradient of large scale temperature field, $\partial\bar{\theta}/\partial x_j$. According to Wang et al. [109], SGS heat flux can be generally expressed as

$$\begin{aligned} q_j = {} & \phi_0 \frac{\partial \bar{\theta}}{\partial x_j} + \phi_{11} \bar{S}_{jk} \frac{\partial \bar{\theta}}{\partial x_k} + \phi_{12} \bar{\Omega}_{jk} \frac{\partial \bar{\theta}}{\partial x_k} + \phi_{21} \bar{S}_{jn} \bar{S}_{nk} \frac{\partial \bar{\theta}}{\partial x_k} \\ & + \phi_{22} \bar{\Omega}_{jn} \bar{\Omega}_{nk} \frac{\partial \bar{\theta}}{\partial x_k} + \phi_{23} \left( \bar{S}_{jn} \bar{\Omega}_{nk} - \bar{\Omega}_{jn} \bar{S}_{nk} \right) \frac{\partial \bar{\theta}}{\partial x_k}, \end{aligned} \tag{2.149}$$

where $\phi_{ii}$ are model coefficients which can be constructed from large fields. Terms on the right-hand side represent zeroth, first and second order terms. However, Wang et al. [109] stated that it is inefficient to solve Eq. (2.149) because there are six independent terms and six model coefficients that have to be calculated. Hence, the authors simplified Eq. (2.149) by

excluding the second order terms, which reduced the nonlinear equation to the linear one. As a result, an expression for SGS is diffusivity is proposed

$$\kappa_{sgs_{jk}} = f\left(\bar{S}_{jk}, \bar{\Omega}_{jk}\right) = C_{\theta E}\bar{\Delta}^2|\bar{A}|\delta_{jk} + C_{\theta S}\bar{\Delta}^2\bar{S}_{jk} + C_{\theta W}\bar{\Delta}^2\bar{\Omega}_{jk}, \tag{2.150}$$

where $\bar{A}_{ij}$ represents large scale velocity gradient, $\bar{A}_{ij} \equiv \partial\bar{u}_i/\partial x_j$, and $C_{\theta E}$, $C_{\theta S}$, $C_{\theta W}$ are model coefficients which can be calculated dynamically. Furthermore, the authors showed that some of the linear SGS diffusivity models and mixed models for SGS heat flux can be derived from the model proposed here. The model was tested for the case of mixed convection in an infinite vertical channel at friction Reynolds number of $Re_\tau = 150$ and Grashof number $Gr = 9.6\times10^5$ and it is compared with the standard dynamic scalar SGS diffusivity model. The comparison showed that both models produce similar results for the mean large-scale velocity and temperature fields as well as for for the velocity and temperature fluctuations. The distinct difference between two modeling approaches exists only at the SGS scales. Again, same as the model proposed by Peng and Davidson [85], the model proposed by Wang et al. [109] also does not include buoyancy effects. Because of the rotation rate tensor, which is directly included in the SGS diffusivity, the model might be suitable for rotational flows.

Further variations of the model (2.150) are proposed by Wang et al. [110] in the same year. The first of the proposed models, called *dynamic full linear tensor diffusivity model*, is basically the same as Eq. (2.150) with the difference that the rotational term is excluded. In the second model, *complete and irreducible dynamic nonlinear tensor diffusivity*, the Noll's formula is applied to construct subgrid-scale heat flux as a vector-valued function of strain rate tensor, large-scale temperature gradient and square of the strain rate tensor. This formulation yields a quadratic nonlinear tensor SGS diffusivity:

$$\kappa_{sgs_{jk}} = C_{\theta E}\bar{\Delta}^2|\bar{S}|\delta_{jk} + C_{\theta S}\bar{\Delta}^2\bar{S}_{jk} + C_{\theta N}\bar{\Delta}^2\frac{\bar{S}_{ji}\,\bar{S}_{jk}}{|S|}. \tag{2.151}$$

Model coefficients $C_{\theta E}$, $C_{\theta S}$ and $C_{\theta N}$ are calculated dynamically.

More general class of models for SGS tensor diffusivity can be constructed by considering the SGS stress tensor instead of resolved strain rate tensor. Wang et al. [111] proposed three new models for SGS tensor diffusivity based on the SGS stress tensor: homogeneous linear, full linear and quadratic SGS tensor diffusivity model. The homogeneous linear model represents the extension of the original relation of Daly and Harlow [15] for modeling the turbulent heat flux in RANS. Within the frame of LES, SGS tensor diffusivity is modeled as

$$\kappa_{sgs_{jk}} = C_{\theta G}\mathcal{T}\tau^*_{jk}, \tag{2.152}$$

in which $\mathcal{T}$ represents time scale, $C_{\theta G}$ is model coefficient and $\tau^*_{jk}$ is deviatoric part of SGS stress tensor. Model coefficient is obtained from the dynamic procedure. Instantaneous value of SGS tensor diffusivity calculated from Eq. (2.152) can locally become negative which is considered by the authors as a backscatter of scalar energy from the subgrid to large scales.

The second proposed model by Wang et al. [111] is a full linear SGS tensor diffusivity model. It represents some kind of combination between simple SGS scalar diffusivity (which is a function of SGS stress tensor of the zeroth order) and the homogeneous linear model (which is a function of SGS stress tensor of the first order), Eq. (2.152). The expression for $\kappa_{sgs_{jk}}$ is same as Eq. (2.151) except that SGS stress tensor $\tau_{ij}$ is used instead of the large scale strain rate tensor, $\bar{S}_{jk}$, and last term on the RHS is not considered.

The most general model proposed in [111] is a quadratic SGS tensor diffusivity model. As well as the model (2.151), the quadratic model for $\kappa_{sgs_{jk}}$ is derived from Noll's formula in which the SGS stress tensor is used. If the original Smagorinsky model is used for $\tau_{ij}$ and

SGS time scale is evaluated as $\mathcal{T} = 1/|\bar{S}|$, then the quadratic nonlinear model, Eq. (2.151), can be recast from the quadratic model proposed here. Moreover, it is also shown that the model of Peng and Davidson [85] can be derived from this model. Validation of the models has been performed using two test cases of fully developed turbulent channel flow where the temperature behaves both as a passive and an active scalar.

Recently, Rasam et al. [93] proposed an explicit algebraic model for subgrid-scale scalar flux. The model represents an extension of the previous work of Marstorp et al. [69], who developed an explicit subgrid-scale stress model which involves the strain rate and rotation rate tensors. The model proposed by Rasam et al. [93] includes resolved strain rate and rotation rate tensors, resolved scalar gradient vector and subgrid-scale stress tensor. The resulting expression for SGS heat flux is an algebraic equation. Since it combines the resolved and subgrid strain rate tensors and temperature gradient, the model is not necessarily aligned with the resolved temperature gradient. Because of the rotation rate tensor, the model is suitable for rotating flows. Tensor SGS diffusivity is calculated from the following equation:

$$A_{ij}^{-1} = \frac{\left(c_{1\theta}^2 - \frac{1}{2}Q_1\right) I_{ij} - c_{1\theta}\left(c_s \bar{S}_{ij}^* + c_\Omega \bar{\Omega}_{ij}^*\right) + \left(c_s \bar{S}_{ij}^* + c_\Omega \bar{\Omega}_{ij}\right)^2}{c_{1\theta}\left(c_{1\theta}^2 - \frac{1}{2}Q_1\right) + \frac{1}{2}Q_2},$$

$$\kappa_{sgs_{ij}} = -1\left(1 - c_{4\theta}\right)\mathcal{T} A_{ij}^{-1} \tau_{jk} \frac{\partial \bar{\theta}}{\partial x_k}, \tag{2.153}$$

where $Q_1 = c_s^2 tr(\bar{S}_{ij}^{*2}) + c_\Omega^2 tr(\bar{\Omega}_{ij}^{*2})$ and $Q_2 = \frac{2}{3}c_s^3 tr(\bar{S}_{ij}^{*3}) + 2c_s c_\Omega^2 tr(\bar{S}_{ij}^* \bar{\Omega}_{ij}^{*2})$, $\mathcal{T}$ is a time scale and $\bar{S}_{ij}^*$ and $\bar{\Omega}_{ij}^*$ are resolved strain and rotation rate tensors multiplied by a time scale. Model coefficients $c_i$ are calculated dynamically. The model is validated for the scalar transport in a channel flow without rotation and with wall-normal rotation at friction Reynolds numbers $Re_\tau = 180$ and $590$, and it was found to perform better than standard dynamic SGS diffusivity model.

### 2.5.3 Mixed models

Mixed models combine standard linear scalar diffusivity models with some other model, usually scale similarity or nonlinear (tensor SGS diffusivity) models.

Following the idea of Bardina et al. [7], Salvetti and Banerjee [96] proposed a mixed dynamic model for subgrid-scale heat flux which combines standard gradient diffusion and the scale similarity models. As a result, the following expression for SGS heat flux is proposed:

$$q_k = -\frac{\bar{\rho}\nu_t}{Pr_{sgs}} \frac{\partial \bar{\theta}}{\partial x_k} + h q_k^L, \tag{2.154}$$

where $q_k^L$ represents the resolved part of the SGS heat flux:

$$q_k^L = \bar{\rho}(\widehat{\bar{u}_k \bar{\theta}} - \hat{\bar{u}}_k \hat{\bar{\theta}}), \tag{2.155}$$

which can be directly calculated.

As well as SGS Prandtl number, the model coefficient $h$ is also determined dynamically. The model was tested only *a priori* using DNS data for fully developed turbulent incompressible and compressible flows. Further tests, both *a priori* and *a posteriori* are given in Jiménez et al. [48].

A mixed model, based on the idea of Bardina et al. [6, 7], which combines scalar and tensor SGS diffusivity models is investigated in Porte-Agel et al. [89, 90]. The model has

favorable features of both models: it is dissipative enough due to the scalar SGS diffusivity part, and the due to the nonlinear part, the model is able to account for backscatter of energy which can be of high importance. SGS heat flux is calculated as follows

$$q_i = -\left[Pr_{sgs}^{-1} C_s^2\right]^* \Delta^2 |S| \frac{\partial \theta}{\partial x_i} + [C_{nl}]^* \Delta^2 \frac{\partial \bar{u}_i}{\partial x_k} \frac{\partial \theta}{\partial x_k}, \tag{2.156}$$

in which $\left[Pr_{sgs}^{-1} C_s^2\right]^*$ and $[C_{nl}]^*$ are model coefficients which can be calculated dynamically. The model is suitable for atmospheric surface layer research where the traditional scale SGS diffusivity models fail to predict SGS flux and dissipation of temperature variance mainly due to their fully dissipative nature and inability to provide backscatter (whose existence is confirmed by experimental measurements).

### 2.5.4 Conclusions

Literature review revealed that most of the modeling in LES are focused on the forced convection. Only a small number of proposed models include buoyancy effects, but all of them are actually based on the model of Eidson [22], where the buoyancy effects are included in the production term of the subgrid-scale kinetic energy, which is assumed to be balanced by the dissipation rate of $k$. The Eidson's model is improved by introducing the dynamic procedure to calculate the Smagorinsky coefficient and SGS turbulent Prandtl number ($C = 0.21$ and $Pr_{sgs} = 0.4$ are used in [22]). However, application of dynamic procedure to calculate model coefficients resulted in numerical instabilities, Wong and Lilly [115]. Moreover, the inclusion of buoyancy effects only in the production term of turbulent kinetic energy may be insufficient.

To the authors knowledge, all models in the known literature that are using some kind of anisotropic SGS diffusivity are constructed without considering the buoyancy force. In the work of Peng and Davidson [85] buoyancy production term was excluded since, according to the authors, it would result in a complicated system of equations. Other external forces, like system rotation, are included in the works of Wang et al. [109] and Rasam et al. [93].

In the mixed model of Salvetti and Banerjee [96] one part of the SGS heat flux is assumed to be proportional to the resolved heat flux vector. Model of Porte-Agel et al. [89, 90] represents combination of scalar and tensor SGS diffusivity. However, in both models buoyancy production term is not considered.

An alternative approach to model subgrid-scale heat flux is to provide an expression which includes also the buoyancy production term. In this case, SGS heat flux is represented by an algebraic relation, which is a common modeling approach in RANS. The model constructed on this way contains more unknown coefficients: one for each of the terms appearing in the algebraic relation. In this work, algebraic model for SGS heat flux contains a term based on the SGD hypothesis and the buoyancy production term. Therefore, the model requires two coefficients and the dynamic procedure will be used in order to calculate these. Depending on the constraints imposed on model coefficients, two versions of the model are possible: volume averaged and locally dependent. In the volume averaged case, it will be assumed that each of the model coefficients has one unique value for whole computational domain. This approach is suitable for homogeneous flows, or if fluid temperature variations are small. In locally dependent version, model coefficients can vary also in space. However, this approach requires a more complicated mathematical procedure.

Derivations of the dynamic model for $Pr_{sgs}$ based on the one equation model for velocity field, and the new model for subgrid-scale heat flux are given in the next chapter.

## 2.6 Numerical Methods

Fundamentals of the numerical methods used in the present work are given in this section. A detailed introduction on the topic is given in i.e. [17, 25, 46].

### 2.6.1 Finite volume discretization

In the Finite Volume Method (FVM), the solution domain is divided into a finite number of control volumes, or shortly cells. Variable values are to be calculated at the center of each cell, while the values at cell faces are obtained by interpolation. Control volumes can be of any shape (polyhedral cells), so that FVM is suitable for complex geometries.

The finite volume method is based on the integral form of conservative equation. Conservation equation for a generic quantity $\phi$ is

$$\underbrace{\frac{\partial}{\partial t}\int_{\Omega}\rho\phi d\Omega}_{\text{Time derivative}}+\underbrace{\int_{S}\rho\phi\vec{u}\cdot\vec{n}dS}_{\text{Convective term}}=\underbrace{\int_{S}\Gamma\nabla\phi\cdot\vec{n}dS}_{\text{Diffusive term}}+\underbrace{\int_{\Omega}S_{\phi}(\phi)d\Omega}_{\text{Source term}}. \tag{2.157}$$

Here, $\phi$ is any conserved intensive property, $\Omega$ is a volume occupied by a computational cell and $S$ represents its surface, $\vec{n}$ is the surface normal vector and $\vec{u}$ is the fluid velocity. Equation (2.157) applies to each computational cell. Surface integrals in Eq. (2.157) can be converted into volume integral by using the Gauss's divergence theorem

$$\int_{S}\phi\vec{n}dS=\int_{\Omega}\nabla\phi d\Omega, \tag{2.158}$$

which yields

$$\frac{\partial}{\partial t}\int_{V_P}\rho\phi dV+\int_{V_P}\nabla\cdot(\rho\phi\vec{u})dV=\int_{V_P}\nabla\cdot(\Gamma\nabla\phi)dV+\int_{V_P}S_{\phi}(\phi)dV. \tag{2.159}$$

Note that the Eq. (2.159) is now written for an arbitrary control volume, $V_P$.

Because the diffusion term includes the second derivative of $\phi$ with respect to spatial coordinate, the Eq. (2.159) is of the second order. Hence, the discretization scheme has to be of at least second order both in space and time.

Let us consider the Taylor series expansion about $P$

$$\phi(x_i)=\phi_P+(x_i-x_{iP})\left(\frac{\partial\phi}{\partial x_i}\right)_P+\frac{(x_i-x_{iP})^2}{2}\left(\frac{\partial^2\phi}{\partial x_i^2}\right)_P+H, \tag{2.160}$$

where $H$ represents the higher order terms. To achieve that discretization scheme is of the second order we assume that variable $\phi$ varies linearly around the point $P$

$$\phi(x_i)=\phi_P+(x_i-x_{iP})(\nabla\phi)_P, \tag{2.161}$$

and in time

$$\phi(t)=\phi_t+\Delta t\left(\frac{\partial\phi}{\partial t}\right)_t. \tag{2.162}$$

A numerical solution requires that a series of volume and surface integrals need to be calculated for each control volume. A volume integral can be simply approximated by the

product of the mean value of the integrand (value at the cell center) and cell volume, which yields

$$\int_{V_P} \phi dV = \phi_P V_P, \tag{2.163}$$

where $\phi_P$ is a value at the cell center and $V_P$ is the cell volume. Calculation of surface integrals is a little bit more complex. Integral over the entire cell boundary is equal to the sum of integrals over the cell faces

$$\int_S \phi dS = \sum_k \int_{S_k} \phi dS, \tag{2.164}$$

where $S_k$ is $k$-th surface and index $k$ loops over the each cell surface (four in 2D case, six in 3D, ...). However, in order to evaluate the integral (2.164), a value of $\phi$ on the cell surface $S_k$ is required. Unfortunately, only the values $\phi_P$ (at the cell center) are known, so that the values at cell surfaces have to be approximated. The easiest way to approximate the values at the cell surfaces is to use the midpoint rule. That is, the integral is approximated as a product of the integrand at the cell-face center and cell-face area

$$\int_{S_k} \phi dS \approx \phi_k S_k, \tag{2.165}$$

where $\phi_k$ is value of the variable $\phi$ at the center of $k$-th cell surface and $S_k$ is its area. However, value of the integrand at the cell-face center $\phi_k$ is not known, so that it has to be approximated by interpolation.

#### Approximation of cell-face values

Some of the interpolation schemes that are commonly used in CFD are: upwind, linear and quadratic upwind interpolations.

In ***Upwind Interpolation (UDS)***, a value at the cell-face center is assumed to be equal to the value at the cell center upstream form the face, depending on the flow direction. This can be written as

$$\phi_e = \begin{cases} \phi_P & if \quad (\vec{u} \cdot \vec{n})_e > 0 \\ \phi_E & if \quad (\vec{u} \cdot \vec{n})_e < 0 \end{cases}. \tag{2.166}$$

Here $\phi_P$ and $\phi_E$ are values at cell centers upstream from the face $e$. Only the first term on the right-hand side of Eq. (2.160) is retained, which means that this interpolation scheme is of the first order. Leading truncation error implicitly introduces numerical diffusion into the system, which significantly violates the accuracy (particularly in LES).

Another simple interpolation scheme is ***Linear Interpolation (CDS)***. Here, value at the cell-face center $e$ is linearly interpolated from the values at the neighboring cell centers, $P$ and $E$. Expression for $\phi_e$ reads as follows

$$\phi_e = \phi_E \lambda_e + \phi_P (1 - \lambda_e), \tag{2.167}$$

where $\lambda_e$ is the linear interpolation factor, defines as

$$\lambda_e = \frac{x_{ie} - x_{iP}}{x_{iE} - x_{iP}}, \tag{2.168}$$

where $x_i$ are nodal coordinates. This is the second order interpolation scheme.

The value at cell-face center $e$ can be evaluated more accurately by introducing the value at one more cell center. The additional cell is taken to be on the upstream side from the face

$e$. This interpolation scheme is known as ***Quadratic Upwind Interpolation (QUICK)***. Value at the face center $\phi_e$ is calculated as follows

$$\phi_e = \phi_U + g_1(\phi_D - \phi_U) + g_2(\phi_U - \phi_{UU}). \tag{2.169}$$

Coefficients $g_1$ and $g_2$ depend on the nodal locations

$$g_1 = \frac{(x_e - x_U)(x_e - x_{UU})}{(x_D - x_U)(x_D - x_{UU})}, \tag{2.170}$$

$$g_2 = \frac{(x_e - x_U)(x_D - x_e)}{(x_U - x_{UU})(x_D - x_{UU})}. \tag{2.171}$$

Subscripts $D$, $U$ and $UU$ stand for the downstream, the first upstream and the second upstream. This interpolation scheme is of the third order.

#### Approximation of convection term

Convective term from Eq. (2.159) can be discretized applying the equations (2.158), (2.164) and (2.165), which yields

$$\int_{V_P} \nabla \cdot (\rho\phi\vec{u})dV = \sum_k (\vec{S}_k \cdot \vec{u})_k (\rho\phi)_k = \sum_k F(\rho\phi)_k, \tag{2.172}$$

in which $\vec{S}_k$ is surface-area vector ($\vec{n}S$) of the $k$-th cell face and $F$ is the volume flux through the face $k$.

#### Approximation of diffusion term

Diffusion term can be discretized on the similar way as convection term. First is the Gauss's theorem (2.158) applied to convert volume integral to surface integral. Surface integral over the control volume is then evaluated as a sum of the surface integrals over the cell faces, Eq. (2.164). Finally, Eq. (2.165) is used to evaluate each of the integrals over the cell faces.

$$\int_{V_P} \nabla \cdot (\Gamma\nabla\phi)dV = \sum_k \vec{S} \cdot (\Gamma\nabla\phi)_k. \tag{2.173}$$

#### Approximation of source term

Source term needs to be linearized before discretization:

$$S_\phi(\phi) = S_u + S_p\phi. \tag{2.174}$$

Afterwards, Eq. (2.163) is applied to evaluated volume integral, which eventually yields

$$\int_{V_P} S_\phi(\phi)dV = S_{uP}V_P + S_{pP}V_P\phi_P. \tag{2.175}$$

### 2.6.2 Time integration

Integration over the control volume produces solution only at the one instant in time. However, in unsteady problems, integration has to be performed also in time. Time integration of Eq. (2.159) is given as

$$\int_t^{t+\Delta t}\left[\frac{\partial}{\partial t}\int_{V_P}\rho\phi dV+\int_{V_P}\nabla\cdot(\rho\phi\vec{u})dV-\int_{V_P}\nabla\cdot(\Gamma\nabla\phi)dV\right]dt = \int_t^{t+\Delta t}\left[\int_{V_P}S_\phi(\phi)dV\right]dt. \tag{2.176}$$

Convection, diffusion and source terms are replaced with the expressions (2.172), (2.173) and (2.175) to obtain

$$\int_t^{t+\Delta t}\left[\left(\frac{\partial\rho\phi}{\partial t}\right)_P V_P+\sum_k F(\rho\phi)_k-\sum_k\vec{S}\cdot(\Gamma\nabla\phi)_k\right]dt = \int_t^{t+\Delta t}\left(S_{uP}V_P+S_{pP}V_P\phi_P\right)dt. \tag{2.177}$$

#### Crank-Nicholson Method

This method is based on the trapezoidal rule for approximating the definite integrals. It requires evaluation of terms at two different time levels. The time derivative and time integral can be calculated as follows

$$\left(\frac{\partial\rho\phi}{\partial t}\right)_P=\frac{\rho_P^n\phi_P^n-\rho_P^{n-1}\phi_P^{n-1}}{\Delta t}, \tag{2.178}$$

$$\int_t^{t+\Delta t}\phi(t)dt=\frac{\phi^{n-1}+\phi^n}{2}\Delta t, \tag{2.179}$$

where $n-1$ and $n$ represent the first old and the new time steps respectively. Because the value of $\phi$ at the new time step is not known, the scheme is implicit and a system of algebraic equations needs to be solved within a time step in order to calculate a new value. Now, expressions (2.178) and (2.179) are used in (2.177) to obtained the following discretized form of the equation:

$$\begin{aligned}\frac{\rho_P\phi_P^n-\rho_P\phi_P^{n-1}}{\Delta t}V_P&+\frac{1}{2}\sum_k F(\rho\phi^n)_k-\frac{1}{2}\sum_k\vec{S}\cdot(\Gamma\nabla\phi^n)_k\\&+\frac{1}{2}\sum_k F(\rho\phi^{n-1})_k-\frac{1}{2}\sum_k\vec{S}\cdot(\Gamma\nabla\phi^{n-1})_k\\&=S_uV_P+\frac{1}{2}S_pV_P\phi_P^n+\frac{1}{2}S_pV_P\phi_P^{n-1}.\end{aligned} \tag{2.180}$$

In the above equation it is assumed that density and diffusivity do not change in time. Crank-Nicholson method is the second order accurate in time.

#### Backward Differencing

In addition to the first old and the new time levels which are required for the Crank-Nicholson method, Backward Differencing scheme includes also the second old time level. This method

is also the second order accurate in time. The time derivative at the new time level is calculated as

$$\left(\frac{\partial \phi}{\partial t}\right)^n = \frac{\frac{3}{2}\phi^n - 2\phi^{n-1} + \frac{1}{2}\phi^{n-2}}{\Delta t}, \tag{2.181}$$

where $n-2$ represents the second old time step ($\phi^{n-2} = \phi(t - \Delta t)$). Discretized form of the transport equation (2.177) takes the following form

$$\frac{\frac{3}{2}\rho_P\phi^n - 2\rho_P\phi^{n-1} + \frac{1}{2}\rho_P\phi^{n-2}}{\Delta t} V_P + \sum_k F(\rho\phi^n)_k - \sum_k \vec{S}\cdot(\Gamma\nabla\phi^n)_k = S_u V_P + \frac{1}{2} S_p V_P \phi_P^n. \tag{2.182}$$

Backward Differencing method is cheaper and easier to implement than the Crank-Nicholson method, however, it can produce high numerical diffusion which is an issue in LES (see [17]).

# Chapter 3

# Subgrid-scale heat flux modeling

In this chapter, new model for subgrid-scale heat flux which includes buoyancy production term is proposed. Derivation of the model is given in Sect. 3.2. In subsections 3.2.2, 3.2.3 and 3.2.4, dynamic procedure is applied to calculate model coefficients. In order to assess applicability of the dynamic procedure, dynamic model for $Pr_{sgs}$ based on the one equation model for velocity field is also derived. This is given in Sect. 3.1.

## 3.1 Dynamic $Pr_{sgs}$

Dynamic procedure is well known technique in LES which is very often used to determine unknown model coefficients. The model for SGS heat flux which is proposed in this work combines two terms: one which corresponds to the gradient diffusion hypothesis, and one which includes buoyancy effects. Therefore, the new model contains two coefficients which have to be determined, and for that purpose the dynamic procedure will be used. Before applying the dynamic procedure on the new model, it is applied to derive a dynamic model for $Pr_{sgs}$. The purpose of this is to test the behavior and stability of the dynamic modeling. First dynamic models for $Pr_{sgs}$ have been proposed by Moin et al. [75] and followed by Lilly [66], and these models were based on the Smagorinsky model for velocity field. In this work, dynamic model for $Pr_{sgs}$ is derived based on the one equation model.

To derive the model for $Pr_{sgs}$, let us start from the filtered energy equation, Eq. (2.64), which is, for the sake of completeness, given here again:

$$\frac{\partial(\tilde{\rho}C_p\bar{\theta})}{\partial t} + \frac{\partial(\tilde{\rho}C_p\bar{u}_j\bar{\theta})}{\partial x_j} = \kappa\frac{\partial^2(\tilde{\rho}C_p\bar{\theta})}{\partial x_j\partial x_j} - \frac{\partial(\tilde{\rho}C_pq_j)}{\partial x_j}, \tag{3.1}$$

where $q_j$ represents subgrid-scale heat flux:

$$q_j^{ls} = \overline{u_j\theta} - \bar{u}_j\bar{\theta}. \tag{3.2}$$

In Eq. (3.2) superscript "ls" stands for "large scales" meaning that the quantity is defined based on the large scales. Now, the test filter (see 2.3.3) is applied on the Eq. (3.1), and by direct analogy to SGS heat flux, Eq. (3.2), subtest-scale heat flux is defined as

$$Q_j^{ls} = \widehat{\overline{u_j\theta}} - \hat{\bar{u}}_j\hat{\bar{\theta}}. \tag{3.3}$$

Since both $q_j^{ls}$ and $Q_j^{ls}$ cannot be directly calculated, it is necessary to relate these terms to

the resolved fields, for what the Germano identity, Eq. (2.71), can be applied:

$$P_j^{ls} = Q_j^{ls} - \hat{q}_j^{ls} = \left(\widehat{\overline{u_j\theta}} - \hat{\bar{u}}_j\hat{\bar{\theta}}\right) - \left(\widehat{\overline{u_j\theta}} - \widehat{\bar{u}_j\bar{\theta}}\right)$$
$$= \widehat{\bar{u}_j\bar{\theta}} - \hat{\bar{u}}_j\hat{\bar{\theta}}. \tag{3.4}$$

Term, $P_j^{ls}$, is called test-window heat flux and it can be explicitly calculated from the large scales.

As it was mentioned above, subgrid-scale heat fluxes can be modeled by standard gradient diffusion hypothesis, and the one equation model is used for the momentum equation. Furthermore, it is assumed that there exists a model coefficient, $c_t$, which is a function of position, such that subgrid-scale heat fluxes at grid and test filter levels can be modeled as:

$$q_j^{ca} = -\frac{c_k}{Pr_{sgs}}\Delta k^{1/2}\frac{\partial\bar{\theta}}{\partial x_j} = -c_t\Delta k^{1/2}\frac{\partial\bar{\theta}}{\partial x_j}, \tag{3.5}$$

$$Q_j^{ca} = -\frac{c_k}{Pr_{sgs}}\hat{\Delta}K^{1/2}\frac{\partial\hat{\bar{\theta}}}{\partial x_j} = -c_t\hat{\Delta}K^{1/2}\frac{\partial\hat{\bar{\theta}}}{\partial x_j}, \tag{3.6}$$

$$c_t \equiv \frac{c_k}{Pr_{sgs}}, \tag{3.7}$$

where $\Delta$ and $\hat{\Delta}$ are grid and test filter width and throughout this work a ratio $\hat{\Delta} = 2\Delta$ will be used and superscript "ca" is abbreviation for "closure approximation" meaning that the quantity is evaluated by using the models. Turbulent kinetic energies at "grid" and "test" levels, $k$ and $K$ are given in the equations (2.100) and (2.101). Consistency between (3.5) and (3.6) depends on a proper local choice of $c_t$, see e.g. Lilly [66].

Let an expression relating the closure approximations (3.5) and (3.6) be defined as:

$$P_j^{ca} = Q_j^{ca} - \hat{q}_j^{ca} = -c_t\alpha_j + \widehat{c_t\beta_j}, \tag{3.8}$$

where

$$\alpha_j \equiv \hat{\Delta}K^{1/2}\frac{\partial\hat{\bar{\theta}}}{\partial x_j}, \tag{3.9}$$

and

$$\beta_j \equiv \Delta k^{1/2}\frac{\partial\bar{\theta}}{\partial x_j}. \tag{3.10}$$

Both (3.4) and (3.8) are relating turbulent heat fluxes at two filtering levels and in the case of ideal modeling these expressions should give the same values, $P_j^{ls} = P_j^{ca}$. This statement can be exploited further to derive the equation for $c_t$. The error between (3.4) and (3.8) can be defined as:

$$E_j = P_j^{ls} - P_j^{ca} = P_j^{ls} + \alpha_j c_t - \widehat{c_t\beta_j}. \tag{3.11}$$

System of equations (3.11) represents a system of three integral equations in just one unknown, $c_t$. The optimal solution, which yields the consistency between expressions (3.5) and (3.6), can be obtained by minimizing the square of the error $E_j$. In calculus of variations, this is achieved by finding the extremal function of the functional:

$$\Phi[c_t] = \int_V E_j(\vec{r})E_j(\vec{r})d\vec{r}, \tag{3.12}$$

where $\vec{r}$ is a position vector and integration is over the whole computational domain.

In general, there are two possible solutions to find $c_t$. First, the more simple way, is to assume that $c_t$ does not depend on position. This will produce a single, volume averaged constant, which changes dynamically as simulation progresses in time

$$c_t = f(t). \tag{3.13}$$

This method will be presented in 3.1.1.

Second possibility is to think of $c_t$ as a function of position which will require a solution of the variational problem (3.12). The model coefficient $c_t$ derived in this manner will be locally dependent but this is to be paid by a more complicated set of equations and harder numerical implementation.

$$c_t = f(\vec{r}, t). \tag{3.14}$$

This method is given in 3.1.2.

### 3.1.1 Volume averaged $Pr_{sgs}$

If we assume that $c_t$ does not depend on position, i.e. it has one single value for the whole computational domain, then the functional (3.12) reduces to a function since $c_t$ can be taken out from the filtering operation in (3.11). The optimal value for $c_t$ will be the minimum point of the function:

$$F = \int_V E_j(\vec{r}) E_j(\vec{r}) d\vec{r}, \tag{3.15}$$

where $E_j$ is reduced to:

$$E_j = P_j^{ls} - c_t m_j, \tag{3.16}$$

and

$$m_j \equiv -\alpha_j + \widehat{\beta}_j. \tag{3.17}$$

$E_j$ from (3.15) is substituted with (3.16) and after setting the first derivative with respect to $c_t$ to zero:

$$\frac{\partial F}{\partial c_t} = \frac{\partial}{\partial c_t} \int_V \left( (P_j^{ls})^2 - 2 c_t m_j P_j^{ls} + c_t^2 m_j^2 \right) d\vec{r} = 0, \tag{3.18}$$

one finally gets the expression for $c_t$:

$$c_t = \frac{\langle P_j^{ls} m_j \rangle}{\langle m_j m_j \rangle}, \tag{3.19}$$

where the angular bracket represents volume averaging. It is easy to see that the second derivative of (3.15) with respect to $c_t$ is always positive which means that (3.19) really represents the optimal value. Finally, the subgrid-scale turbulent Prandtl number is:

$$Pr_{sgs} = \frac{c_k}{c_t}. \tag{3.20}$$

The model for $Pr_{sgs}$ described with the equations (3.19) and (3.20) is very simple to implement and it does not require significant increase of computational costs. It's favorable feature is self-adaptivity to different flow and heat transfer regimes without any *a priori* tuning of $Pr_{sgs}$. Moreover, the model showed stable behavior even when simulations were started from uniform internal fields (zero-gradients). Disadvantage of the model might be the fact that $Pr_{sgs}$ has one value for the whole computational domain independent of the local flow and heat transfer conditions.

### 3.1.2 Locally dependent $Pr_{sgs}$

When the model coefficient $c_t$ is not a single constant but a function depending on the position, an extremal function for the functional (3.12) has to be found. This procedure is given in Ghosal et al. [36] and we are going to use the same technique for this case.

To find the extremal function for the functional (3.12), we set the variation of $\Phi$ to zero:

$$\begin{aligned}\delta\Phi[c_t] &= \delta\int_V E_j(\vec{r})E_j(\vec{r})d\vec{r} = \int_V \left(\delta E_j(\vec{r})E_j(\vec{r}) + \delta E_j(\vec{r})E_j(\vec{r})\right)d\vec{r} = 0 \\ &= 2\int_V E_j(\vec{r})\delta E_j(\vec{r})d\vec{r} = 0.\end{aligned} \tag{3.21}$$

Variation of $E_j(\vec{r})$ is defined as:

$$\delta E_j(\vec{r}) = \frac{\partial E_j(\vec{r})}{\partial c_t(\vec{r})}\delta c_t(\vec{r}) = \alpha_j(\vec{r})\delta c_t(\vec{r}) - \widehat{\beta_j(\vec{r})\delta c_t(\vec{r})}. \tag{3.22}$$

Introducing (3.22) in (3.21) yields:

$$\int_V \left(E_j(\vec{r})\alpha_j(\vec{r})\delta c_t(\vec{r}) - E_j(\vec{r})\widehat{\beta_j(\vec{r})\delta c_t(\vec{r})}\right)d\vec{r} = 0. \tag{3.23}$$

From the the definition of filtering in LES, follows from (3.23):

$$\int_V \left(E_j(\vec{r})\alpha_j(\vec{r})\delta c_t(\vec{r}) - E_j(\vec{r})\int_V G(\vec{r},\vec{\xi})\beta_j(\vec{\xi})\delta c_t(\vec{\xi})d\vec{\xi}\right)d\vec{r} = 0, \tag{3.24}$$

or:

$$\int_V E_j(\vec{r})\alpha_j(\vec{r})\delta c_t(\vec{r})d\vec{r} - \int_V\int_V E_j(\vec{r})G(\vec{r},\vec{\xi})\beta_j(\vec{\xi})\delta c_t(\vec{\xi})d\vec{\xi}d\vec{r} = 0. \tag{3.25}$$

Throughout this work the box filter is applied. It is defined as:

$$G(\vec{\xi},\vec{r}) := \begin{cases}\frac{1}{\Delta} & \text{if } |\vec{\xi}-\vec{r}| \le \frac{\Delta}{2} \\ 0 & \text{otherwise}\end{cases}, \tag{3.26}$$

Because the computational domain is a finite Euclidean space, the following equality holds:

$$|\xi - r| = |r - \xi| \rightarrow G(\vec{\xi},\vec{r}) = G(\vec{r},\vec{\xi}). \tag{3.27}$$

Now, it is possible to interchange $\vec{r}$ and $\vec{\xi}$ in Eq. (3.25), which yields:

$$\int_V E_j(\vec{r})\alpha_j(\vec{r})\delta c_t(\vec{r})d\vec{r} - \int_V\int_V E_j(\vec{\xi})G(\vec{\xi},\vec{r})\beta_j(\vec{r})\delta c_t(\vec{r})d\vec{r}d\vec{\xi} = 0, \tag{3.28}$$

and after changing the order of integration:

$$\int_V E_j(\vec{r})\alpha_j(\vec{r})\delta c_t(\vec{r})d\vec{r} - \int_V \beta_j(\vec{r})\delta c_t(\vec{r})\int_V E_j(\vec{\xi})G(\vec{\xi},\vec{r})d\vec{\xi}d\vec{r} = 0. \tag{3.29}$$

Equation (3.29) can be rewritten as:

$$\int_V \left(E_j(\vec{r})\alpha_j(\vec{r}) - \beta_j(\vec{r})\int_V E_j(\vec{\xi})G(\vec{r},\vec{\xi})d\vec{\xi}\right)\delta c_t(\vec{r})d\vec{r} = 0. \tag{3.30}$$

Equation (3.30) holds when either term in the bracket is zero, or $\delta c_t = 0$. Since we are interested in a non-trivial solution, that is, $\delta c_t \neq 0$, Eq. (3.30) reduces to:

$$E_j(\vec{r})\alpha_j(\vec{r}) - \beta_j(\vec{r})\int_V E_j(\vec{\xi})G(\vec{r},\vec{\xi})d\vec{\xi} = 0. \tag{3.31}$$

The integral in Eq. (3.31) represents filtering, so that we can write:

$$E_j(\vec{r})\alpha_j(\vec{r}) = \beta_j(\vec{r})\widehat{E_j(\vec{r})}, \tag{3.32}$$

and after substituting Eq. (3.11) into (3.32) we get:

$$\Big(P_j^{ls}(\vec{r}) + \alpha_j(\vec{r})c_t(\vec{r}) - \widehat{\beta_j(\vec{r})c_t(\vec{r})}\Big)\alpha_j(\vec{r}) = \beta_j(\vec{r})\Big(\widehat{P_j^{ls}(r) + \alpha_j(\vec{r})c_t(\vec{r}) - \widehat{\beta_j(\vec{r})c_t(\vec{r})}}\Big). \tag{3.33}$$

Equation (3.33) can be further rearranged as follows:

$$c_t(\vec{r}) = -f_j(\vec{r}) + \frac{1}{\alpha_j(\vec{r})\alpha_j(\vec{r})}\left[\underbrace{\alpha_j(\vec{r})\widehat{\beta_j(\vec{r})c_t(\vec{r})}}_{\text{A}} + \underbrace{\beta_j(\vec{r})\widehat{\alpha_j(\vec{r})c_t(\vec{r})}}_{\text{B}} - \underbrace{\beta_j(\vec{r})\widehat{\beta_j(\vec{r})c_t(\vec{r})}}_{\text{C}}\right], \tag{3.34}$$

$$f_j(\vec{r}) = \frac{1}{\alpha_j(\vec{r})\alpha_j(\vec{r})}\left[P_j^{ls}(\vec{r})\alpha_j(\vec{r}) - \beta_j(\vec{r})\widehat{P_j^{ls}(\vec{r})}\right], \tag{3.35}$$

where $f_j(\vec{r})$ can be explicitly evaluated from the large scales.

Further, Eq. (3.34) may be expressed as Fredholm integral equation of the second kind:

$$A = \int_V G(\vec{r},\vec{\xi})\alpha_j(\vec{r})\beta_j(\vec{\xi})c_t(\vec{\xi})d\vec{\xi}, \tag{3.36}$$

$$B = \int_V G(\vec{r},\vec{\xi})\beta_j(\vec{r})\alpha_j(\vec{\xi})c_t(\vec{\xi})d\vec{\xi}, \tag{3.37}$$

$$C = \int_V \beta_j(\vec{r})\beta_j(\vec{\xi})c_t(\vec{\xi})\int_V G(\vec{\zeta},\vec{r})G(\vec{\zeta},\vec{\xi})d\vec{\zeta}d\vec{\xi}, \tag{3.38}$$

which finally gives:

$$c_t(\vec{r}) = -f_j(\vec{r}) + \int_V H(\vec{r},\vec{\xi})c_t(\vec{\xi})d\vec{\xi}, \tag{3.39}$$

$$H(\vec{r},\vec{\xi}) = \frac{1}{\alpha_j(\vec{r})\alpha_j(\vec{r})}\left[H_A(\vec{r},\vec{\xi}) + H_A(\vec{\xi},\vec{r}) - H_B(\vec{r},\vec{\xi})\right], \tag{3.40}$$

$$H_A(\vec{r},\vec{\xi}) = G(\vec{r},\vec{\xi})\alpha_j(\vec{r})\beta_j(\vec{\xi}), \tag{3.41}$$

$$H_B(\vec{r},\vec{\xi}) = \beta_j(\vec{r})\beta_j(\vec{\xi})\int_V G(\vec{\xi},\vec{r})G(\vec{\xi},\vec{\xi})d\vec{\zeta}. \tag{3.42}$$

Equation (3.39) can be solved by applying the method proposed by Ghosal et al. [36]. When applied on (3.39), this methods yields the following iteration scheme:

$$c_t^n(\vec{r}) = \frac{1}{1-\mu g(x)}\left[-f_j(\vec{r}) + \int_V H(\vec{r},\vec{\xi})c_t(\vec{\xi})d\vec{\xi} - \mu g(x)c_t^{n-1}(\vec{r})\right], \tag{3.43}$$

where, for a top-hat filter:

$$g(\vec{r}) = \frac{2\alpha_{ij}(\vec{r})\beta_{ij}(\vec{r}) - \beta_{kl}(\vec{r})\beta_{kl}(\vec{r})}{\alpha_{mn}(\vec{r})\alpha_{mn}(\vec{r})}. \tag{3.44}$$

However, Piomelli and Liu [86] reported that the iterative scheme (3.43) - (3.44) leads to a significant increase of the computational time. Therefore, this method is not considered here.

A simple and easy to implement way to solve Eq. (3.34), is to replace $c_t(\vec{r})$ on the RHS of the equation with a value which is assumed to be known. This yields:

$$c_t^n(\vec{r}) = -f_j(\vec{r}) + \frac{1}{\alpha_j(\vec{r})\alpha_j(\vec{r})}\Big[\alpha_j(\vec{r})\widehat{\beta_j(\vec{r})c_t^*(\vec{r})} + \beta_j(\vec{r})\widehat{\alpha_j(\vec{r})c_t^*(\vec{r})} - \beta_j(\vec{r})\widehat{\beta_j(\vec{r})c_t^*(\vec{r})}\Big], \tag{3.45}$$

where $c_t^*(\vec{r})$ has to be determine yet. There are various ways to obtain $c_t^*(\vec{r})$ and some of them are given in [86]:

1. Use the value from the previous time step:
$$c_t^*(\vec{r}) = c_t^{n-1}(\vec{r}). \tag{3.46}$$
2. Estimate the value:
$$c_t^*(\vec{r}) = c_t^{n-1}(\vec{r}) + \Delta t \frac{\partial c_t(\vec{r})}{\partial t} + \dots, \tag{3.47}$$
where $\Delta t$ is a time step.
3. Iterative scheme: use a value for $c_t^*(\vec{r})$ from the previous time step and then solve (3.45). Afterwards, within the same time step but in the second inner-iteration, a newly calculated value for $c_t^*(\vec{r})$ is used instead of $c_t^*(\vec{r})$ to solve (3.45) and iteration process is repeated until convergence is reached.

Since the second and third methods would require additional computational cost, we approximate $c_t^*(\vec{r})$ by using the value from the previous time step. As a result, implementation of Eq. (3.45) is very simple and without significant increase of computational effort compared to volume averaged method (see 3.1.1).

The model coefficient obtained by solving the Eq. (3.45) locally depends on the flow field and heat transfer. If in some regions of the flow field values for $c_t(\vec{r})$ become very high, which may cause stability problems, local averaging over the neighboring grid points can be applied. These extreme situations are likely to occur if simulation is started from uniform velocity and temperature fields.

## 3.2 Dynamic subgrid-scale heat flux model

In this section, a dynamic model for subgrid-scale heat flux, based on the transport equation, is proposed. In the first part of the section, 3.2.1, we propose an algebraic model for subgrid-scale heat flux. In the second part, 3.2.2, dynamic procedure is applied once again to calculate model coefficients $c_1$ and $c_2$. Same as for $Pr_{sgs}$, model coefficients can be treated as volume averaged, or locally dependent.

### 3.2.1 Model for subgrid-scale heat flux

Transport equation for the subgrid-scale heat flux can be derived from momentum and energy equations and it reads as follows:

$$\begin{aligned}\frac{\partial \overline{u_i'\theta'}}{\partial t} + \bar{u}_j \frac{\partial \overline{u_i'\theta'}}{\partial x_j} = &-\frac{\partial}{\partial x_j}\left(\overline{u_i'u_j'\theta'} + \frac{1}{\rho}\delta_{i,j}\overline{p'\theta'} - \kappa\overline{u_i'\frac{\partial\theta'}{\partial x_j}} - \nu\overline{\theta'\frac{\partial u_i'}{\partial x_j}} - \overline{\tau_{ij}\theta'} - \overline{q_j u_i'}\right)\\ &- \left(\overline{u_i'u_j'}\frac{\partial\bar{\theta}}{\partial x_j} + \overline{u_j'\theta'}\frac{\partial\bar{u}_i}{\partial x_j}\right) - \beta g_i\overline{\theta'^2} + \frac{1}{\rho}\overline{p'\frac{\partial\theta'}{\partial x_i}} - (\nu+\kappa)\overline{\frac{\partial u_i'}{\partial x_j}\frac{\partial\theta}{\partial x_j}}\\ &- \overline{\tau_{ij}\frac{\partial\theta'}{\partial x_j}} - \overline{q_j\frac{\partial u_i'}{\partial x_j}}.\end{aligned} \tag{3.48}$$

As it was mentioned before, the simplest model for $\overline{u_i'\theta'}$ is the one based on the simple gradient diffusion hypothesis which is commonly used in CFD for both RANS and LES. It is well

known from the literature, e.g. Otic [80], that this method fails to give good prediction for heat transfer in the conditions where the buoyancy effects are of significant importance. In order to improve modeling for buoyancy dominated flows, buoyancy effects need to be included in the modeled equation for SGS heat flux.

If we now examine the transport equation for SGS heat flux, Eq. (3.48), we see that the buoyancy term includes the temperature variance, $\overline{\theta'^2}$, which is a measure for the temperature fluctuations on the same manner as the turbulent kinetic energy is a measure for the fluctuations of velocity field. This means that, if we want to include the buoyancy term into the modeled equation for SGS heat flux, we have either to solve the transport equation for temperature variance, which is given by the equation (3.49), or to provide an adequate modeled expression for it.

$$\frac{\partial\overline{\theta'^2}}{\partial t}+\bar{u}_j\frac{\partial\overline{\theta'^2}}{\partial x_j}=-\frac{\partial}{\partial x_j}\left(\overline{u_j'\theta'^2}-\kappa\frac{\partial\overline{\theta'^2}}{\partial x_j}\right)-2\overline{u_j'\theta'}\frac{\partial\bar{\theta}}{\partial x_j}-2\kappa\overline{\frac{\partial\theta'}{\partial x_j}\frac{\partial\theta'}{\partial x_j}}. \tag{3.49}$$

Double and triple correlations appearing in (3.49) require further modeling which produces new constants that have to be prescribed or dynamically calculated as the simulation progresses in time. Unfortunately, this significantly increases both complexity and computational costs. It is important to keep in mind that LES lays between RANS and DNS and one of the main characteristics is that the effects of small scales can be estimated by using the models which are, in general, more simple than the models used in RANS. Since our goal is to propose a new model for the flows where buoyancy plays an important role and at the same time keep the model as simple as possible, we skip solving Eq. (3.49) and, instead of that, approximate temperature variance, $\theta'^2$, with the expression proportional to the production term. This approach is widely used, see e.g. Launder [63] who has suggested that the unknown terms may be modeled by invoking the so called WET (*Wealth* $\propto$ *Earnings* $\times$ *Time*) hypothesis, which states that an unknown term is proportional to it's generation (production) rate. Afterwards, this newly obtained expression for buoyancy production is added to the gradient diffusion model and eventually a new model is proposed. Derivation of the model is shown through the equations (3.50) to (3.55).

We start from the production term in temperature variance equation, Eq. (3.49), which reads as follows:

$$P_\theta=-2\overline{u_j'\theta'}\frac{\partial\bar{\theta}}{\partial x_j}. \tag{3.50}$$

Production of SGS heat flux due to the buoyancy effects is given by the following term:

$$P_\beta=-\beta g_i\overline{\theta'^2}. \tag{3.51}$$

Temperature variance in equation (3.51) is replaced with the term proportional to (3.50) and multiplied by a constant of proportionality. In addition, dimensional analysis is used and new expression for buoyancy production term is derived:

$$B=c_2\Delta\beta\frac{g_j}{|g|}\overline{u_j'\theta'}\frac{\partial\bar{\theta}}{\partial x_j}, \tag{3.52}$$

where $c_2$ represents a model coefficient and $\Delta$ is filter width. Equation (3.52) is subsequently added to the gradient diffusion approximation, which yields the following expression for SGS heat flux:

$$\overline{u_i'\theta'}=-\left(\frac{\nu_t}{Pr_{sgs}}\frac{\partial\bar{\theta}}{\partial x_j}+c_2\Delta\beta\frac{g_j}{|g|}\overline{u_j'\theta'}\frac{\partial\bar{\theta}}{\partial x_j}\right), \tag{3.53}$$

which after rearranging the eddy viscosity, $\nu_t=c_k\Delta\sqrt{k}$, takes the following form:

$$\overline{u_j'\theta'}=-\left(c_1\Delta\sqrt{k}\frac{\partial\bar{\theta}}{\partial x_j}+c_2\Delta\beta\frac{g_j}{|g|}\overline{u_j'\theta'}\frac{\partial\bar{\theta}}{\partial x_j}\right), \tag{3.54}$$

where $c_1 = c_k / Pr_{sgs}$.

Equation (3.54) is implicitly defined and for the numerical implementation SGS heat flux on the RHS $\overline{u_j'\theta'}$ is replaced by its value from the previous time step. This yields the final expression for the proposed model for SGS heat flux:

$$\overline{u_j'\theta'}^n = -\left( c_1 \Delta \sqrt{k} \frac{\partial \bar{\theta}}{\partial x_j} + c_2 \Delta \beta \frac{g_j}{|g|} \overline{u_j'\theta'}^{(n-1)} \frac{\partial \bar{\theta}}{\partial x_j} \right). \tag{3.55}$$

In the above equation, $g_j$, $\beta$ and $\overline{u_j'\theta'}^{(n-1)}$ are gravity, coefficient of thermal expansion and SGS heat flux from the previous time step.

Equation (3.55) is the model for subgrid-scale heat flux for the flows where buoyancy has significant influence. Depending on the constraints imposed when deriving the dynamic equations for $c_1$ and $c_2$, these coefficients can take either single values for the whole computational domain, or alternatively, they can vary locally. In both cases, model coefficients are calculated dynamically in time. Derivation of the dynamic equations for $c_1$ and $c_2$ is given in the succeeding subsections. Application of the model is given in the next chapter.

### 3.2.2 Determination of model coefficients

To close the model for SGS heat flux, Eq. (3.55), once again the well known dynamic procedure is applied. Unlike the dynamic model for subgrid-scale turbulent Prandtl number, where only one model coefficient, $c_t$, was unknown, in this case there are two unknown model coefficients, $c_1$ and $c_2$.

In particular, there are two different approaches to determine $c_1$ and $c_2$. First approach would be to treat $c_1$ and $c_2$ independently of each other: $c_1$ is derived by assuming that $c_2 = 0$ and vice versa. This yields two dynamic equation: one for $c_1$ and the other for $c_2$, where the equation for $c_1$ is exactly the same as the equation for $c_t$, Eq. (3.19). When deriving the equation for $c_2$, instead of (3.9) and (3.10) one has to use:

$$\alpha_{j2} \equiv 2\Delta\beta \frac{g_j}{g} Q_j^{n-1} \frac{\partial \hat{\bar{\theta}}}{\partial x_j}, \tag{3.56}$$

and

$$\beta_{j2} \equiv \Delta\beta \frac{g_j}{|g|} q_j^{n-1} \frac{\partial \bar{\theta}}{\partial x_j}. \tag{3.57}$$

This approach will be called *uncoupled* and final forms of the equations for $c_1$ and $c_2$ will be given later in this section.

In the second approach, equations for $c_1$ and $c_2$ are derived in a *coupled* manner which means that no additional assumptions are introduced (it is not necessary to set one coefficient to zero when determining the other one). Behavior of the model coefficient $c_1$ is explicitly influenced by $c_2$ and vice versa. As a result, a system of two linear algebraic equations whose solution yields $c_1$ and $c_2$ is obtained. Derivation of the model is given next.

By following the same procedure as for the determination of the subgrid-scale turbulent Prandtl number (see Sect. 3.1), and using the new model for closure approximation, (3.55),

subgrid-scale heat fluxes at grid, $q_j^{ca}$, and test filter level, $Q_j^{ca}$, are given as follows:

$$q_j^{ca} = -\left( c_1 \Delta \sqrt{k} \frac{\partial \bar{\theta}}{\partial x_j} + c_2 \Delta \beta \frac{g_j}{|g|} q_j^{n-1} \frac{\partial \bar{\theta}}{\partial x_j} \right), \tag{3.58}$$

$$Q_j^{ca} = -\left( c_1 \hat{\Delta} \sqrt{K} \frac{\partial \hat{\bar{\theta}}}{\partial x_j} + c_2 \hat{\Delta} \beta \frac{g_j}{|g|} Q_j^{n-1} \frac{\partial \hat{\bar{\theta}}}{\partial x_j} \right). \tag{3.59}$$

When applied on the equations (3.58) and (3.59), Germano identity, [34] yields the following expressions which relate SGS heat fluxes at two filtering levels:

$$P_j^{ca} = Q_j^{ca} - \hat{q}_j^{ca} = -c_1\alpha_1 + \widehat{c_1\beta_1} - c_2\alpha_2 + \widehat{c_2\beta_2}, \tag{3.60}$$

$$\alpha_1 = 2\Delta \sqrt{K} \frac{\partial \hat{\bar{\theta}}}{\partial x_j}, \quad \alpha_2 = 2\Delta\beta \frac{g_j}{g} Q_j^{n-1} \frac{\partial \hat{\bar{\theta}}}{\partial x_j}, \tag{3.61}$$

$$\beta_1 = \Delta \sqrt{k} \frac{\bar{\theta}}{\partial x_j}, \quad \beta_2 = \Delta\beta \frac{g_j}{|g|} q_j^{n-1} \frac{\partial \bar{\theta}}{\partial x_j}. \tag{3.62}$$

Again, the "error" between test window heat fluxes, Eq. (3.4), and closure approximations, equations (3.58) and (3.59) is introduced:

$$E_j = P_j^{ls} - P_j^{ca} = P_j^{ls} - \left[ -c_1\alpha_1 + \widehat{c_1\beta_1} - c_2\alpha_2 + \widehat{c_2\beta_2} \right]. \tag{3.63}$$

In general case both $c_1$ and $c_2$ are functions of position and in order to find functions $c_1$ and $c_2$ which make functional $\Phi$ stationary (minimize the error):

$$\Phi[c_1, c_2] = \int_V E_j(\vec{r}) E_j(\vec{r}) d\vec{r}, \tag{3.64}$$

one has to solve two Euler-Lagrange equations (see e.g. [9], [5]). Same as it was done for subgrid-scale turbulent Prandtl number, there are two possibilities to determine $c_1$ and $c_2$. First possibility is to assume that constants do not depend on position, which reduces the functional $\Phi$ to a function of two variables. In this case are the model coefficients functions only of time

$$c_1 = f(t), \qquad c_2 = f(t). \tag{3.65}$$

This approach is presented in 3.2.3.

Second possibility is to treat $c_1$ and $c_2$ as functions which depend on both position and time

$$c_1 = f(\vec{r}, t), \qquad c_2 = f(\vec{r}, t). \tag{3.66}$$

Locally dependent approach is given in 3.2.4.

### 3.2.3 Volume averaged model coefficients

First, let impose a constraint that model coefficients do not depend on the position. This is a strong assumption which can be justified for homogeneous flows. By doing so, both model derivation and later numerical implementation are significantly simplified.

If $c_1$ and $c_2$ are spatially independent, then these can be taken out from the filtering operation in (3.63) and functional (3.64) reduces to a function of two variables:

$$F(c_1, c_2) = \int_V E_j(\vec{r}) E_j(\vec{r}) d\vec{r}. \tag{3.67}$$

Optimal values for $c_1$ and $c_2$ are those that minimize the function $F(c_1, c_2)$. Because the test filter in (3.63) does not affect the model coefficients, error $E_j$ is now:

$$E_j = P_j^{ls} - c_1 m_{j1} - c_2 m_{j2}, \tag{3.68}$$

$$m_{j1} = \hat{\beta}_1 - \alpha_1, \quad m_{j2} = \hat{\beta}_2 - \alpha_2, \tag{3.69}$$

and $\alpha_1, \alpha_2, \beta_1$ and $\beta_2$ are given by (3.61) and (3.62). Expression (3.68) is substituted in (3.67) to give a function:

$$F(c_1, c_2) = \int_V \Big( P_j^{ls2}(\vec{r}) - 2c_1 m_{j1}(\vec{r}) P_j^{ls}(\vec{r}) - 2c_2 m_{j2}(\vec{r}) P_j^{ls}(\vec{r}) + 2c_1 c_2 m_{j1}(\vec{r}) m_{j2}(\vec{r}) + c_1^2 m_{j1}^2(\vec{r}) + c_2^2 m_{j2}^2(\vec{r}) \Big) d\vec{r}. \tag{3.70}$$

Afterwards, first derivatives with respect to $c_1$ and $c_2$ are set to zero, $\frac{\partial F(c_1,c_2)}{\partial c_1} = 0$ and $\frac{\partial F(c_1,c_2)}{\partial c_2} = 0$, which gives following relations for model coefficients:

$$c_1 = \frac{\langle P_j^{ls} m_{j1} - c_2 m_{j1} m_{j2} \rangle}{\langle m_{j1} m_{j1} \rangle}, \tag{3.71}$$

$$c_2 = \frac{\langle P_j^{ls} m_{j2} - c_1 m_{j1} m_{j2} \rangle}{\langle m_{j2} m_{j2} \rangle}, \tag{3.72}$$

where $\langle\rangle$ represents volume averaging. Mode coefficients calculated on this way represent the optimal values since the second derivatives of $F(c_1, c_2)$ with respect to $c_1$ and $c_2$ are always positive.

Equations (3.71) and (3.72) represent a system of two linear equations with two unknowns. Written in matrix form, the system of equations is:

$$\begin{bmatrix} 1 & \frac{\langle m_{j1} m_{j2} \rangle}{\langle m_{j1} m_{j1} \rangle} \\ \frac{\langle m_{j1} m_{j2} \rangle}{\langle m_{j2} m_{j2} \rangle} & 1 \end{bmatrix} \cdot \begin{bmatrix} c_1 \\ c_2 \end{bmatrix} = \begin{bmatrix} \frac{\langle P_j^{ls} m_{j1} \rangle}{\langle m_{j1} m_{j1} \rangle} \\ \frac{\langle P_j^{ls} m_{j2} \rangle}{\langle m_{j2} m_{j2} \rangle} \end{bmatrix}. \tag{3.73}$$

Since the numbers of unknowns and and equations are same, the system of linear equations (3.73) has an unique solution which is found by applying the Gaussian elimination. Model coefficients evaluated by solving the system (3.73) have a single values for the whole flow field. Those values are changing dynamically in time and if we considered a steady state case, they will tend to some constant values if the simulation has progressed long enough in time. Furthermore the model is self-adaptive to the heat transfer regime (forced or mixed convection) by adjusting $c_1$ or $c_2$. For example, if the considered case is a purely forced convection, $c_2$ will become less important, reducing the model to the simple gradient diffusion model with dynamically calculated subgrid-scale turbulent Prandtl number. The fact that the model coefficients have "global", but not the "local" values is a drawback which can become important if the flow has strong local variations of flow and temperature fields. This problem is solved by not using the constraint that model coefficients do not depend on position and this is given in the next subsection.

#### Uncoupled case

Second possibility to derive the equations for model coefficients $c_1$ and $c_2$ is to treat them independently of each other. This means that we have to set one of the coefficient to zero

in order to derive the equation for the other and vice versa. Derived on this way, model coefficients do not explicitly affect each other. If this is the case, for $c_1$ Eq. (3.19) can be used:

$$c_1 = \frac{\langle P_j^{ls} m_j \rangle}{\langle m_j m_j \rangle}, \tag{3.74}$$

where $P_j^{ls}$ and $m_j$ are given by Eq. (3.4) and Eq. (3.17) respectively.

Dynamic equation for $c_2$ has the similar form:

$$c_2 = \frac{\langle P_j^{ls} m_{j2} \rangle}{\langle m_{j2} m_{j2} \rangle}, \tag{3.75}$$

where Eq. (3.69) determines $m_{j2}$.

### 3.2.4 Locally dependent model coefficients

If the problem of interest is characterized by some kind of complex geometry and it includes phenomena like flow separation and reattachment, turbulent mixing, transition to turbulence, etc., which is very often the case in real engineering problems, local variations of $c_1$ and $c_2$ need to considered.

Since in this case we have two independent variables, two model coefficients, the value of the functional (3.64) depends on both $c_1(\vec{r})$ and $c_2(\vec{r})$, and in this case we will have to solve two Euler-Lagrange equations, one for each unknown. By carrying out the derivation similar to the one we used to determine locally dependent $Pr_{sgs}$ (see 3.1.2), we derive the equations for locally dependent $c_1(\vec{r})$ and $c_2(\vec{r})$.

To find the extremal functions that make the functional (3.64) stationary, variations of model coefficients are set to zero:

$$\delta\Phi|_{c_1} = 0 \quad \wedge \quad \delta\Phi|_{c_2} = 0. \tag{3.76}$$

These two conditions lead to the aforementioned two Euler-Lagrange equations. Complete derivation for the case of one dependent variable (locally dependent subgrid-scale turbulent Prandtl number) is given in 3.1.2 and it would be tedious to repeat the similar procedure here. Hence, we skip the derivation and write down the final forms of the equations for $c_1(\vec{r})$ and $c_2(\vec{r})$:

$$c_1^n(\vec{r}) = -f_{j1} + \frac{1}{\alpha_{j1}(\vec{r})\alpha_{j1}(\vec{r})} \Bigg[ \alpha_{j1}(\vec{r}) \widehat{\beta_{j1}(\vec{r}) c_1^{n-1}(\vec{r})} + \beta_{j1}(\vec{r}) \widehat{\alpha_{j1}(\vec{r}) c_1^{n-1}(\vec{r})} - \beta_{j1}(\vec{r}) \widehat{\widehat{\beta_{j1}(\vec{r}) c_1^{n-1}(\vec{r})}} \Bigg], \tag{3.77}$$

$$c_2^n(\vec{r}) = -f_{j2} + \frac{1}{\alpha_{j2}(\vec{r})\alpha_{j2}(\vec{r})} \Bigg[ \alpha_{j2}(\vec{r}) \widehat{\beta_{j2}(\vec{r}) c_2^{n-1}(\vec{r})} + \beta_{j2}(\vec{r}) \widehat{\alpha_{j2}(\vec{r}) c_2^{n-1}(\vec{r})} - \beta_{j2}(\vec{r}) \widehat{\widehat{\beta_{j2}(\vec{r}) c_2^{n-1}(\vec{r})}} \Bigg]. \tag{3.78}$$

In the above equation, superscript $n-1$ represents the previous time step, and $\alpha_{j1}$, $\alpha_{j2}$, $\beta_{j1}$ and $\beta_{j2}$ are given in (3.61) and (3.62). Nonhomogeneous parts, $f_{j1}$ and $f_{j2}$, known from

the large scales, are given as follows:

$$f_{j1} = \frac{1}{\alpha_{j1}(\vec{r})\alpha_{j1}(\vec{r})}\Bigg[P_j^{ls}(\vec{r})\alpha_{j1}(\vec{r}) - \alpha_{j1}(\vec{r})\alpha_{j2}(\vec{r})c_2^{n-1}(\vec{r}) + \alpha_{j1}(\vec{r})\widehat{\beta_{j2}(\vec{r})c_2^{n-1}(\vec{r})} - \beta_{j1}(\vec{r})\hat{P}_j^{ls} + \beta_{j1}(\vec{r})\widehat{\alpha_{j2}(\vec{r})c_2^{n-1}(\vec{r})} - \beta_{j1}(\vec{r})\widehat{\widehat{\beta_{j2}(\vec{r})c_2^{n-1}(\vec{r})}}\Bigg], \quad (3.79)$$

$$f_{j2} = \frac{1}{\alpha_{j2}(\vec{r})\alpha_{j2}(\vec{r})}\Bigg[P_j^{ls}(\vec{r})\alpha_{j2}(\vec{r}) - \alpha_{j2}(\vec{r})\alpha_{j1}(\vec{r})c_1^{n-1}(\vec{r}) + \alpha_{j2}(\vec{r})\widehat{\beta_{j1}(\vec{r})c_1^{n-1}(\vec{r})} - \beta_{j2}(\vec{r})\hat{P}_j^{ls} + \beta_{j2}(\vec{r})\widehat{\alpha_{j1}(\vec{r})c_1^{n-1}(\vec{r})} - \beta_{j2}(\vec{r})\widehat{\widehat{\beta_{j1}(\vec{r})c_1^{n-1}(\vec{r})}}\Bigg]. \quad (3.80)$$

Equations (3.77), (3.78), (3.79) and (3.80) complete the model. Initial tests shoved that the model coefficients calculated from the above equation set can experience very strong variations between neighboring computational cells (especially if the regions with uniform velocity and temperature fields occur within the computational domain). If this happens, than some kind of local averaging (averaging over the neighboring cells) have to be applied in order to stabilize computation. Alternatively, high variations of $c_1$ and $c_2$ can be limited to some acceptable range.

In the next chapter, new model for subgrid-scale heat flux is applied to simulate a turbulent mixed convection test case.

# Chapter 4

# Results

## 4.1 Introduction

This chapter is devoted to validation of the dynamic model for subgrid-scale heat flux which is given in 3.2.1. First part of the chapter, Sec. 4.2, deals with the dynamic model for subgrid-scale turbulent Prandtl number. Here, the model for $Pr_{sgs}$ is applied to simulate a heat transfer within a T-junction geometry for which purpose the well known Vattenfall benchmark experiment is used as a test case. Goal of this test is to investigate behavior and stability of the dynamic procedure which is, afterwards, applied to calculate model coefficients of the newly developed model for subgrid-scale heat flux.

In the second part of the chapter, Sec. 4.3, the dynamic model for subgrid-scale heat flux will be validated by simulating turbulent buoyant flow and heat transfer. Results will be compared with the experimental measurements and with the results obtained by using the standard gradient diffusion model with three different values for $Pr_{sgs}$: $0.1$, $0.9$ and $2$.

## 4.2 Vattenfall T-junction test case

As a test case for validation of the dynamic model for $Pr_{sgs}$, the well known T-junction benchmark experiment, conducted at Vattenfall test facility, Smith et al. [99], is chosen. Since the main purpose was to calculate model coefficients by applying the dynamic procedure, whose performances strongly depend on the stability, strong requirements were imposed on the possible test case. It was required that the test case fulfills some criteria regarding geometry, flow physics, fluid properties, etc.

- **Geometry.** Geometry that appears in the real engineering problem considerably differs from purely academic cases like simple pipes or channels. Unfortunately, complex geometry causes additional problems for experimental setup and increases costs, hence the experiments dealing with complex geometry are much rarer than those conducted on pipes or channels. This problem is even more highlighted when considering DNS where numerical schemes require additional attention and those kind of simulations are still a challenging task. T-junction configuration, together with some others like, i. e. forward and backward facing steps, flows around cylinders or cubes, etc., are usual choices among researchers. By using this kind of geometry it is possible to reproduce flow phenomena that are likely to appear in the real world. In a T-junction configuration we have intrusion of one fluid stream into another which leads to unsteady flow

field. Fluids are usually of different temperatures: higher temperature difference means higher requirement on the subgrid-scale model.

- **Flow physics.** In the case of simple geometry configuration, dynamic models will run smoothly with model coefficients rapidly converging to some constant values. Initial computations, that have been conducted on a turbulent channel test case, have proved this statement. In order to test the model in a more rigorous way, it is necessary to check its behavior if there exists some flow unsteadiness, like flow separation and reattachment, turbulent mixing, transition to turbulence, etc. Flow physics is closely related to the geometry.

- **Fluid properties.** Importance of SGS modeling depends on molecular fluid properties. For example, large thermal diffusivity of liquid metals, which is much larger than kinematic viscosity, smears out temperature fluctuations reducing the contribution of SGS model for a given numerical grid. Vice versa, SGS modeling in the case of water flow is much more important since low thermal diffusivity (compared to kinematic viscosity) makes the temperature field to decay slower than the velocity field. Because of that, this research is focused on test cases with water as a working fluid.

Some of the test cases available in the literature are listed in Tab. 4.1.

**Tab. 4.1:** List of test cases.

| Author | Year | Method | Working fluid |
|---|---|---|---|
| Suzuki et al. [103] | 1991 | Experiment | Water |
| Meinders and Hanjalic [73] | 1999 | Experiment | Air |
| Tokuhiro and Kimura [106] | 1999 | Experiment | Water |
| Miyake et al. [74] | 2001 | DNS | Air |
| Hattori and Nagano [39] | 2004 | DNS | Air |
| Nagano et al. [77] | 2004 | DNS | Air |
| Kruse and von Rohr [60] | 2006 | Experiment | Water |
| Kawamura et al. [51] | 2007 | DNS | Air |
| Hosseini et al. [41] | 2008 | Experiment | Water |
| Walker et al. [108] | 2009 | Experiment | Water |
| Smith et al. [99] | 2011 | Experiment | Water |
| Matsubara et al. [70] | 2012 | DNS | Pr = 0.025 to 5.0 |

Although a large database of turbulent heat transfer exists, it is hard to find a single test case which fulfills all the requirements mentioned above. The Vattenfall T-junction test case, Smith et al. [99] is chosen since it deals with water in a complex geometry. Deficiency is the rather limited temperature measurements, but this is not a critical issue since the main goal was to test the behavior of the dynamic procedure.

### 4.2.1 Test facility

The Vattenfall T-junction test facility is described in Smith et al. [99] and here will be given just a short description with the main parameters. Experimental configuration of the Vattenfall test facility is given in Fig. 4.1. A high-level reservoir provides a constant flow rate of cold water which is controled by the flow meter $Q_2$. In order to provide a high quality flow without large-scale turbulence or secondary flows, a stagnation chamber of diameter $400\,[mm]$ is mounted at the inlet of the horizontal pipe. The stagnation chamber is connected to a $10\,[m]$ long plastic

pipe section which is followed by a plexiglas section extending $1270\,[mm]$ upstream of the T-junction. Diameter of the pipe is $140\,[mm]$ with the total length exceeding $11.2\,[m]$ which is more than $80$ pipe diameters, assuring a fully developed velocity profile.

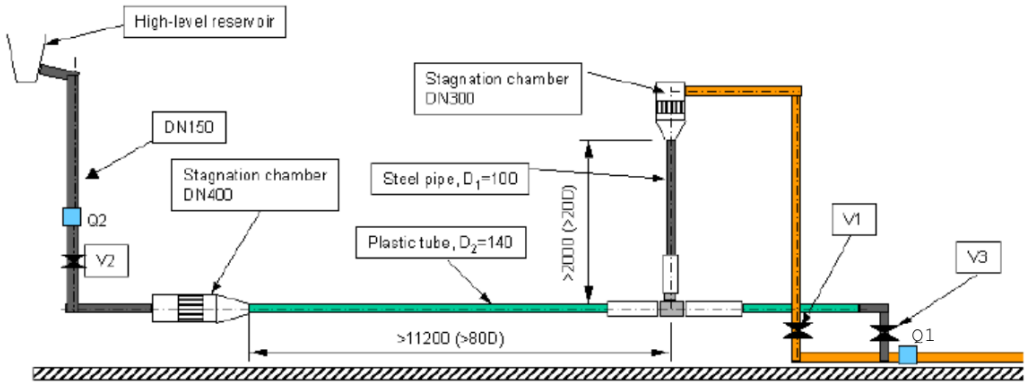


**Fig. 4.1:** T-junction test rig.

A pump is used to supply the system with hot water which is taken from a $70\,[m^3]$ reservoir and a flow meter $Q_1$ is used to control the flow rate, automatically adjustable by the control of the pump's rotational speed. Same as for the cold water, a stagnation chamber is used to provide a high quality flow. The stagnation chamber is connected to the more than $2\,[m]$ long steel pipe with the inner diameter $D_1 = 100\,[mm]$. Since the length to diameter ratio of the hot pipe is about 20, a fully developed velocity profile is not achieved.

In Fig. 4.2, a close up of the T-junction test section is shown. Curved surfaces of the pipes can distort the laser beams and in order to prevent it, each of the three pipes is surrounded by a rectangular water box. LDA measurements have been taken $3$ diameters upstream of the junction for the cold pipe and $3.1$ diameters upstream for the hot pipe. These flow measurements provide inlet boundary conditions for velocity and they confirm fully developed flow for the cold, and not fully developed flow for the hot water. Finally, the pipe walls are considered adiabatic.

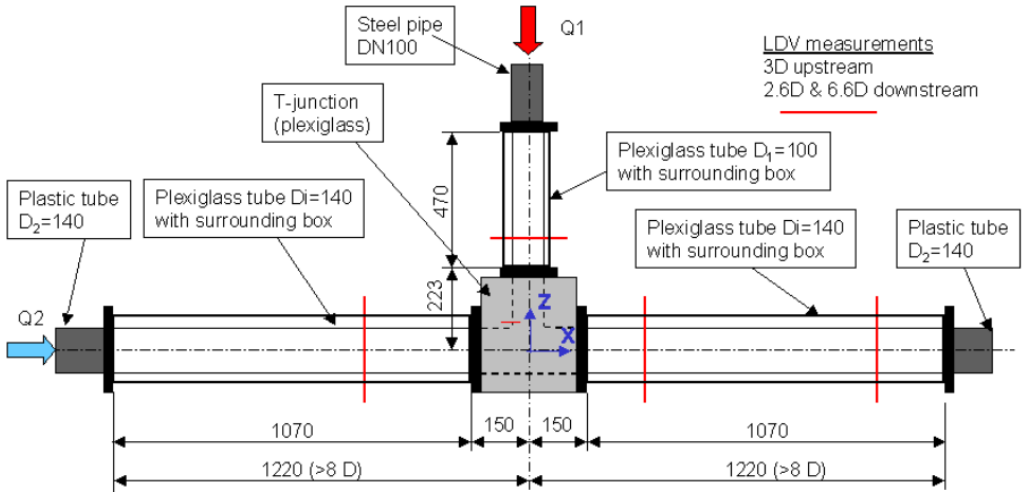


**Fig. 4.2:** T-junction test section close up.

### 4.2.2 Inlet boundary conditions

Flow rates and temperatures together with Reynolds numbers based on the volumetric flow rates are listed in Tab. 4.2. The measuring location was $420\,[mm]$ upstream of the T-junction for the cold (main) pipe and $310\,[mm]$ upstream of the T-junction for hot (branch) pipe. A uniform distribution of the temperature is assumed and, because of that, just one thermocouple is used.

**Tab. 4.2:** Inlet boundary conditions

| | Temperature $[°C]$ | Diameter $[mm]$ | Flow rate $[l/s]$ | Re $[-]$ |
|---|---|---|---|---|
| Cold pipe | 19 | 140 | 9.0 | 79400 |
| Hot pipe | 36 | 100 | 6.0 | 107000 |

A two component LDA system is used to measure velocity in two perpendicular directions: one in the main flow direction and the other one transverse to the first one. The coordinate system adopted is shown in Fig. 4.3 and the measured velocity is given in Fig. 4.4, where $U_{bulk}$ represents the bulk velocity determined by the volumetric flow rate.

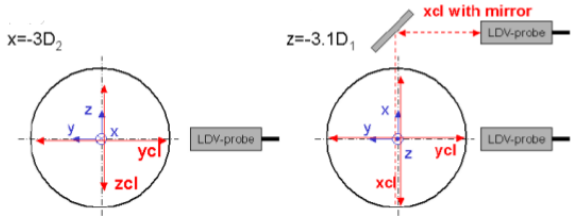


**Fig. 4.3:** LDA measurements coordinate system.

It must be mentioned that the upstream velocity measurements shown here are actually the scaled measurements from the previous experiment done by Westin et al. [113] in which

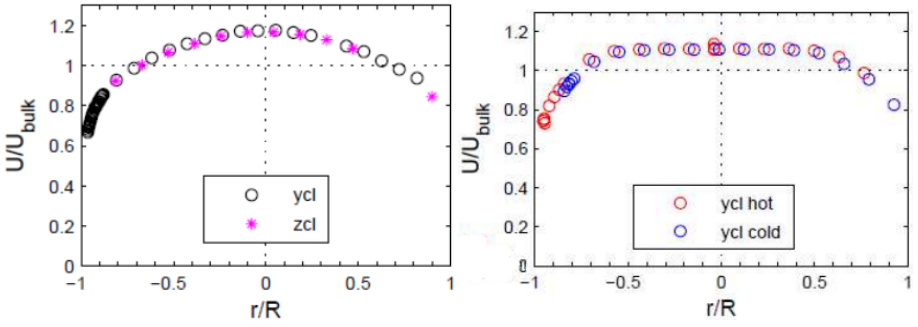


**(a)** Cold pipe **(b)** Hot pipe

**Fig. 4.4:** Velocity upstream measurements.

volumetric flow rates were $12\,[l/s]$ and $6\,[l/s]$ for cold and hot pipe respectively. In the present test, the hot water flow rate is kept the same while the flow rate of cold water is decreased to $9\,[l/s]$. Since the cold water velocity profile is fully developed, results from previous experiments are simply scaled. Velocity data shown here are later used as inlet boundary condition for CFD calculation. From Fig. 4.4, it can be seen that the velocity profile for the hot stream is not fully developed since the length of the hot pipe is only about 20 diameters. This velocity profile is almost impossible to reproduce by any kind of inflow boundary conditions and the discussion on the inflow boundary conditions and influence on the LES results will be given later in this section.

### 4.2.3 Computational setup

**Computational mesh** The computational mesh is block-structured, generated by Ansys ICEM CFD, [2]. By using the the block-structured mesh, it is possible to create a fine mesh in those regions of the domain where high resolution is required and, on the other hand, to keep the total number of cells at reasonable level. The mesh generated for this test case consists of 2.2 million cells and it is shown in Fig. 4.5. Meshes with different cell numbers

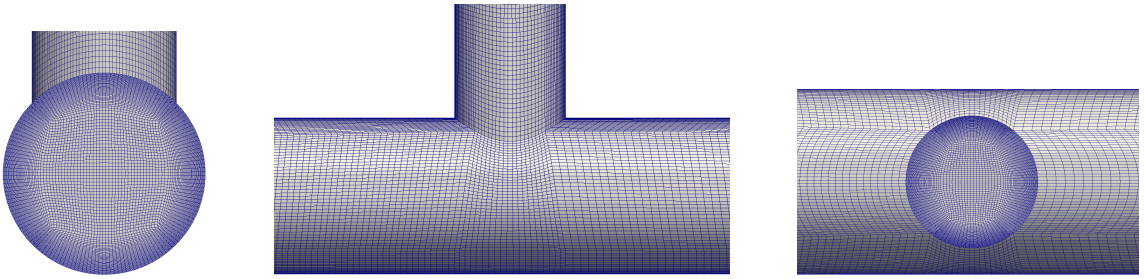

**(a)** Cold inlet **(b)** Junction **(c)** Hot inlet

**Fig. 4.5:** Block structured mesh.

have been tested too and it is found out that the one with 2.2 millions was the optimal solution. Any further increase of mesh number significantly increases computational costs, while the improvement of the simulation results was small. Computational domain and measuring locations are shown in Fig. 4.6.

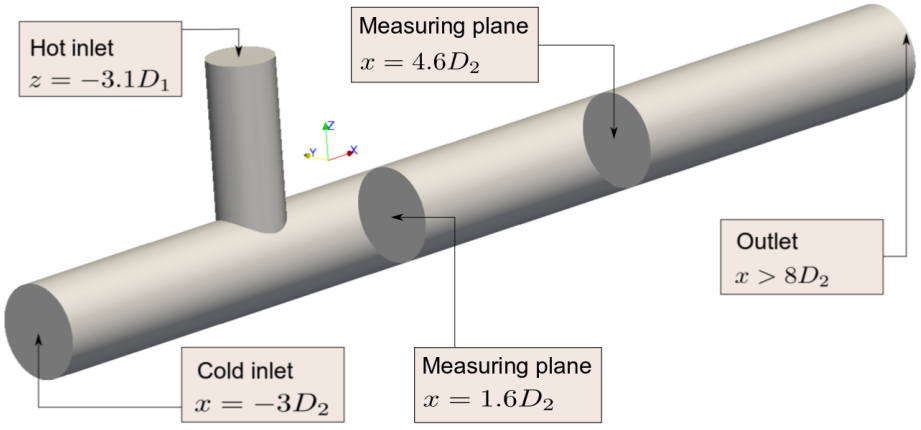


**Fig. 4.6:** Geometry and computational domain for T-junction test case.

**Boundary conditions** Boundary conditions for the simulation are defined by the experimental setup. Inlet velocities for the cold and hot inlet are interpolated from the experimental results shown in Fig. 4.4. Advective boundary conditions are used at the outlet, while a no-slip boundary condition is set on the walls. A low level of perturbations of the inlet velocity field, $10^{-5}$, is used in order to remove errors introduced by interpolating the experimental data.

For temperature, constant values of $19°C$ and $36°C$ are set for cold and hot inlet respectively. As it was suggested by the experimental setup, it is assumed uniform temperature distribution for both inlets. No additional perturbations of inlet temperature fields were introduced. Adiabatic boundaries are used for walls. Pressure inlets are zero-gradient, while the outlet is a fixed value.

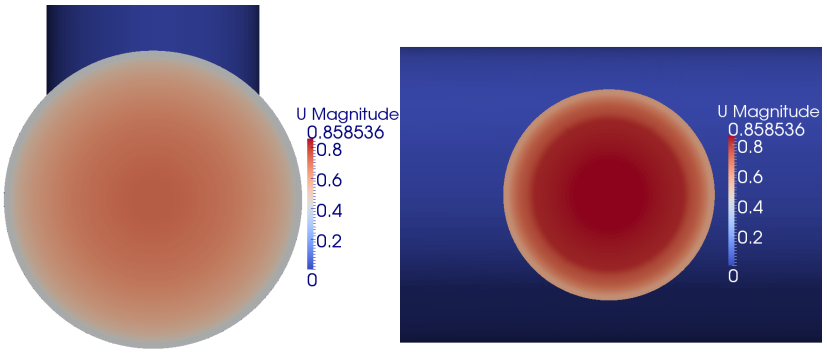


**(a)** Cold inlet **(b)** Hot inlet

**Fig. 4.7:** Interpolated velocities at the inlets.

**Fluid properties** There are two possibilities for choosing the fluid properties: constant, used in S1 (see Tab. 4.3) and temperature-dependent, used in other simulations. Temperature dependent fluid properties are calculated from the polynomials constructed by interpolating the data for water properties which are available in [64], for the temperature range from $15°C$ to $40°C$. Fluid properties are given by the following equations:

$$\rho(T) = 662.5 + 2.498\,T - 0.004616\,T^2, \tag{4.1}$$

$$C_p(T) = 6318 - 13.88\,T + 0.02252\,T^2, \tag{4.2}$$

$$\mu(T) = 0.03773 - 0.0002263\,T + 0.0000003447\,T^2, \tag{4.3}$$

$$\lambda(T) = -0.6958 + 0.007042\,T - 0.00000896\,T^2. \tag{4.4}$$

In equations (4.1) to (4.4) $\rho$ is density, $C_p$ - specific heat at constant pressure, $\mu$ - dynamic viscosity, $\lambda$ - thermal conductivity and $T$ is temperature given in $[K]$. Figure 4.8 shows agreement between polynomials and data from the literature.

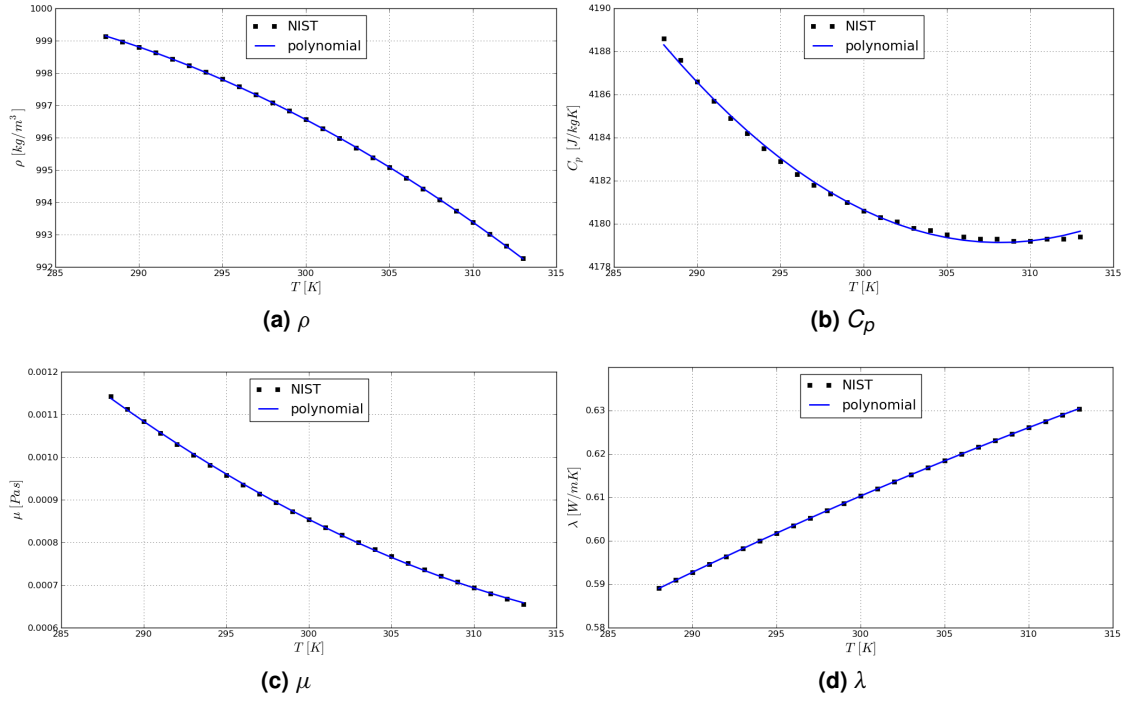


**(a)** $\rho$ **(b)** $C_p$

**(c)** $\mu$ **(d)** $\lambda$

**Fig. 4.8:** Fluid properties.

**SGS model for velocity** The dynamic one-equation model, given in Sect. 2.4, is used for the velocity field. As it was mentioned before, the modeled transport equation for the SGS kinetic energy is solved and SGS diffusivity is determined by following relation:

$$\nu_{sgs} = c_k \Delta \sqrt{k}, \tag{4.5}$$

where $c_k$ is the model coefficient calculated dynamically. $\Delta$ is characteristic length and it is calculated as a cube root of a cell volume: $\Delta = \sqrt[3]{\Delta_x \Delta_y \Delta_z}$.

In addition, in order to reduce characteristic length scale, $\Delta$, in the near wall region, van Driest damping function is applied. This was necessary because the mesh resolution in the near-wall region is not sufficient to resolve the viscous sublayer, and any further mesh refinement would significantly increase computational cost. In OpenFOAM, van Driest damping function is given as follows:

$$\Delta = min\left(y\frac{\kappa}{C}\left[1 - exp\left(-\frac{y^+}{A^+}\right)\right], \sqrt[3]{V}\right), \tag{4.6}$$

where $\kappa$, $C$ and $A^+$ are usually set to $0.41$, $0.158$ and $26$ respectively and $V$ is a cell volume.

**SGS model for temperature** Three models based on the standard gradient diffusion hypothesis are used to close the temperature equation and they differ in the treatment of subgrid-scale turbulent Prandtl number. The first one is the standard, constant $Pr_{sgs}$, model with the value for $Pr_{sgs}$ set to $0.9$.

In the second model, S2, which is proposed by Otic [81], $Pr_{sgs}$ depends on temperature and molecular fluid properties. In this model, $Pr_{sgs}$ is calculated from Eq. (2.143):

$$Pr_{sgs} = \frac{\nu_{sgs}}{\kappa_{sgs}} = \left(\left(\frac{4\alpha}{\beta}\right)^{1/2} Pr^{4/9}\right)^{-1}.$$

The third model, used in S3, is the volume-averaged version of the dynamic model for $Pr_{sgs}$, which is derived in Sect. 3.1. $Pr_{sgs}$ is determined by the Eq. (3.20). All models are listed in Table 4.3. Results and discussion follow in the succeeding section.

**Tab. 4.3:** Models for subgrid-scale heat flux.

| Simulation | SGS heat flux | $Pr_{sgs}$ |
|---|---|---|
| S1 | SGD | 0.9 |
| S2 | SGD | $f(T)$ |
| S3 | SGD | dynamic |

### 4.2.4 Results

Before analyzing the results, it would be useful to point out the measuring locations. It is reported in [99] that velocities were measured at $x = 1.6D_2$, $2.6D_2$, $3.6D_2$ and $4.6D_2$ along two lines perpendicular to the flow: horizontal ($-70\,mm < y < 70\,mm$) and vertical ($-70\,mm < z < 70\,mm$), but, in the same document, just the measurements at two locations ($x = 1.6$ and $4.6$) were provided. For temperature measurements, thermo couples were placed at $x = 2D_2$, $4D_2$, $6D_2$, $8D_2$, $10D_2$, $15D_2$ and $20D_2$. The computational domain used for this validation is just a little longer than $8D_2$, see Fig. 4.6, hence the measurements at

$x = 10D_2$, $15D_2$ and $20D_2$ are not considered. For both velocity and temperature, mean and rms values are provided. Reported uncertainties were $6-8\%$ for velocity and $8-13\%$ for $T_{rms}$. For the mean temperature, a constant uncertainty of $0.03$ in terms of the normalized temperature ($T^*$) is given. Normalized temperature is defined as:

$$T^* = \frac{(T - T_{cold})}{\Delta T}, \tag{4.7}$$

where $\Delta T = T_{hot} - T_{cold}$.

Results are compared with the experimental measurements and with the results from the T-junction benchmark which are available in [99, 100]. Results published by other researchers can be found in, e.g. [27, 38, 47, 52, 78].

### Velocity

Prior to the comparison of different models for SGS heat flux, it is necessary to reproduce the velocity field as close as possible to the experimental measurements. Figure 4.9 shows the instantaneous and time-average velocity distribution for case S3. Apparent visual differences of instantaneous velocity field between simulations were not observed.

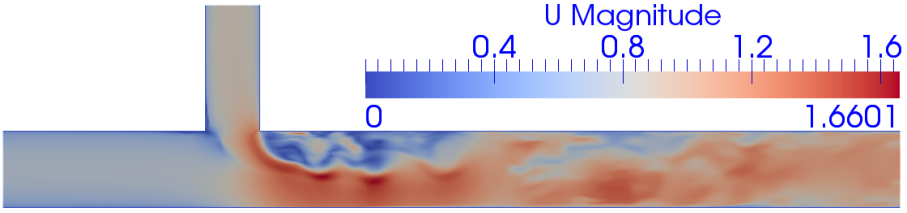


**(a)** Instantaneous

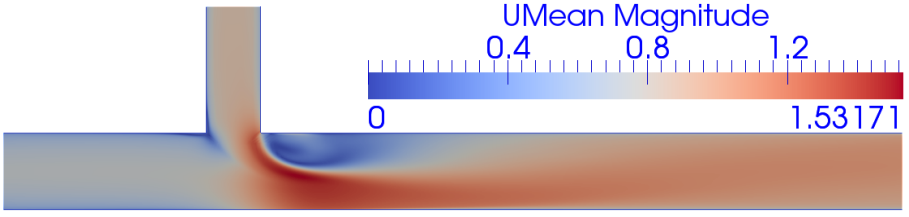


**(b)** Mean

**Fig. 4.9:** Velocity field for S3 case.

At the first look, a region of recirculation fluid can be observed immediately after the branch pipe. It emerges as a consequence of the hot stream intrusion and spans to $2-3D_2$ in the main flow direction. Directly under this region, is the region with highest velocities, with the highest peeks up to $1.6\frac{m}{s}$, which is about $65\%$ above the bulk velocity. Starting from about $3D_2$, flow slowly becomes recovered and towards the end of the computational domain it looks like fully developed pipe flow. Furthermore, in one of the previous reports, Frank et al. [27] observed a so-called horseshoe vortex structure forming upstream from the center of T-junction and the same structures are found in our simulation.

In Figures 4.10 and 4.11, velocity is compared with the experimental measurements and with the results from benchmark simulations published in [99]. For data comparison, two benchmark simulations are chosen: BS1 is a high-resolution LES simulation ($70.5$ million cells) which showed the best agreement to the experiment, and BS2, which showed also very good agreement while the mesh size was much closer to the present setup: $5.8$ million cells. Details of these simulations are given in Table 4.4.

**Tab. 4.4:** Benchmark simulations chosen for comparison.

| Simulation | Code | Turbulence | Mesh |
|---|---|---|---|
| BS1 | Fluent | LES, Dyn. Smagorinsky | 70.5M |
| BS2 | Fluent 6.3.26 | LES, Dyn. Smagorinsky | 5.8M |

Tim averaged values are provided by the experiment, hence it was necessary to average velocity and temperature fields for long enough time prior to the data comparison. After an initial flow development period, which took between $4$ and $5s$, results are averaged in the next $20s$ of physical time. This averaging time was long enough for mean velocity and temperature to reach smooth and symmetric profiles, however it was still insufficient for rms values. The overall rate of change of the rms profiles was too slow to make any further extension of the simulation time reasonable. The time averaged velocity at $x = 1.6D_2$ is shown in Fig. 4.10 and 4.11. The mean velocity is normalized by the bulk velocity, $u_{bulk} = 0.97\frac{m}{s}$. Even though results for $z = 0$ overpredict measurements, overall good agreement is achieved. Small differences

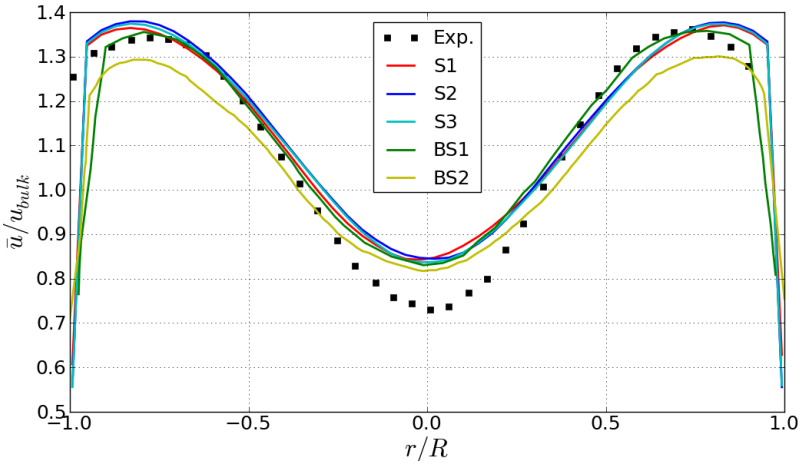


**Fig. 4.10:** Mean velocity at $x = 1.6D_2$ and $z = 0$.

between S1 and S2 and S3 are visible and this is caused by the different fluid properties: constant fluid properties are used in S1, while temperature dependen fluid properties (see equations (4.1) to (4.4)) are used in S2 and S3. Differences between S2 and S3 are probably caused by the small differences in temperature fields. Furthermore, its is shown that mean velocity field can be reproduced with much coarser mesh than the meshes used in benchmark

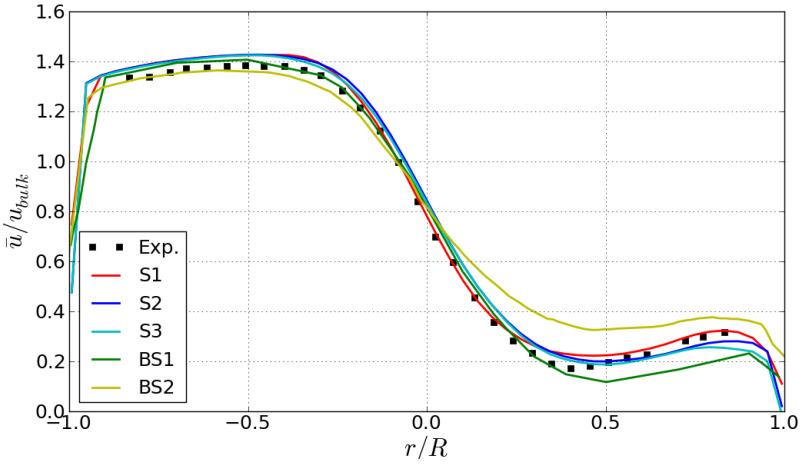


**Fig. 4.11:** Mean velocity at $x = 1.6D_2$ and $y = 0$.

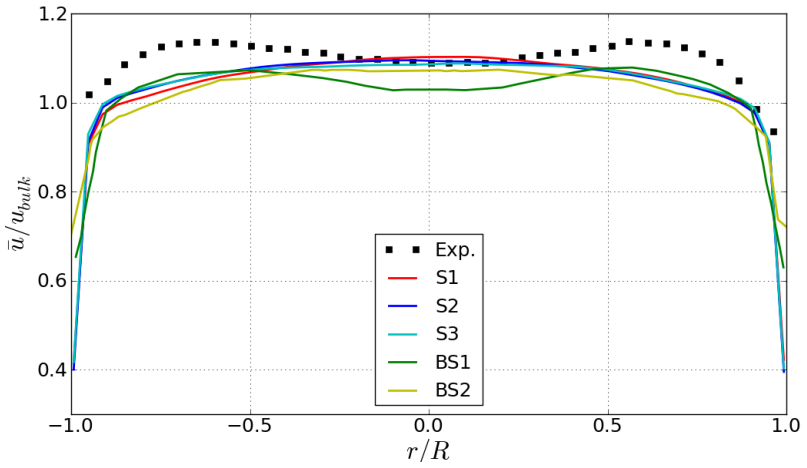


**Fig. 4.12:** Mean velocity at $x = 4.6D_2$ and $z = 0$.

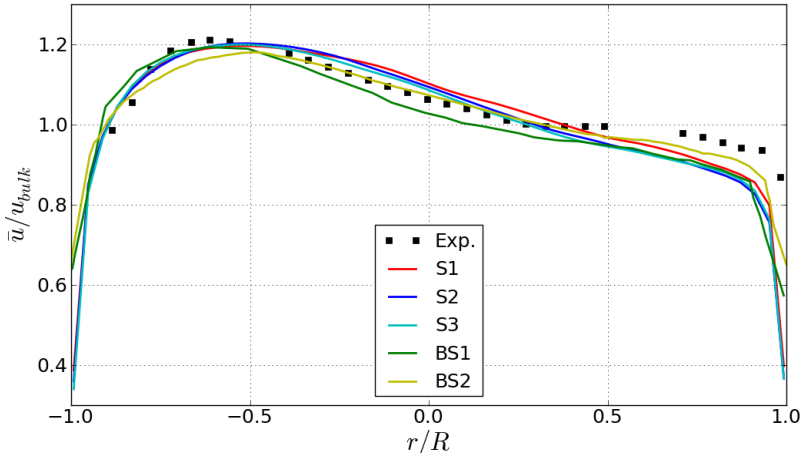


**Fig. 4.13:** Mean velocity at $x = 4.6D_2$ and $y = 0$.

tests.

Figures 4.12 and 4.13 show normalized time averaged velocities at $x = 4.6$. Again, overall good agreement with the experiment is obtained. From figures 4.10 to 4.13 it can bee seen how the flow field recovers from the intrusion of hot water from the branch pipe. RMS values of velocity fluctuations are given in Fig. 4.14. Nevertheless that small underprediction can be observed, overall agreement is satisfying.

From figures 4.10 to 4.14 it can be conclude that mean velocity correlates well with the experimental results and, even more, at some measuring locations agreement is better than for the benchmark simulations BS1 and BS2.

### Temperature

Temperatures are compared in non-dimensional form given by Eq. (4.7). This kind of comparison was necessary since, as it was reported in [99], it was difficult to keep constant fluid temperatures at the measuring locations upstream from the center of T-junction. Thermocouples are placed at four streamwise locations around the pipe wall, defined at the beginning of this subsection, taking $0°$ to be the top wall of the main pipe ($y = 0$, $z = 70\,[mm]$) and $90°$ bottom wall ($y = 0$, $z = -70\,[mm]$).

Fig. 4.15 (a) to (i) shows development of temperature field for S3 case. Numerical

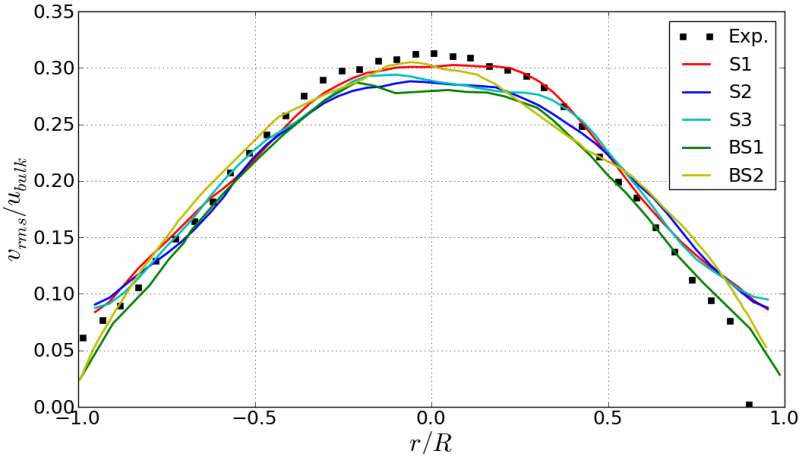


**Fig. 4.14:** RMS of velocity fluctuations at $x = 1.6D_2$ and $z = 0$.

schlieren technique, given by relation (4.8), is applied to instantaneous temperature field in order to expose even the smallest non-uniformities in temperature field:

$$\theta_S = \beta exp\left(-\frac{\kappa\nabla|\theta|}{|\theta|_{max}}\right), \tag{4.8}$$

where $\beta$ and $\kappa$ are adjustable parameters and subscript *max* denotes maximum value over the whole domain. Further details on numerical schlieren, as well as some other visualization techniques can be found in [37] or [67]. Fig. 4.15 (a) shows the cross-section at $50\,[mm]$ from the center of T-junction, after intrusion of hot stream. A clear, sharp border separates cold and hot stream and it extends within the upper half of the main pipe. At the pipe walls, hot stream goes further toward the bottom wall, but this protrusion of hot fluid is limited to the thin layer in the wall vicinity. In figures (b) and (c), the clear border between two streams is still visible but now it extends to the bottom half of the pipe. Turbulent structures can be observed in the upper half of the pipe surrounded by the mixing front, while the lower half remains almost without any indication of turbulence. As a result of interaction between turbulent structures (turbulent mixing) emerging in the upper part, the mixing front is smeared and in Fig (d) it cannot be distinguished even though the flow field is still separated. Following recovery of the flow field, beginning from the $x = 4D_2$ turbulent mixing takes part in the whole flow field and this can be observed in figures (e) to (h). About $x = 8D_2$, fig (i), temperature field has properties of fully developed turbulent pipe flow. At the end, it should be mentioned that this analyses is for instantaneous temperature field obtained from the S3 case. Other two test cases produce more or less same development of temperature field (in visual sense).

Normalized mean temperatures and rms of temperature fluctuations are shown in Fig. 4.16 from (a) to (h). Results are compared with the experimental measurements and with the benchmark test BS1. The second benchmark test, BS2, is not available in [99] since it did not enter top five scores for temperature. Fig. (a) shows the normalized mean temperature, $\bar{T}^*$, at the top wall. All three tested models gave better prediction at $x = 2D_2$, while temperature at $x = 8D_2$ is overpredicted. Models S2 and S3 give almost the same trend for temperature curve. In Fig. (e), normalized mean temperature at bottom wall, $\phi = 180°$, is shown. All three models underpredict wall temperature but the overall trend is reproduced. The temperature obtained from S2 is closer to the experimental measurements than temperatures produced by two other models. Case S3, which uses the dynamic model for subgrid-scale turbulent Prandtl number, showed improvement compared to the standard model with constant $Pr_{sgs}$, but it fails to reach results of S2. This is probably caused by the fact that S3 uses "global" version of dynamic $Pr_{sgs}$ - it is averaged over the whole computational domain and it fails to account for the local variations of velocity and temperature. Figures (c) and (g) show results

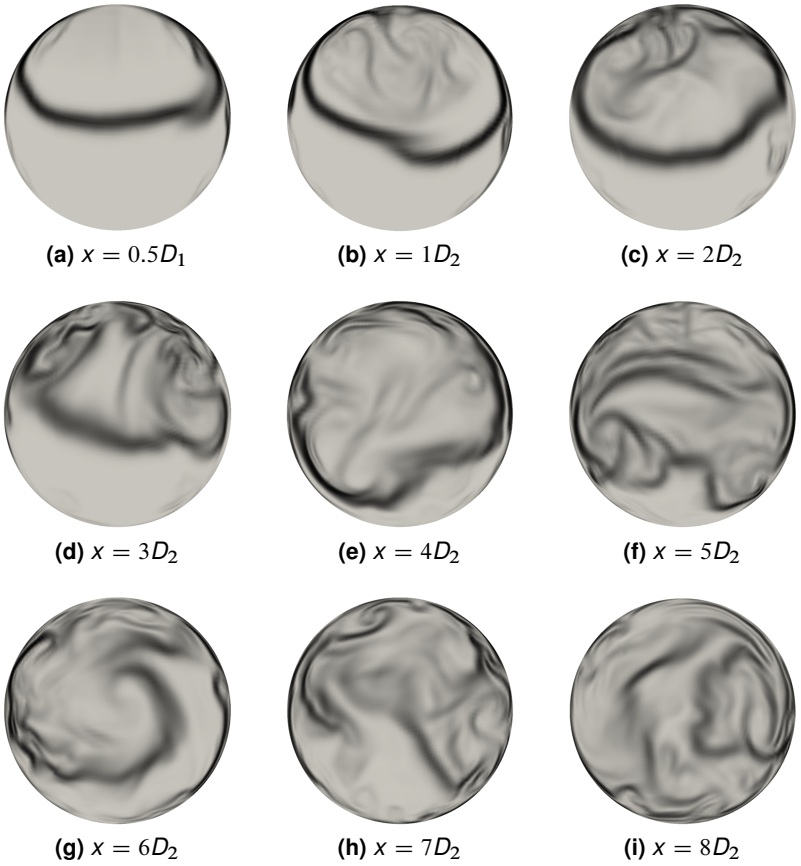

**(a)** $x = 0.5D_1$ **(b)** $x = 1D_2$ **(c)** $x = 2D_2$

**(d)** $x = 3D_2$ **(e)** $x = 4D_2$ **(f)** $x = 5D_2$

**(g)** $x = 6D_2$ **(h)** $x = 7D_2$ **(i)** $x = 8D_2$

**Fig. 4.15:** Numerical schlieren of temperature for S3 case obtained by using Eq. (4.8) with $\beta = 0.8$ and $\kappa = 15$. Darker regions represent higher temperature gradients.

for left, $\phi = 90°$, and for the right main pipe wall, $\phi = 270°$. Same as for the top wall, results at $x = 2D_2$ are closer to the experimental than the results at $x = 8D_2$ where overprediction exists. For side walls, S3 produces slightly better results than S2. It is worth noting that the experimental results show a small asymmetry which can be seen at $x = 4D_2$ and this should be addressed to the difficulties in keeping the thermal boundary conditions constant. From the comparison of normalized mean temperatures follows that all three models, S1, S2 and S3 are able to give good prediction for temperature field even with a mesh which contains much less computational volumes than the mesh used in benchmark simulation BS1.

RMS values of temperature fluctuations at the pipe wall are given in Fig. 4.16: (b), (d), (f) and (h). At the first look it can be seen that averaging time of $20s$ is not long enough because the curves still contain some fluctuations. For further averaging, more than $25s$, overall changes in rms values were too small and it would take a long time before getting completely smooth curves. Fig. (b) shows rms values at the top wall, $\phi = 0°$. As opposed to the normalized mean temperature, simulation results at $x = 8D_2$ showed better agreement to the experiment than the results at $x = 2D_2$. All three models slightly overpredict the experiment, but the overall trend reproduces the measurements. S1 gave slightly better results than S2 and S3 which are almost the same. $T^*_{rms}$ at the bottom wall, $\phi = 0°$, is given in (f). Same as for the normalized mean temperatures at the same position, S2 gave the best results. This can be addressed to the temperature dependent $Pr_{sgs}$ which takes the local value at each computational volume. Again, S3 fails to give better prediction, probably because of the volume averaging which is implemented in the model. Figures (d) and (h) show $T^*_{rms}$ at side walls of the pipe: left, $\phi = 90°$ and right, $\phi = 270°$. S2 and S3 produced almost the same results and both of the models show good agreement with the experiment, while S1

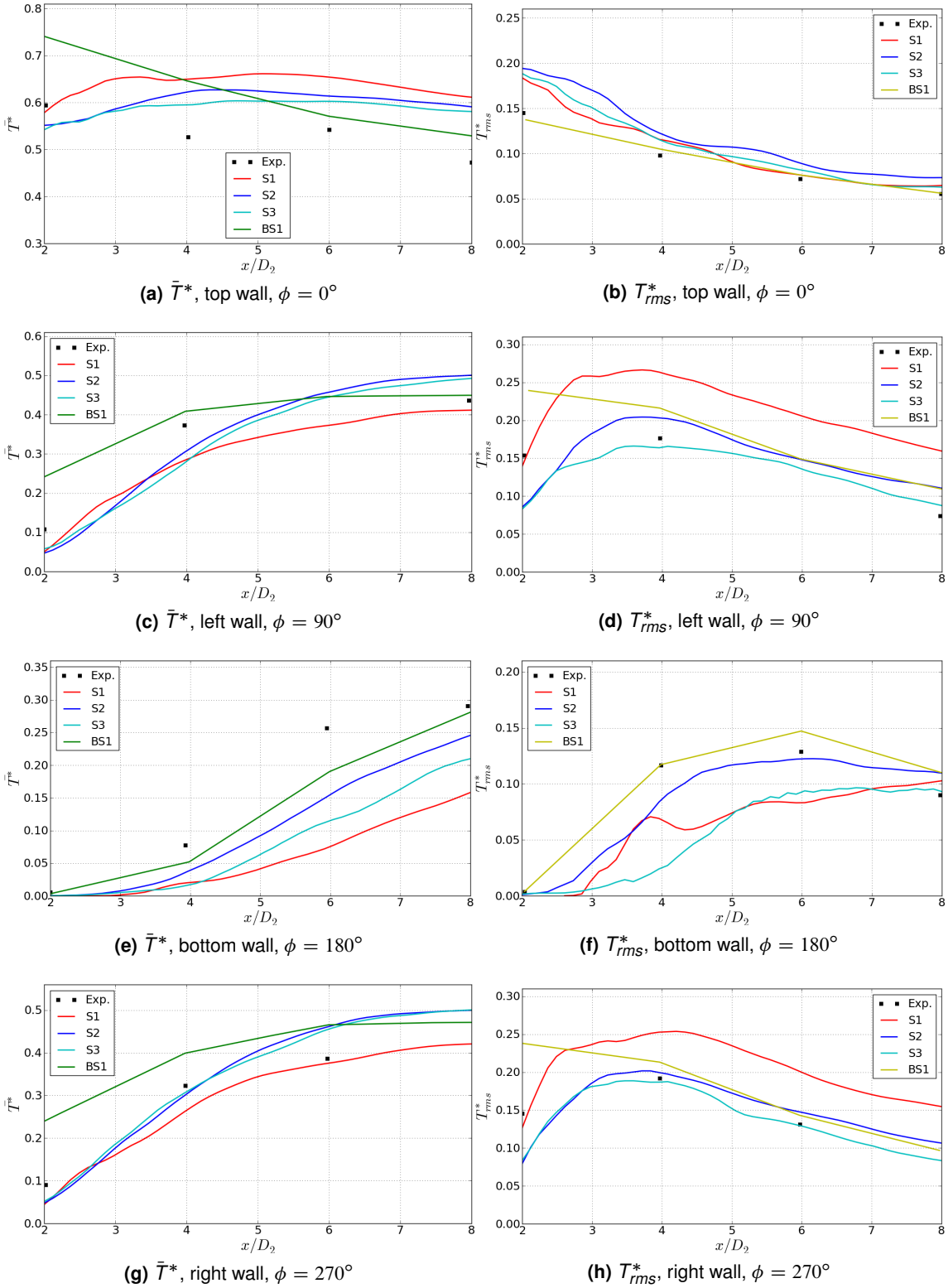


**(a)** $\bar{T}^*$, top wall, $\phi = 0°$

**(b)** $T^*_{rms}$, top wall, $\phi = 0°$

**(c)** $\bar{T}^*$, left wall, $\phi = 90°$

**(d)** $T^*_{rms}$, left wall, $\phi = 90°$

**(e)** $\bar{T}^*$, bottom wall, $\phi = 180°$

**(f)** $T^*_{rms}$, bottom wall, $\phi = 180°$

**(g)** $\bar{T}^*$, right wall, $\phi = 270°$

**(h)** $T^*_{rms}$, right wall, $\phi = 270°$

**Fig. 4.16:** Normalized mean temperature and RMS values of temperature fluctuations at the wall.

overpredicts the measurements. By comparing these results, it can be concluded that $Pr_{sgs}$ significantly influences results in the bottom part of the main pipe, which can be observed in (f), while the effects in the upper region are smaller. Hence, when simulating the turbulent heat transfer in flows where molecular Prandtl number significantly differs from 1, as it was the case in this experiment, some kind of modeling for $Pr_{sgs}$ definitely has to be considered.

Normalized mean temperatures over the cross sections at $x = 1.6D_2$ and $4.6D_2$ are given in Fig. 4.17, (a) to (d). Unfortunately, there are no available experimental measurements and it is possible to compare different models just between each other. The general characteristic observed here is that the models used in S2 and S3 produce almost similar mean temperature profiles. On the other hand S1, which uses constant fluid properties, gives somewhat different profiles and this difference is increasing with the $x$ coordinate.

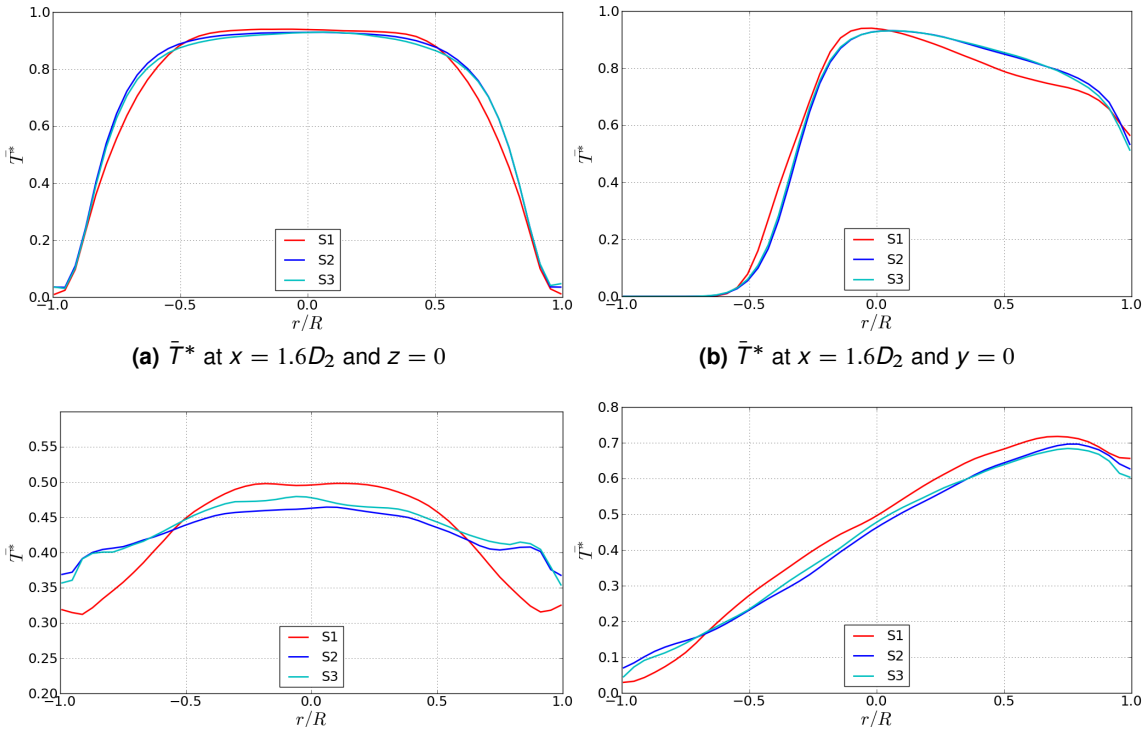


**(a)** $\bar{T}^*$ at $x = 1.6D_2$ and $z = 0$

**(b)** $\bar{T}^*$ at $x = 1.6D_2$ and $y = 0$

**(c)** $\bar{T}^*$ at $x = 4.6D_2$ and $z = 0$

**(d)** $\bar{T}^*$ at $x = 4.6D_2$ and $y = 0$

**Fig. 4.17:** Normalized mean temperature over the cross sections.

Bearing in mind the mesh resolution used in present simulations, a satisfactory agreement with the experimental measurements is achieved. Models based on variable subgrid-scale turbulent Prandtl number, S2 and S3, show better performance, especially for the rms values. Furthermore, S2 gives better results for the bottom wall than other two models and this is the consequence of locally dependent $Pr_{sgs}$ which is able to adjust its value depending on the local fluid temperature.

Since the main purpose of this test case was to validate the dynamic modeling approach, the primary interest is in S3 case. Results are in satisfactory good agreement with the experiment and improvement over the standard model which uses a constant value for $Pr_{sgs}$ is achieved. However, the most important conclusion is that the dynamic procedure is able to give good prediction for $Pr_{sgs}$ in the conditions of turbulent mixing at high Reynolds numbers and, at the same time, it showed stable behavior. This means that the dynamic procedure is suitable for further application to calculate model coefficients in other models for SGS heat flux.

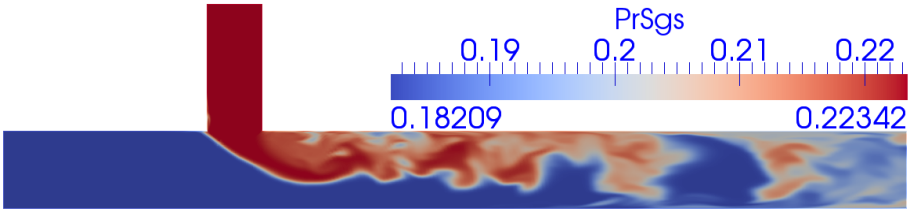


**Fig. 4.18:** Local distribution of $Pr_{sgs}$.

**Subgrid-scale turbulent Prandtl number, $Pr_{sgs}$**

Figure 4.18 shows the distribution of temperature dependent $Pr_{sgs}$ which is used in S2. It is calculated from Eq. (2.143), which is solved for each computational volume so that the $Pr_{sgs}$ has local distribution. It can be seen that higher values correspond to the higher fluid temperatures or lower molecular Prandtl numbers ($Pr$ of water decreases with the temperature increase). Calculated values are in the range between $0.18209$ and $0.22342$ and this range is fixed because of the constant inlet temperatures. The difference of $0.04$ between minimal and maximal value is not big, but, the difference between cold and hot stream, $\Delta T$, is only $19°C$. It is expected that for higher $\Delta T$, the temperature dependent $Pr_{sgs}$ model will further improve results in regard to the models based on constant $Pr_{sgs}$.

The dynamic model, which is applied in S3, calculates $Pr_{sgs}$ at each time step as simulation progresses and, as it was already mentioned, it is assumed that $Pr_{sgs}$ takes one single value for the whole computational domain. The progress of dynamic $Pr_{sgs}$ for the first five seconds of physical time is shown in Fig. 4.19. The time step used in the simulation was $\Delta t = 0.0001\,[s]$, which kept the maximal Courant number under 0.5. It can be seen that first $1-1.5\,[s]$ of physical time (first 10000 - 15000 time steps) is characterized by strong variations of $Pr_{sgs}$ value with both positive and negative peeks. At the beginning of the simulation, $Pr_{sgs}$ is very low, just above zero. This was expected because internal fields for velocity and temperature were uniform (zero-gradient). The highest negative peek, $Pr_{sgs} = -2.36648$, occurs at $t = 0.0033\,[s]$. This is probably caused by the negative value of model coefficient $c_k$, which could be an indication of backscatter of energy. However, this high negative peek appears at just on time step while the values around it are about ten orders of magnitude higher. Initial period of simulation lasts until $t \approx 0.1\,[s]$ whereupon $Pr_{sgs}$ starts to increase monotonically. At about $t \approx 0.27 - 0.28\,[s]$, which corresponds to the beginning of intrusion of hot fluid into the main stream (the centerline velocity in the hot pipe is $u_{cl} \approx 0.865\,[m/s]$), as a consequence of intense mixing $Pr_{sgs}$ starts to increase sharply and at $t = 0.3413\,[s]$ the highest value is reached: $Pr_{sgs} = 5.41579$. After the highest peek is reached, $Pr_{sgs}$ decreases very fast until a stable value of about $Pr_{sgs} \approx 0.3 - 0.35$ at $t \approx 0.5\,[s]$. This part of the simulation, intrusion of the hot fluid, is the most critical one and high time steps can lead to divergence of the solution. Since the temperature of internal field was set at the same value as the temperature of cold stream, $19°[C]$, collision of two streams, which occurs at $t \approx 0.7\,[s]$ does not produce strong variations of $Pr_{sgs}$. Instead of that, $Pr_{sgs}$ slowly increases for another second of physical time and after $t \approx 2\,[s]$ a stable region is reached. In this region $Pr_{sgs}$ oscillates around mean value $\bar{Pr}_{sgs} = 0.65$, which is obtained by averaging $Pr_{sgs}$ over the first five seconds. It has to be mentioned that the beginning of the stable region at $t = 2\,[s]$ agrees to the time suggested in [99]: $t = 2 - 4\,[s]$. At $t = 5\,[s]$ averaging of the velocity and temperature fields is started.

At the end of $Pr_{sgs}$ analyses, one further stability detail has to be mentioned. If the difference between hot and cold stream were higher than $\Delta T = 19\,[°C]$, the maximal $Pr_{sgs}$ would be higher than the value observed in this test case. Higher peeks means that some kind of clipping of very high (or very low) $Pr_{sgs}$ values might be necessary in order to stabilize the calculation. Since the region with strong and irregular oscillations of $Pr_{sgs}$ is usually limited to

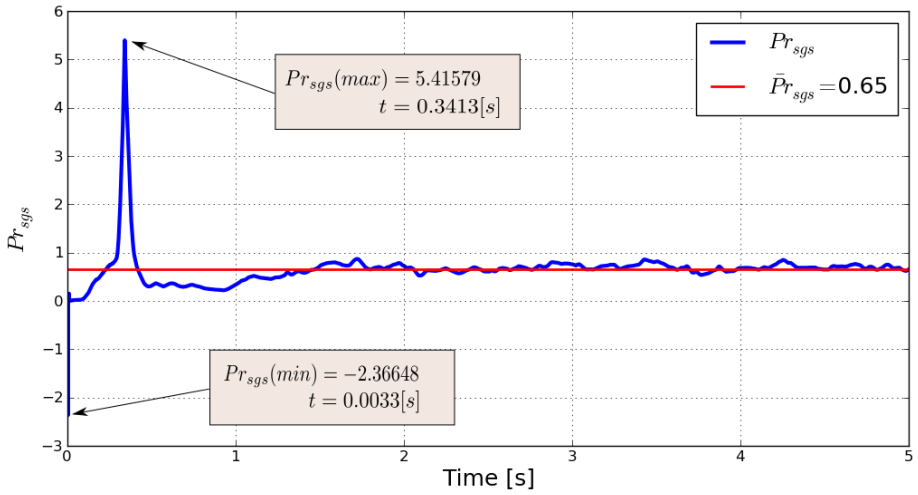


**Fig. 4.19:** $Pr_{sgs}$ in the first 5 seconds of physical time.

a short period of time with just occasional very low or very high peeks, clipping of $Pr_{sgs}$ values appears to be an attractive solution because it is very simple to implement and fundamental advantages of dynamic procedure are not affected.

### 4.2.5 Discussion

The aim of the T-junction test case was to validate the dynamic procedure which is applied in the dynamic model for $Pr_{sgs}$. The validation is done by comparing the results for velocity and temperature with the experimental measurements, results from other simulations available in the literature and with the results obtained by using standard models, case S1, or by using other models for $Pr_{sgs}$, case S2.

The dynamic one equation model for momentum equation is applied in all three cases. The only difference was that in S1 constant fluid properties are used while in S2 and S3 fluid properties depend on temperature. Since the inlet Reynolds numbers were $Re_c = 79400$ and $Re_h = 107000$, while the temperature difference between two streams was $\Delta T = 19\,[°C]$, the test case is forced convection. This means that different models for $Pr_{sgs}$ have minimal influence on the velocity field, hence difference in velocity results is mainly caused by different treatment of fluid properties: constant or polynomial. Following conclusions can be drawn from velocity comparison:

- Overall good agreement to the experimental measurements and results from the literature, for both mean and rms values is achieved.
- The dynamic model for momentum equation combined with the van Driest damping in the wall vicinity gives good results even if applied on the meshes with lower resolutions.

Same as for the velocity, the temperature validation is done by comparing the mean and rms values at the wall with the results from the experiment and literature. In every simulation a different treatment of $Pr_{sgs}$ is used: constant $Pr_{sgs}$ is used in S1, temperature dependent $Pr_{sgs}$ in S2 and newly formulated dynamic model for $Pr_{sgs}$ in S3. Following the temperature comparison, the following can be concluded:

- The overall agreement to the existing results is worse than the agreement obtained for the velocity field. This can be explained by the fact that, since the spectra of temperature field decays slower than velocity field spectra (at the temperatures used in this

experiment Prandtl number of water is around 7), mesh requirements for temperature are higher than for the velocity.

- Results for the side walls ($\phi = 90°$ and $\phi = 270°$) are better than results for top wall ($\phi = 0°$). S2 and S3 give very good qualitative agreement for rms values to the experiment, but both models underpredict value at $x = 2D_2$.
- S2 gives better results for the bottom wall than the other two models, while S3 is better than S1. Since the only difference between S2 and S3 is in $Pr_{sgs}$, it follows that modeling of $Pr_{sgs}$ is of high importance. In S3 $Pr_{sgs}$ does not vary spatially and this is a disadvantage over S2.
- Wall mean temperatures and rms values predicted by S3 are in reasonable good agreement with the experimental data.
- The dynamic model for $Pr_{sgs}$ is stable despite the strong flow unsteadiness caused by intrusion of hot fluid.
- The local dynamic model for $Pr_{sgs}$ can be applied but it requires some arbitrary clipping of very high or very low values.

At the end, it can be concluded that the dynamic model for $Pr_{sgs}$ is successfully validated. This gives the basis for further utilization of the dynamic procedure: to calculate model coefficients for the dynamic subgrid-scale heat flux model which is derived in 3.2.

## 4.3 Turbulent mixed convection

The new dynamic model for subgrid-scale heat flux is validated in this section. For the validation purpose chosen is an experiment, where the aiding flow of water along a vertical flat plate is investigated, Kitamura and Inagaki [55]. The experiment was performed in the region of high Rayleigh and Reynolds numbers and provides both mean and root mean square values of velocity and temperature for different inlet and boundary conditions.

Beside the experiment selected for our validation purpose, a number of other experiments or direct numerical simulations exists in the literature, some of whom are listed in Tab. 1.1. Experiments and DNSs listed here cover a large range of Reynolds and Grashof numbers and build up a large database for further validation of the model.

### 4.3.1 Test facility

A schematic illustration of the experimental facility is shown in Fig. 4.20. A flow of water is forced through a vertical, rectangular duct of $0.3 \times 0.3\,m^2$ cross section area and of $3.6\,m$ height. A uniform, vertical flow of maximum turbulent intensity level less than $3\,\%$ was provided to the duct inlet. One wall was heated by a uniform wall heat flux which ranged between $1000\,W/m^2$ and $7800\,W/m^2$, depending on the experimental setup. The heat lost by conduction through the heating plate and by the radiation from the heating plate was estimated to be less than $3.5\,\%$. The temperature of the main stream was in the range from $26°C$ to $28°C$ while the measured temperature of the heated surface was between $30°C$ and $46°C$, depending on the wall heat flux. Inlet velocity and wall heat flux were varied to obtain different experimental conditions which are given in Tab. 4.5. The inlet temperature was $27°C$ for all experimental configurations. Further details about the experiment are given in [55]. Values in

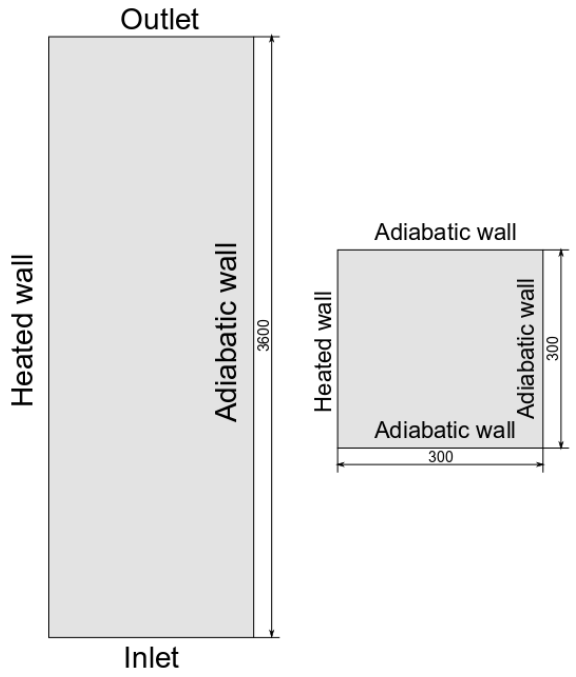


**Fig. 4.20:** Schematic of the test facility.

**Tab. 4.5:** Experimental conditions.

| Run | Main velocity, $U_\infty\,[cm/s]$ | Wall heat flux, $q_w\,[W/m^2]$ | Reynolds number, $Re_z$ | Grashof number, $Gr_z^*$ | Nusselt number, $Nu_z$ | Non-dimensional parameter $\zeta$ |
|---|---|---|---|---|---|---|
| Q1 | 2.6 | 4000 | $7.30 \times 10^4$ | $9.98 \times 10^{14}$ | 1570 | $4.70 \times 10^{-2}$ |
| Q2 | 4.4 | 4000 | $12.0 \times 10^4$ | $9.89 \times 10^{14}$ | 1470 | $1.30 \times 10^{-2}$ |
| Q3 | 9.6 | 4000 | $24.8 \times 10^4$ | $9.75 \times 10^{14}$ | 1255 | $2.12 \times 10^{-3}$ |
| Q4 | 11.2 | 4000 | $32.2 \times 10^4$ | $10.1 \times 10^{14}$ | 1550 | $8.80 \times 10^{-4}$ |
| U1 | 4.4 | 1000 | $12.0 \times 10^4$ | $2.26 \times 10^{14}$ | 910 | $4.80 \times 10^{-3}$ |
| U2 | 4.4 | 0 | $12.3 \times 10^4$ | 0 | - | 0 |

the table are given at $Z = 3\,m$, where $Z$ represents distance from the inlet in streamwise direction. A non-dimensional parameter which is used by the authors to define the heat transfer regime (forced, natural or mixed convection) is given by the following relation

$$\zeta = \frac{Gr_z^*}{Nu_z Re_z^{2.7}}. \tag{4.9}$$

Regimes of heat transfer depending on the parameter $\zeta$ are given in Tab. 4.6.

**Tab. 4.6:** Regimes of heat transfer.

| Non-dimensional parameter $\zeta$ | Heat transfer regime |
|---|---|
| $\zeta < 4 \times 10^{-4}$ | Forced convection |
| $\zeta > 4 \times 10^{-3}$ | Natural convection |
| $4 \times 10^{-4} < \zeta < 4 \times 10^{-3}$ | Mixed convection |

### 4.3.2 Computational setup

**Experimental configuration** Two experimental configuration, $Q_1$ and $Q_2$ (see Tab. 4.5) were chosen for validation purpose. In both cases, the wall heat flux was $q_w = 4000\,W/m^2$. Inlet velocities were $0.026\,m/s$ in $Q_1$ and $0.044\,m/s$ in $Q_2$. Higher inlet velocity in $Q_2$ increases the influence of forced convection which affects the velocity and temperature profiles near to the wall. All data were reported at the measuring location $Z = 3\,m$ from the inlet.

**Computational mesh** The computational mesh used for the simulations is depicted in Fig. 4.21. The number of cells in $x$, $y$ and $z$ directions are $64$, $30$ and $200$ respectively, while the total number is $384000$. The mesh is refined in the region of heated wall in order to capture the generation of thermal plumes. The mesh is optimized so that minimum $6$ cells lay within the region of $y^+ < 10$, with the first cell being at $y^+ \approx 0.7$.

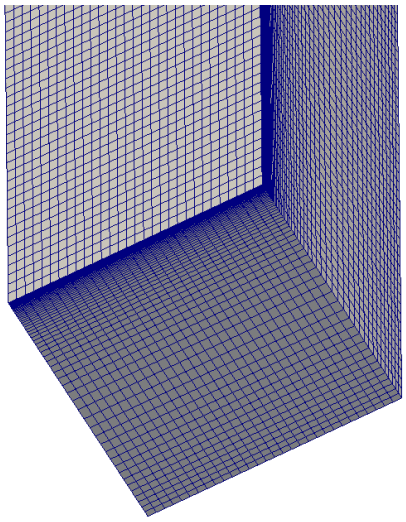

**Fig. 4.21:** Computational mesh.

**Fluid properties** Density, specific heat capacity at constant pressure, dynamic viscosity and thermal conductivity are determined from second order polynomials constructed by interpolating the NIST data, [3], for the temperature range between $25°C$ and $55°C$:

$$\rho = 746.5 + 1.95T - 0.00372T^2, \tag{4.10}$$

$$Cp = 5320 - 7.356T + 0.01186T^2, \tag{4.11}$$

$$\mu = 0.0234 - 0.0001327T + 1.917 \times 10^{-7}T^2, \tag{4.12}$$

$$\lambda = -0.861 + 0.008122 - 1.073 \times 10^{-5}T^2, \tag{4.13}$$

where T is temperature given in $K$. Fig. 4.22 shows agreement between the polynomials (4.10) to (4.13) and NIST data.

**SGS model for velocity** The dynamic one equation model is applied for velocity field. Full description of the model is given in Sec. 2.4.

**SGS model for temperature** Two models are used to close the energy equation. First one is the model based on the standard gradient diffusion hypothesis (SGD) and subgrid-scale turbulent Prandtl number approach. Here, three methods for $Pr_{sgs}$ are used:

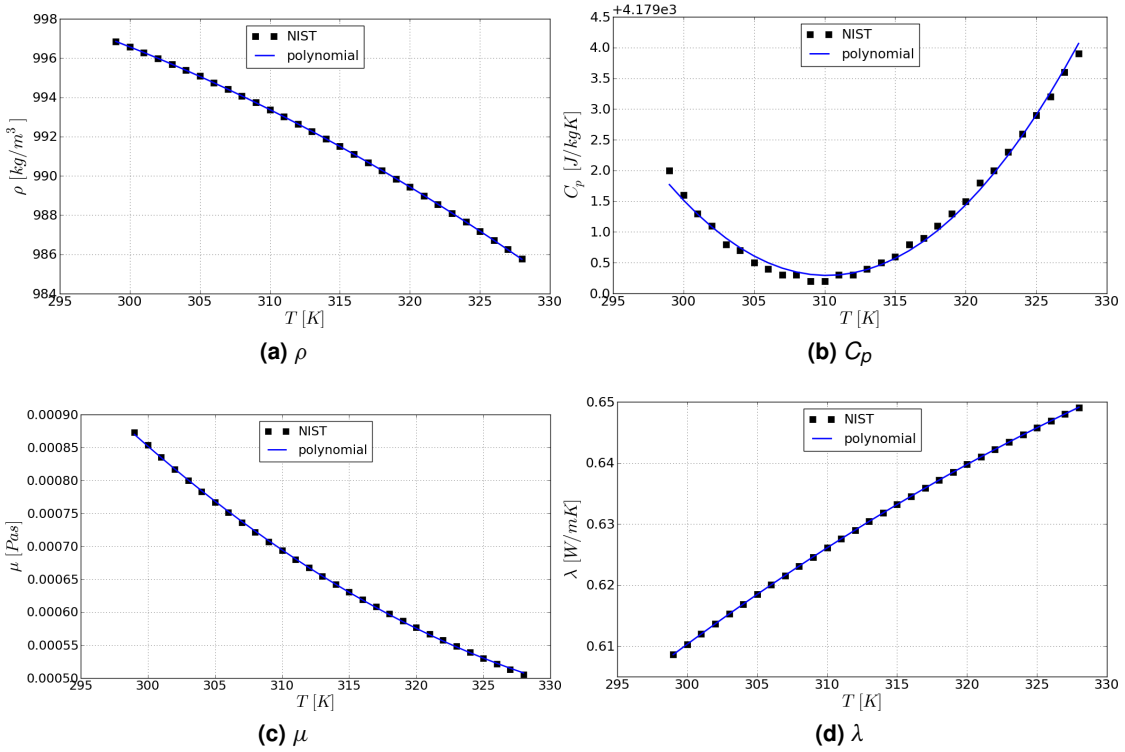


**Fig. 4.22:** Comparison between calculated fluid properties and NIST data.

- Constant $Pr_{sgs}$. Three different values are used $0.1$, $0.9$ and $2$. Those values are chosen because the range of $Pr_{sgs}$ that can be found in the literature is covered by these three values.
- Temperature dependent $Pr_{sgs}$. This model is described in 2.5. In this approach $Pr_{sgs}$ depends on temperature.
- Dynamic $Pr_{sgs}$ - volume averaged. The model is given in 3.1.1. $Pr_{sgs}$ is spatially independent.
- Dynamic $Pr_{sgs}$ - locally dependent. The model is given in 3.1.2. $Pr_{sgs}$ is locally dependent.

The second method to calculate SGS heat flux is the dynamic model which is proposed in 3.2.1. Both approaches to determine model coefficients are tested. The first one, derived in 3.2.3, assumes spatial independent model coefficients, while in the second approach, derived in 3.2.4, model coefficients are locally dependent.

### 4.3.3 Results - Case Q1

In this experimental configuration, the inlet velocity was $0.026\,m/s$ and wall heat flux was $q_w = 4000\,W/m^2$.

Experimental data available for comparison are time average and root mean square values of streamwise velocity component and fluid temperature measured at the streamwise location of $Z = 3\,m$. Velocity and rms values are normalized by the velocity at the duct center, which is almost the same as the main stream velocity (it is reported by the experimentalists that the relative difference between the velocities at two locations $Z = 0$ and $3\,m$ is less than $6\%$ even

**Tab. 4.7:** Models for SGS heat flux.

| Simulation | SGS heat flux | $Pr_{sgs}$ |
|---|---|---|
| LES1 | SGD | 0.1 |
| LES2 | SGD | 0.9 |
| LES3 | SGD | 2 |
| LES4 | SGD | $f(T)$ |
| LES5 | SGD | dynamic - averaged |
| LES6 | SGD | dynamic - local |
| LES7 | dynamic - averaged | - |
| LES8 | dynamic - local | - |

in the most severe cases, so that the velocity at the duct inlet is adopted as the main stream velocity, $U_\infty$). Normalized velocity is given as follows

$$u^* = \frac{u}{u_c}, \tag{4.14}$$

where $u_c$ is the velocity at the duct center.

The temperature is reported in the form of local temperature difference normalized by the difference between the wall and free stream temperature (which is same as the inlet temperature):

$$T^* = \frac{T - T_\infty}{T_w - T_\infty}, \tag{4.15}$$

in which $T_\infty$ is the free stream temperature.

### Velocity

Figure 4.23 shows instantaneous and time-averaged streamwise component of the velocity field obtained form LES7 (see 4.7). Vertical $xz$ plane in the middle of the duct, $y = 0$, between the streamwise distances $z = 1.5$ and $z = 3.2\,m$ is shown. As a consequence of buoyancy force generated by density gradients, thermal plumes are developing at the heated wall which leads to the acceleration of fluid. In the region close to the heated wall, the velocity reaches its highest values which are, on the average, about $100\,\%$ higher than velocities in the middle of the duct.

The streamwise component of the time averaged velocity normalized by the centerline velocity is shown in Fig. 4.24. Same as in the experiment, it is assumed that the velocity in the duct center is equal to the inlet velocity, $u_c = u_{in} = 0.026\,m/s$. Time averaged velocity is calculated by the Eq. (4.16) (see [1])

$$\bar{\phi}^n = \frac{Dt - dt}{Dt}\bar{\phi}^{n-1} + \frac{dt}{Dt}\phi^n, \tag{4.16}$$

where $Dt$ is total elapsed time, $dt$ is current time step and superscripts $n$ and $(n-1)$ represent values at current and previous time steps. It can be seen that $Pr_{sgs}$ strongly affects the velocity field. Lower values (LES1 and LES4) lead to the very high overprediction of the experimental measurements. The results produced by LES1 and LES4 are about $100\,\%$ and $50\,\%$ respectively above the measurements. Simulation results were improved for larger $Pr_{sgs}$ values (LES2 and LES3), however results are still about $20\,\%$ too high.

Simulation results are improved when dynamic models for $Pr_{sgs}$ (LES5 and LES6) and for subgrid-scale heat flux (LES7 and LES8) are used. There was no significant difference among

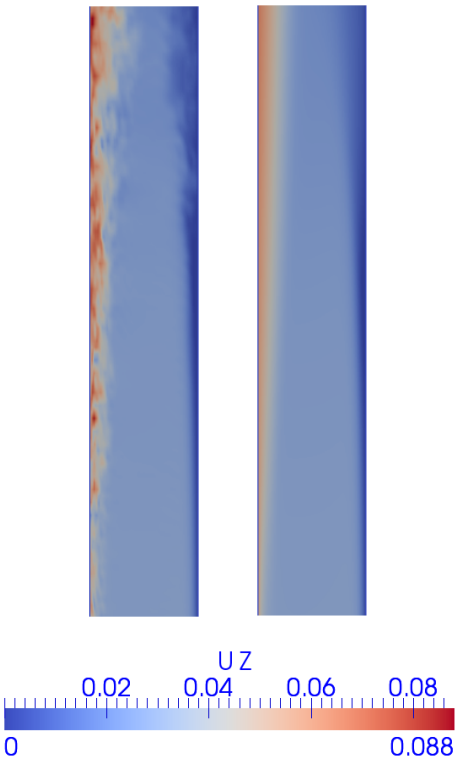


**Fig. 4.23:** Instantaneous and time-averaged streamwise velocity for case Q1.

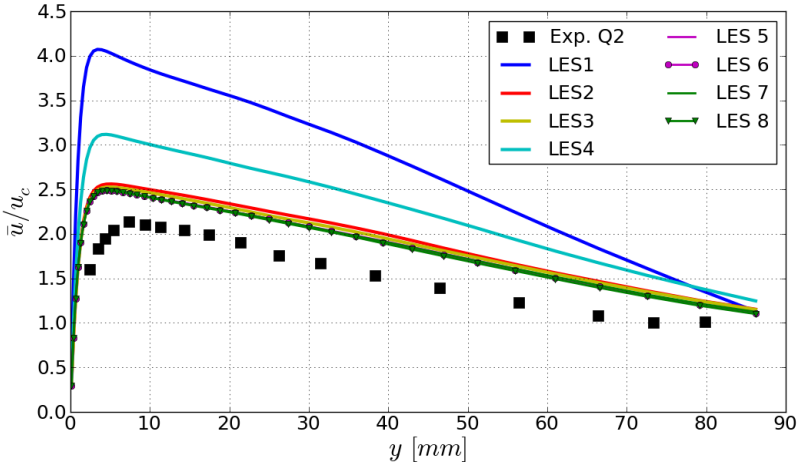


**Fig. 4.24:** Time averaged streamwise velocity.

SGS models and simulation results are about $15\,\%$ above the experimental measurements. Same as in the experiment, the maximal velocity near the heated wall is about $2$ times higher than the velocity in the duct center.

### Temperature

As it was mentioned before, two models, standard gradient diffusion and dynamic subgrid-scale heat flux model, are used to close the energy equation, see Tab. 4.7. The influence of different models on the temperature field is investigated by comparing the dimensionless temperature, Eq. (4.15) with the experimental measurements.

Figure 4.25 shows time averaged temperature distribution in the region close to the heated

wall. Results show the influence of different $Pr_{sgs}$ numbers on temperature field. It can be seen that lowest value for subgrid-scale turbulent Prandtl number $Pr_{sgs} = 0.1$ (LES1) produces smallest temperature gradient and by increasing the $Pr_{sgs}$, temperature gradient becomes larger. This can be explained by larger subgrid scale thermal diffusivity $\kappa_{sgs}$, which is inversely proportional to $Pr_{sgs}$, i.e. lower $Pr_{sgs}$ values give higher $\kappa_{sgs}$:

$$\kappa_{sgs} = \frac{\nu_{sgs}}{Pr_{sgs}}, \tag{4.17}$$

$$\kappa_{eff} = \kappa + \kappa_{sgs}, \tag{4.18}$$

where $\kappa$ is molecular thermal diffusivity. Higher thermal diffusivity better transports heat from the heated wall into the bulk region thereby smearing the temperature gradient.

Correct temperature profile in the wall region can be obtained by adjusting the $Pr_{sgs}$, however, this is a rather arbitrary process and the proper choice for $Pr_{sgs}$ is not known in advance. Moreover, a constant $Pr_{sgs}$ approach will always influence the large scale temperature field even though that a SGS model might be unnecessary (i.e. fine mesh or zero temperature gradient). Model where $Pr_{sgs}$ depends on temperature, LES4, gives better results than LES1.

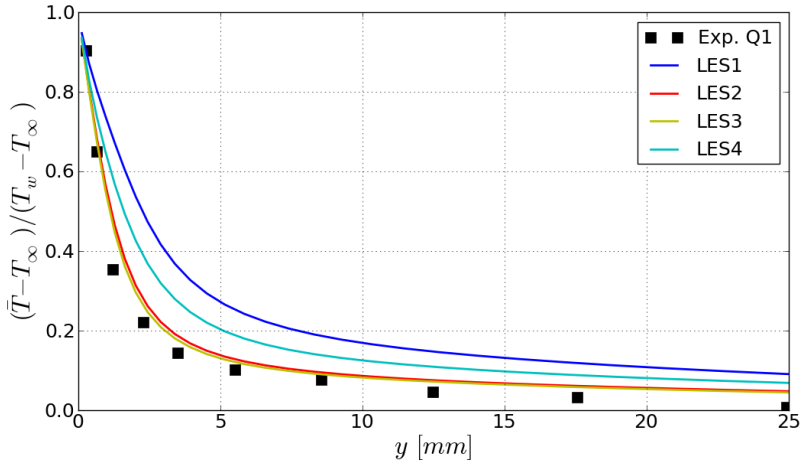


**Fig. 4.25:** Time averaged temperature distribution for cases LES1, LES2, LES3 and LES4.

However, it seams that $Pr_{sgs}$ calculated on this way is still too small which produces smooth temperature gradient. For the present test case, calculated $Pr_{sgs}$ values vary between $0.2$ and $0.25$ which is about four times smaller than a common choice for $Pr_{sgs}$ value, $Pr_{sgs} = 0.9$, which was used in LES2. Even though that results are much closer to the measurements than LES1 and LES2, it can be concluded from the results that a further improvement can be achieved by using larger values for $Pr_{sgs}$. This is shown in LES3. Difference between LES2 and LES3 is very small but it is expected that further increase of $Pr_{sgs}$ would produce results that are even closer to the measurements.

Dynamic models for $Pr_{sgs}$ are used in LES5 and LES6, and the models for subgrid-scale heat flux are applied in LES7 and LES8. Comparison between these models and the one with $Pr_{sgs} = 0.9$ is shown in 4.26. It can be seen that an improvement over the standard model is achieved. However, difference between different dynamic models is very small. This is probably due to the fact that the temperature variations within the water are less than $20°C$. These temperature variations can be observed only in a thermal boundary layer region which is, according to the experiment (see [55]), about $30\ mm$ thick. It is expected that the difference between these models would be higher for the larger variations of fluid temperature. This has to be further investigated for other experiments. All simulations LES5 to LES8 were conducted without any kind of adjustment of the model coefficients.

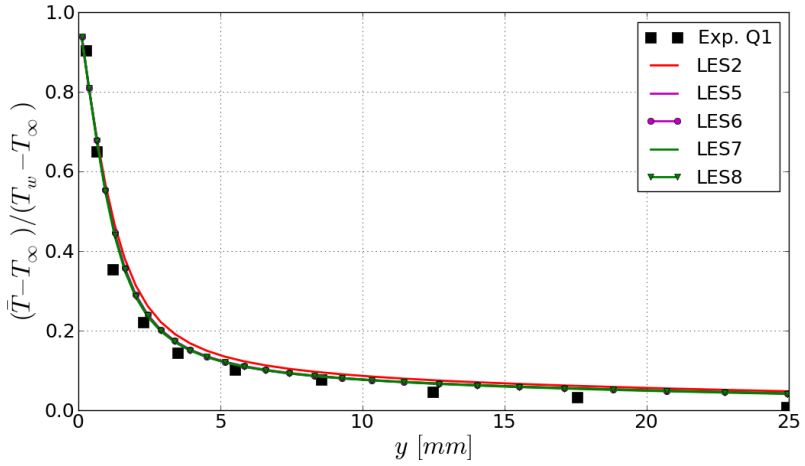


**Fig. 4.26:** Time averaged temperature distribution for cases LES2, LES5, LES6, LES7 and LES8.

The root mean square values of temperature fluctuations are calculated as follows (see [1]):

$$\overline{\phi'^2}^n = \frac{Dt - dt}{Dt}\overline{\phi'^2}^{n-1} + \frac{dt}{Dt}\phi^2 - \bar{\phi}^2, \tag{4.19}$$

$$\phi_{rms} = \sqrt{\overline{\phi'^2}}, \tag{4.20}$$

where $\phi$ is a free variable and represents temperature in this case. Furthermore, $\phi$ can be replaced by any scalar or vector variable.

Figure 4.27 shows temperature rms values for different $Pr_{sgs}$ numbers compared with the experimental measurements. Again, the difference between different $Pr_{sgs}$ numbers is obvious. Differences are particularly highlighted at the wall. Same as for the mean temperature, LES2 ($Pr_{sgs} = 0.9$) and LES3 ($Pr_{sgs} = 2$) produce almost similar results which are lower than measurements. LES1 overpredicts the experiment over the whole thermal boundary layer region. Model with temperature dependent $Pr_{sgs}$ (LES4) overpredicts the measurements in the region close to the wall $x < 3\,mm$. Away from the wall, $x > 3\,mm$, agreement with the experiment is very good.

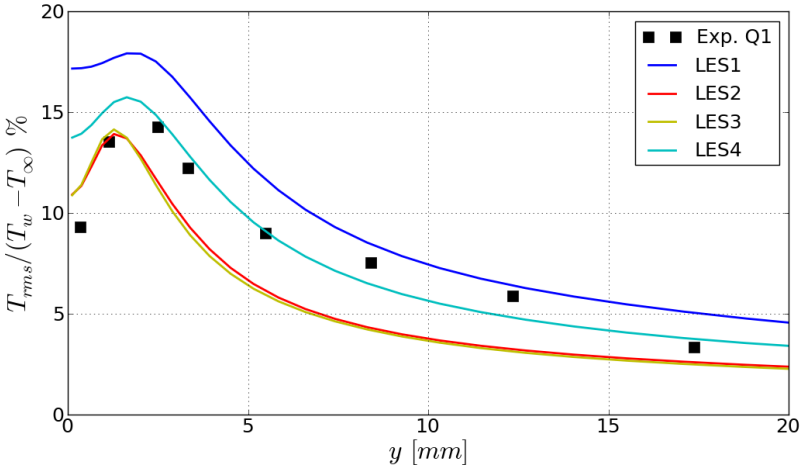


**Fig. 4.27:** RMS of temperature fluctuations for case LES1, LES2, LES3 and LES4.

Dynamic models together with LES2 are shown in Fig. 4.28. Simulation results overpredict the measurements at the wall and underpredict the measurements in the region $3 < x < 20\,[mm]$. Difference between models can be observed only close to the wall, $x < 3\,mm$.

Models LES5, LES7 and LES8 correctly predicts the peak value, which is, however, shifted closer to the wall than in the experiment; $x_{sim} \approx 1.25\,mm$ compared to $x_{exp} \approx 2.5\,mm$. Again, small temperature variations are probably the reason why the dynamic models for $Pr_{sgs}$ and SGS heat flux produce very similar results.

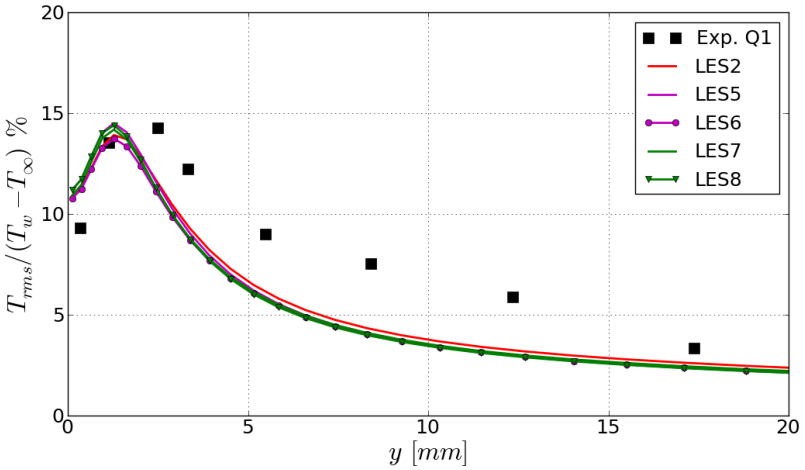


**Fig. 4.28:** RMS of temperature fluctuations for cases LES2, LES5, LES6, LES7 and LES8.

Due to buoyancy force, thermal plumes are developing at the heated wall as can be seen in Fig. 4.29. Six cross sections normal to the flow direction at the streamwise locations $z = 1$, $1.5$, $2$, $2.5$, $3$ and $3.5\,m$ are shown. Again, here is the numerical schlieren technique (see Eq. (4.8)) applied in order to expose even the smallest temperature gradients. Darkest values correspond to the highest temperature gradients. We can see that the temperature gradients exist only in the region near the wall, while in the outer region temperature field stays uniform over the whole duct length. At the streamwise position $Z = 3\,m$, temperature gradients extend only until $x < 100\,mm$.

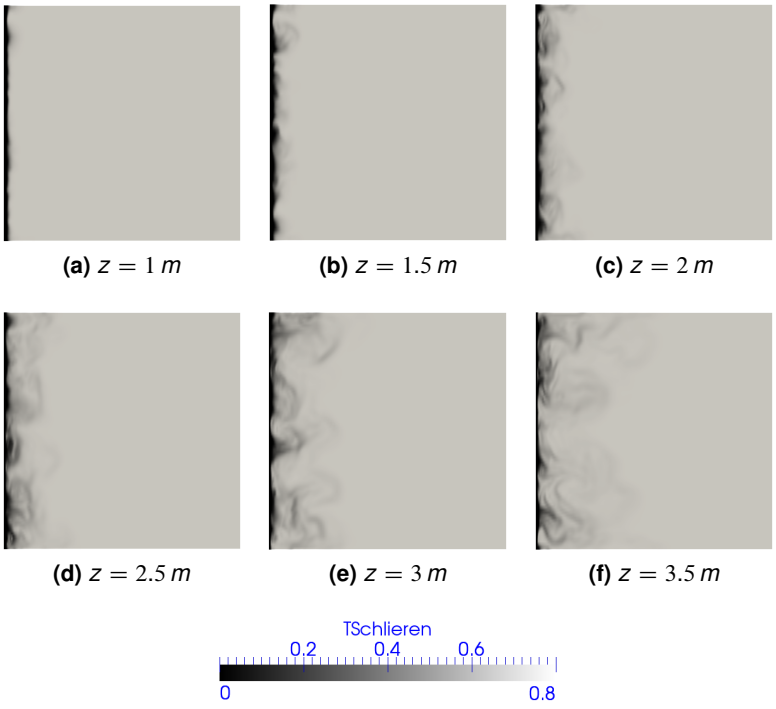


**(a)** $z = 1\,m$ **(b)** $z = 1.5\,m$ **(c)** $z = 2\,m$

**(d)** $z = 2.5\,m$ **(e)** $z = 3\,m$ **(f)** $z = 3.5\,m$

**Fig. 4.29:** Development of thermal plumes along the heated wall.

Wall temperatures at location $Z = 3\,m$ are listed in Tab. 4.8. It is interesting to note that the model with lowest $Pr_{sgs}$, LES1, gives highest wall temperature, see also Fig. 4.30. This is a consequence of ineffective heat transfer (small Nusselt number). Other simulations produce wall temperatures that are close to each other, between $\bar{T}_w = 311.6\,K$ and $\bar{T}_w = 312.4\,K$.

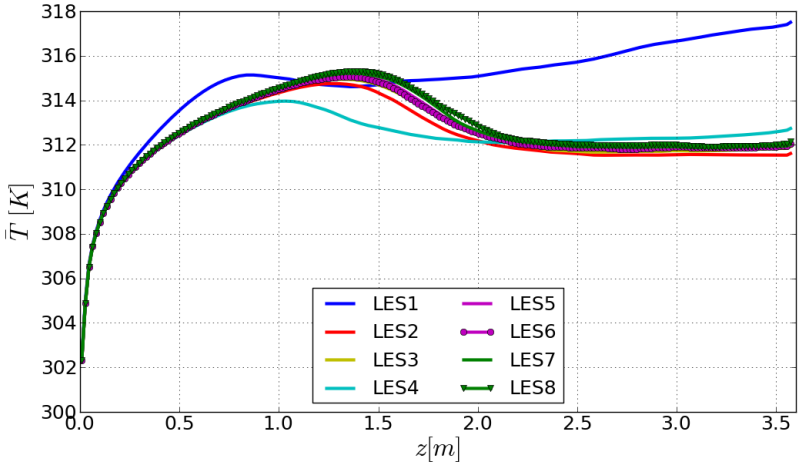


**Fig. 4.30:** Time-averaged wall temperatures for different simulations.

Local Nusselt numbers are shown in Fig. 4.31. They are calculated from the following equation:

$$Nu_z = \frac{hZ}{\lambda_f}, \tag{4.21}$$

where $\lambda_f$ is thermal conductivity evaluated at the film temperature, $Z$ is distance in the streamwise direction (flow direction) and $h$ is heat transfer coefficient

$$h = \frac{q_w}{(T_w - T_f)}. \tag{4.22}$$

Local Nusselt numbers at the measuring location, $Z = 3\,m$, are given in Tab. 4.5. For the experimental configuration Q1, local Nusselt number is $Nu_z = 1570$. Simulation LES4 was closest to this value, $Nu_z \approx 1620$, however, the mean temperature distribution predicted by this model was very poor. All dynamic models showed improvement over LES2 where the standard value for $Pr_{sgs}$ was used. The highest difference between different dynamic models was in the region $1.5\,m < Z < 2\,m$. The dynamic models for SGS heat flux, LES7 and LES8, produce slightly lower Nusselt numbers than dynamic models for $Pr_{sgs}$. Since the only difference between these two type of models is the buoyancy production term which is explicitly included in LES7 and LES8, we conclude that the buoyancy effects are the main reason for such a behavior of local Nusselt number.

### Model coefficients

Figure 4.32 shows dynamic $Pr_{sgs}$ obtained from LES5 for the first $2000$ seconds of physical time. Since the simulation was started from previously developed velocity and temperature fields, high oscillations of $Pr_{sgs}$ have not been observed. Highest value was $Pr_{sgs} = 10.2$ which appeared at $t = 1710.2\,s$. Averaged value for the first $2000\,s$ was $\bar{Pr}_{sgs} = 7.51$. This value is much higher than values that are commonly used in LES, which is, among other things, a consequence of the buoyancy effects. It is expected that with an increase of buoyancy force, or decrease of inlet velocity, $Pr_{sgs}$ will further increase. Further simulations showed that higher inlet velocities (lower influence of buoyancy force) reduced $Pr_{sgs}$. However, it has to be mentioned that $Pr_{sgs}$ is not only a function of buoyancy, but also of the mesh resolution.

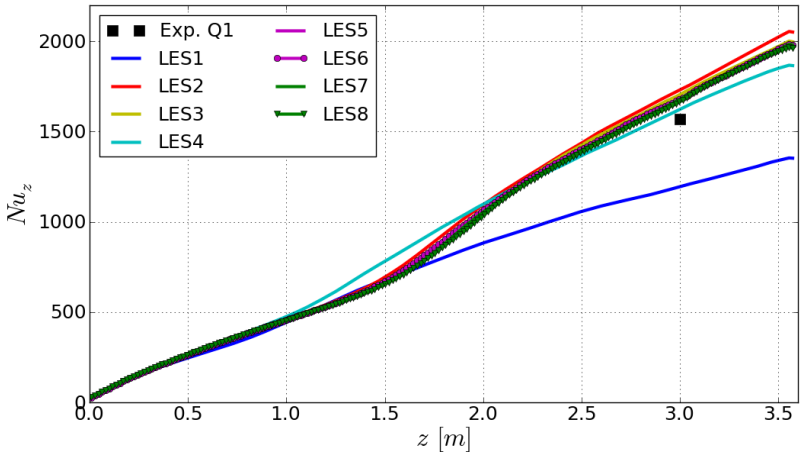


**Fig. 4.31:** Local Nusselt numbers at the heated wall for different simulations.

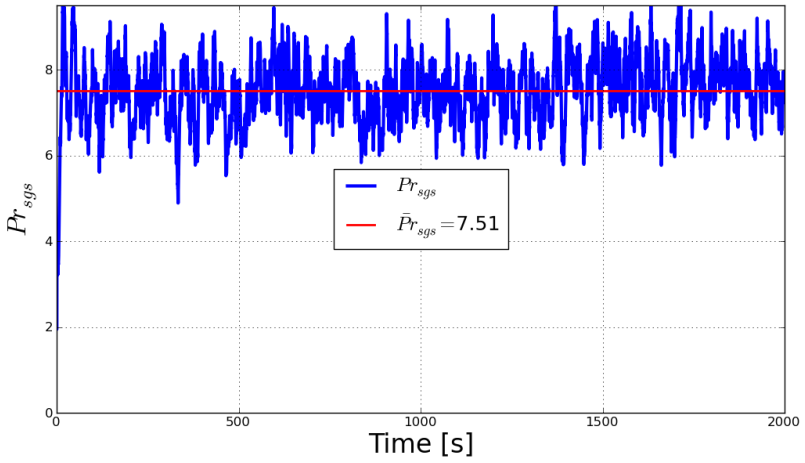


**Fig. 4.32:** Dynamic behavior of $Pr_{sgs}$.

Different meshes yield different values for $Pr_{sgs}$. Mesh dependency for $Pr_{sgs}$ will not be studied here.

Dynamic behavior of time dependent model coefficients $c_1$ and $c_2$ for the first $2000\,s$ of physical time are shown in Fig. 4.33. Strong oscillations of both $c_1$ and $c_2$ are limited to the firs $50 - 100$ seconds and after that initial period both coefficients approach and slightly oscillate around some mean values. This initialization period corresponds to approximately one flow-through time (residence time).

In the present case it is found that $c_1$ approaches and oscillates around $0.00016$ and $c_2$ around $0.38$. These oscillations of model coefficients did not affect computational stability so that the clipping of $c_1$ and $c_2$ was not necessary. In extreme cases, if the oscillations of model coefficients are very strong and frequent so that the computational stability is violated, further clipping of $c_1$ and $c_2$ values can be applied. Since the values of $c_1$ and $c_2$ are not known in advance, maximal and minimal allowable values, i.e. clipping limits, have to be determined *ad hoc*. This can be achieved by running the simulation on a coarse mesh and monitoring the behavior of model coefficients. Afterwards, the lowest and highest allowable values can be implemented in the code to prevent strong oscillations. However, in the test cases simulated so far, such an unstable behavior of model coefficients was not experienced.

Mean values, around which the model coefficients oscillate, depend on Reynolds number, molecular fluid properties, heat transfer, mesh resolution, etc. Since this approach of calculating the subgrid-scale heat flux is, to our knowledge, new in LES, it is necessary to conduct

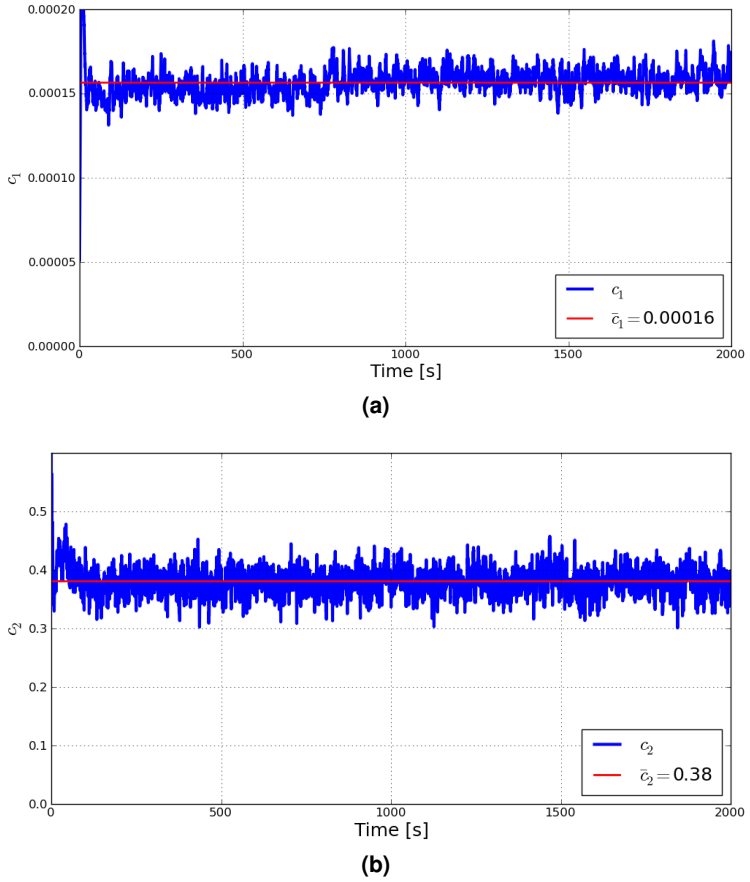


**Fig. 4.33:** Dynamic behavior of $c_1$ and $c_2$.

more computations with different fluids at heat transfer regimes in order to get further insight in the behavior of model coefficients.

### 4.3.4 Results - Case Q2

For the constant wall heat flux, $4000\,W/m^2$, an increase of the inlet velocity results in an increased influence of forced convection. In this experimental configuration, the inlet velocity is increased from $0.026\,m/s$ to $0.044\,m/c$ and the wall heat flux was kept the same as in $Q1$.

#### Velocity

Fig. 4.34 shows instantaneous (left) and time-averaged (right) streamwise velocity component. We can see that the influence of buoyancy force is reduced as compared to the experimental configuration $Q1$ where the inlet velocity was $0.026\,m/s$. Difference between the highest velocity near to the heated wall and velocity in the middle of the duct is not as big as in the previous case. The time-average velocity near to the heated wall is about $50\,\%$ larger than the value in the center. Due to the buoyancy force, the fluid is accelerated near the heated wall. However, the layer in which is the fluid accelerated is apparently thinner than in $Q2$. Compared to the Q1 case, it can be seen that the buoyancy force does not significantly affect the flow field before the streamwise length of $Z \approx 2.5\,m$.

Figure 4.35 (a) shows time-averaged streamwise velocity profile normalized by the centerline velocity for three different $Pr_{sgs}$ numbers, $0.1$, $0.9$ and $2$ and for the model with temperature

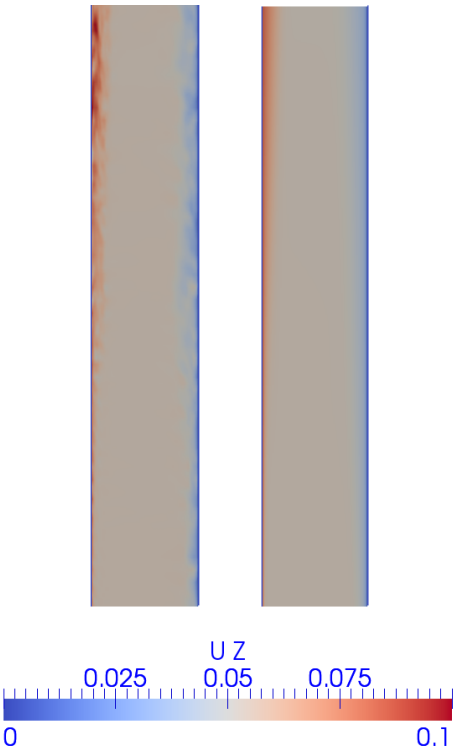


**Fig. 4.34:** Instantaneous and time-averaged streamwise velocity for case Q2.

dependent $Pr_{sgs}$, LES4. It can bee seen that $Pr_{sgs}$ has highest influence in the region close to the heated wall. Lower $Pr_{sgs}$ values produced lower velocity peak and smoother velocity gradient. This is probably caused by the higher effective thermal diffusivity which more effectively transports heat from the wall to the bulk region so that the temperature (and density) profile is more uniform. Values of $Pr_{sgs}$ obtained from LES4 are between $0.21$, and $0.23$,which corresponds to the lowest temperatures and to the highest temperatures respectively. Difference between LES1 ($Pr_{sgs} = 0.1$) and LES2 ($Pr_{sgs} = 0.9$) is much higher than difference between LES2 and LES3 ($Pr_{sgs} = 2$).

Velocity profiles for cases where dynamic models for $Pr_{sgs}$ and SGS heat flux are used are shown in Fig. 4.35 and LES2 is also given for comparison. We can see that all models produce very similar velocity distributions. The only simulation that slightly differs is LES6, where the localized dynamic model for $Pr_{sgs}$ is used. This simulation together with LES7 produce slightly higher velocity peaks. Away from the wall, $y > 50\,mm$, all models produce similar velocity profiles. This means that the influence of the SGS heat flux models on the velocity field is highest in the near-wall region. Agreement with the experimental measurements is fairly good. The highest discrepancy between the experimental and simulation velocity peaks is less than $8\,\%$.

### Temperature

Figures 4.36 (a) and (b) show time-averaged temperature distributions obtained from different simulations. Same as in the previous case, temperature is given in the dimensionless form, Eq. (4.15).

Effects of the various $Pr_{sgs}$ values on the time-averaged temperature distribution are shown in Fig. 4.36 (a). It can bee seen that low $Pr_{sgs}$ values (LES1 and LES2) produce

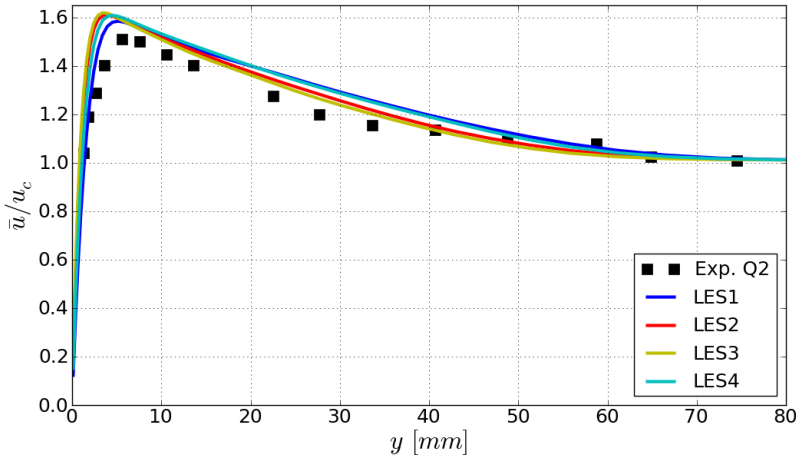


**(a)**

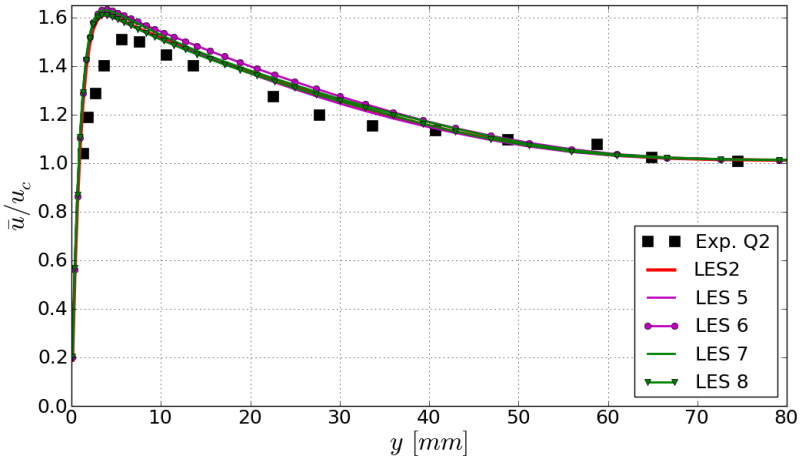


**(b)**

**Fig. 4.35:** Time averaged streamwise velocity.

very smooth temperature gradients. Due to the high effective thermal diffusivity produced by low $Pr_{sgs}$ ($0.1$ in LES1), heat is effectively removed from the heated wall, resulting in an incorrect temperature distribution. In LES4, $Pr_{sgs}$ depends on temperature and, as mentioned before, it varies between $0.21$ and $0.23$. In this case, temperature distribution is much closer to the experimental measurements, but discrepancy is still to high. Further increase of $Pr_{sgs}$ ($0.9$ in LES2 and $2$ in LES3) results in further improvement of temperature prediction. However, it is very interesting to note that there is almost no difference between LES2 and LES3, as it was the case in Q1. From these results we can conclude that

- For a given computational mesh, an increase of the forced convection influence leads to a lower $Pr_{sgs}$ value
- For a given computational mesh, an increase of the natural convection influence (buoyancy force) increases the influence of the subgrid scales requirements, i.e. if velocity is reduced, number of mesh cells may become insufficient

However, these conclusions are based just on the present test case and additional investigations are necessary.

A better agreement between the experimental measurements and simulation results can be achieved by using the dynamic models for $Pr_{sgs}$ (LES5 and LES6) or by using the dynamic models for subgrid-scale heat flux (LES7 and LES8). Comparison between these models

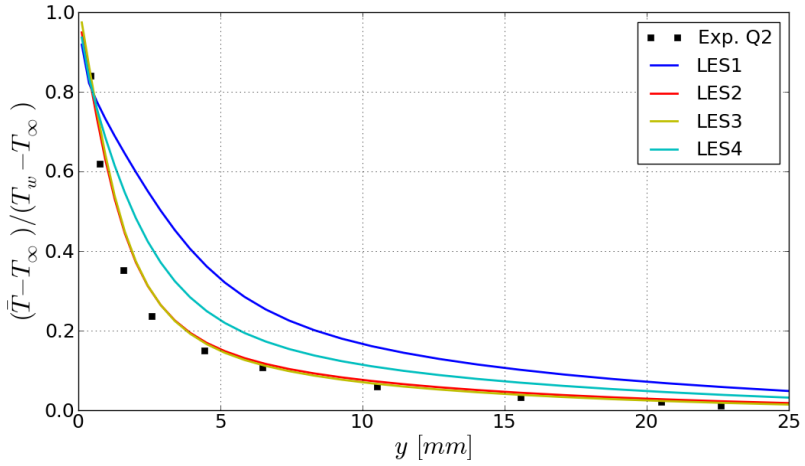


**(a)**

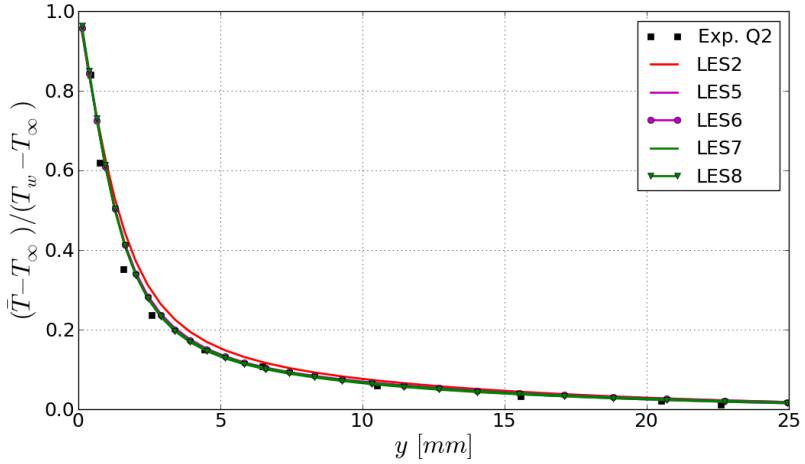


**(b)**

**Fig. 4.36:** Time averaged normalized temperature distribution.

and standard gradient model with $Pr_{sgs} = 0.9$ is given in Fig. 4.36 (b). All models show improvement over the standard model, while the difference among dynamic models is small.

Temperature rms values are plotted in Fig. 4.37 (a) and (b). It can bee seen that simulation with lowest $Pr_{sgs}$ (LES1) underpredicts the experimental measurements near the wall ($y < 3\,mm$) and overpredicts measurements away from the wall, $y > 3\,mm$. On the other hand, higher $Pr_{sgs}$ values used in LES2 and LES3 resulted in overprediction of the measurements in the near-wall region and underprediction apart from the wall. The model for $Pr_{sgs}$ based on the fluid temperature showed the best behavior.

Furthermore, it is observed that with an increase of $Pr_{sgs}$, peak of the temperature rms values increases and moves toward the wall. This is contrary to the previous configuration (Q1) where the peak of temperature rms values decreased with increasing $Pr_{sgs}$.

When the dynamic models for $Pr_{sgs}$ and SGS heat flux are applied, temperature RMS values overpredict the experimental measurements in the near-wall region, and underpredict the measurements away from the wall. The profile is close to LES2 profile, with the highest discrepancy less than $1\,\%$. This is probably caused by the slightly higher wall temperature. The highest discrepancy between the simulations LES5 to LES8 and experimental measurements is less than $5\,\%$.

Time-averaged wall temperatures are given in Tab. 4.8. As expected, lowest wall tem-

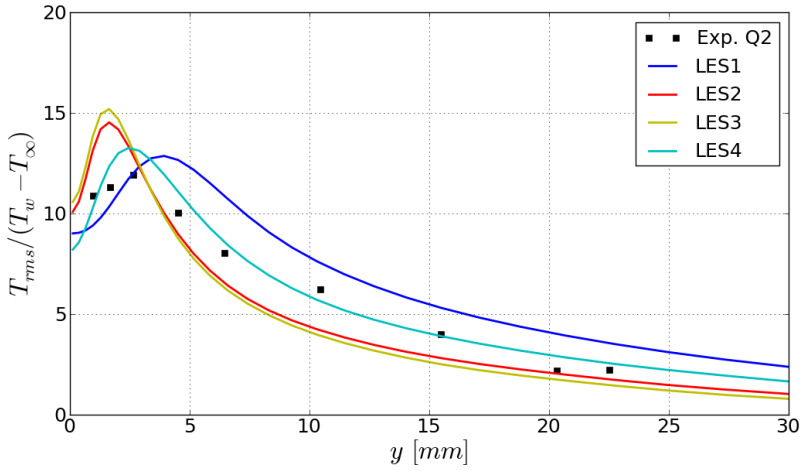


**(a)**

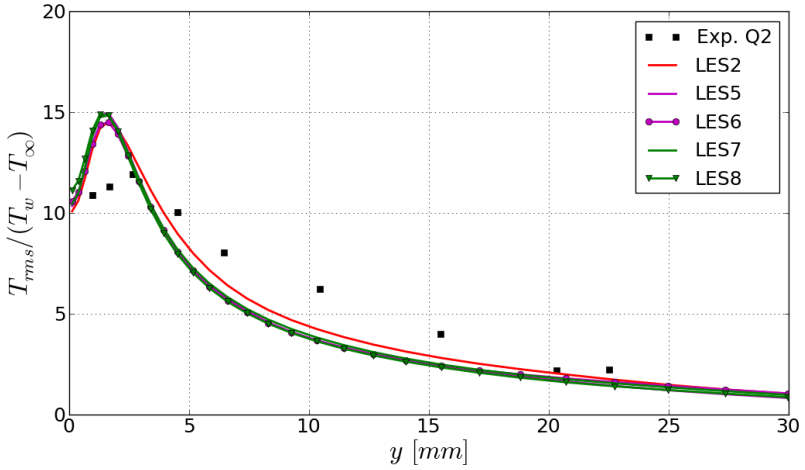


**(b)**

**Fig. 4.37:** RMS of temperature fluctuations.

perature , $T_w = 306.41\,[K]$ was obtained in LES1, where the lowest $Pr_{sgs}$ was used. When the model with temperature dependent $Pr_{sgs}$ is applied (LES4), wall temperature was $T_w = 309.1\,[K]$. These low wall temperatures are caused by higher effective thermal diffusivity. Increase of $Pr_{sgs}$ (LES2 and LES3) led to the further increase of wall temperature, but difference was less than $1\,[K]$. Dynamic models for $P_{sgs}$ and SGS heat flux (LES5 to LES8) increased the wall temperature up to $T_w \approx 314\,[K]$.

**Tab. 4.8:** Time-averaged wall temperatures for Q1 and Q2 cases.

| Simulation | Q1, $\bar{T}_w\,[K]$ | Q2 $\bar{T}_w\,[K]$ |
|---|---|---|
| LES1 | 316.9 | 306.4 |
| LES2 | 311.6 | 312.7 |
| LES3 | 311.8 | 313.5 |
| LES4 | 312.4 | 309.1 |
| LES5 | 311.9 | 313.8 |
| LES6 | 311.9 | 313.5 |
| LES7 | 311.9 | 313.8 |
| LES8 | 312 | 313.9 |

Figures 4.38 (a) to (d) show instantaneous and time-averaged wall temperatures for Q1

(figures a and b) and Q2 (figures c and d) obtained from case LES7. Higher temperature regions correspond to the lower heat transfer coefficients. Streaky patterns, that are observed in the experiment, are also found here. It can be seen that higher buoyancy influence (case Q1) causes that transition to turbulence occurs earlier.

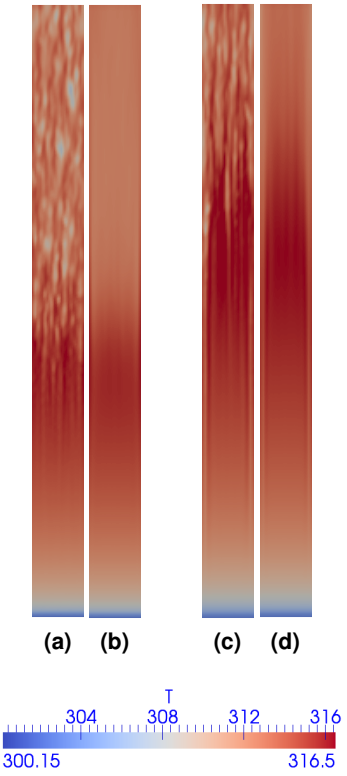


**Fig. 4.38:** Case Q1: (a) instantaneous wall temperature, (b) time-averaged wall temperature; Case Q2: (a) instantaneous wall temperature, (b) time-averaged wall temperature. Results are from case LES7.

Figure 4.39 shows the development of the time-averaged temperature over the heated wall at the middle of the duct ($y = 0$). High discrepancy among different models can be observed. For the low $Pr_{sgs}$ values, wall temperature reaches some value and stays almost constant. Starting from the streamwise location of $Z = 0.5\,m$, difference between LES2, which uses a common value for subgrid-scale turbulent Prandtl number $Pr_{sgs} = 0.9$, and dynamic models is monotonically increasing until $Z \approx 2.3\,m$. Simulations based on the dynamic models for SGS heat flux (LES7 and LES8) produce very similar wall temperatures. These models also predict higher wall temperatures than the dynamic $Pr_{sgs}$ models.

Figure 4.40 shows local Nusselt numbers, $Nu_z$, along the heated wall. Local Nusselt number is given by Eq. (4.21). Again, smaller $Pr_{sgs}$ values considerably increase heat transfer which results in much higher than experimental Nusselt number. Furthermore, $Pr_{sgs} = 0.9$ (LES2) seams to be too small to correctly predict the effects of natural convection in buoyancy aiding flow since the local Nusselt number at $Z = 3\,m$ is higher than the experimental result, $Nu_z \approx 1570$ compared to $Nu_z \approx 1470$. This means that, if the model for SGS heat flux is based on the constant subgrid-scale turbulent Prandtl number, a larger value for $Pr_{sgs}$ has to be used when simulating turbulent flows with high influence of buoyancy.

Modeling of heat transfer is improved by using dynamic models for $Pr_{sgs}$ and subgrid-scale heat flux. All models, LES5 to LES8, produce nearly the same values for local Nusselt numbers which are close to the experimental measurements, $Nu_t = 1470$. All dynamic models showed a clear improvement over the model with a standard, constant value for $Pr_{sgs}$, LES2.

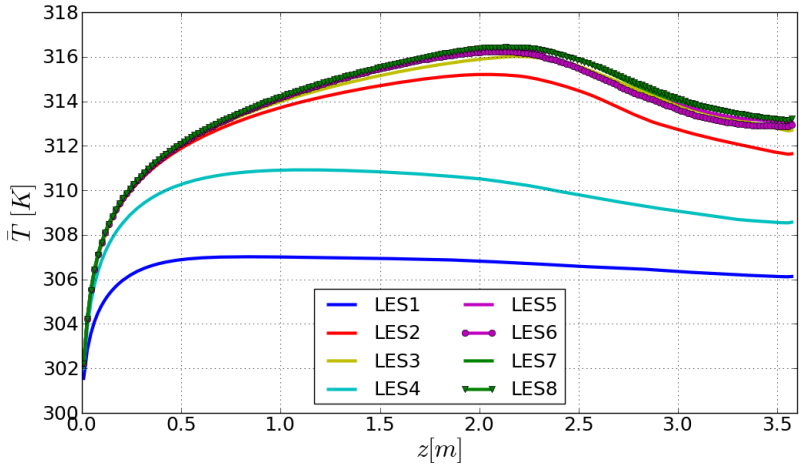


**Fig. 4.39:** Time-averaged wall temperatures at the heated wall for different simulations.

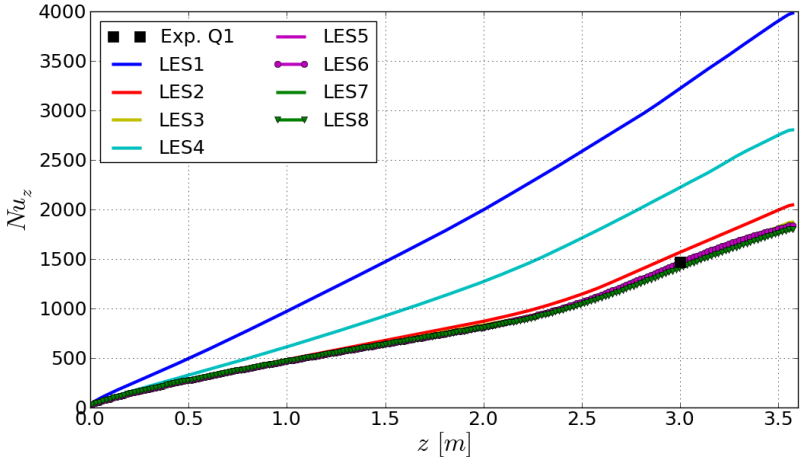


**Fig. 4.40:** Local Nusselt numbers at the heated wall for different simulations.

### Model coefficients

Figure 4.41 shows variation of $Pr_{sgs}$ during the first $1200$ seconds of physical time obtained from LES5. Averaged value for this simulation period was $\bar{Pr}_{sgs} = 5.85$. Because the simulation was started from already developed velocity and temperature fields obtained by simulating the same test case but on a coarser mesh (that contained approximately $100000$ cells), strong oscillations of $Pr_{sgs}$ were avoided. The lowest value was $Pr_{sgs} \approx 0.68$ at $t \approx 0.18\,s$. Nevertheless, it took about $250\,s$, which corresponds to approximately three flow-through times, until $Pr_{sgs}$ approached a mean value of $5.85$.

As we can see from the results, the time-averaged $Pr_{sgs}$ evaluated for this case is smaller than in the previous case, where the inlet velocity was lower, $5.85$ compared to $7.51$. Since the computational mesh and wall heat flux are same for both cases, the reduction of $Pr_{sgs}$ must be caused by the higher inlet velocity. In Q2, the influence of forced convection is larger than in Q1. Hence, for the mixed convection heat transfer regime, we can conclude that, if the natural convection heat transfer is increased with respect to the forced convection, $Pr_{sgs}$ will increase too.

Figure 4.42 shows the dynamic behavior of model coefficient $c_1$ (a) and $c_2$ (b). Slightly stronger oscillations are observed only in the first $50$ seconds. After this initial period, both coefficients converge very fast to mean values $\bar{c}_1 = 1.1 \times 10^{-4}$ and $\bar{c}_2 = 0.39$. Within this initial period, $c_1$ was oscillating between lowest value $c_1^{min} = 3.2 \times 10^{-5}$ and highest value

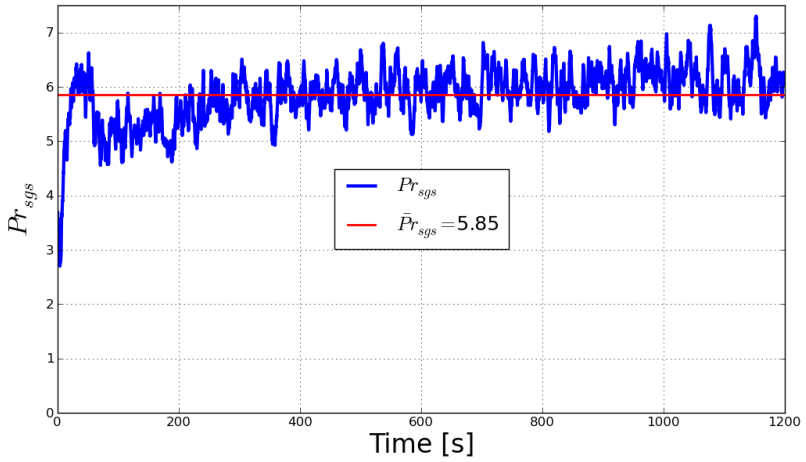


**Fig. 4.41:** Dynamic behavior of $Pr_{sgs}$.

$c_1^{max} = 1.6 \times 10^{-4}$. $c_2$ was oscillating between $c_2^{min} = 0.09$ and $c_2^{max} = 1.03$.

The time-averaged model coefficient $c_1$ in the present case, $\bar{c}_1^{Q2} = 0.00011$, is lower than in the previous case, $\bar{c}_1^{Q1} = 0.00016$. This is associated with the reduction of velocity fluctuations. Namely, it is found out in the experiment and also in the present simulations that velocity fluctuations decrease significantly with an increase of inlet velocity. Velocity fluctuations decrease until a certain value of inlet velocity is reached, after which a further increase of inlet velocity leads to an increase of velocity fluctuations. In the present experiment, velocity fluctuations were decreasing monotonically for inlet velocities of $u_{in} = 0.026, 0.044$ and $0.096\, m/s$. However, when the inlet velocity was increased to $u_{in} = 0.112\, m/s$, velocity fluctuations were increased too. The highest value of velocity fluctuations was obtained for $u_{in} = 0.026\, m/s$.

On the other hand, because the variations in fluid temperature are small, the time-averaged coefficient $c_2$ increased only from $0.38$ to $0.39$. From table 4.8 we can see that the wall temperatures in Q2 ($\bar{T}_w = 313.8\, K$) are higher than in Q1 ($\bar{T}_w = 311.9\, K$). Since the inlet temperature was constant in both cases ($T_{in} = 300.15\, K$), the higher temperature difference that occurs in Q2 can be the reason for increase in $c_2$. Nevertheless, further simulations with different heat transfer conditions are required in order to get a better understanding in the behavior of model coefficients.

Same as $Pr_{sgs}$, coefficients $c_1$ and $c_2$ also depend on the mesh size and this has to be investigated further. In all cases that have been tested so far, oscillations of model coefficients did not violate the computational stability.

### 4.3.5 Discussion

The present numerical studies have been performed to investigate the dynamic model for subgrid-scale heat flux which is applied to simulate a buoyancy-aided turbulent convective heat transfer to water flowing through a $3.6\, m$ long vertical duct with one of the walls heated with uniform wall heat flux, $q_w = 4000\, W/m^2$. Two experimental configurations have been considered: Q1, where the inlet velocity was $u_{in} = 0.026\, m/s$, and Q2, where the inlet velocity was $u_{in} = 0.044\, m/s$. The computational domain consisted of $384$ thousands cells.

Dynamic models for $Pr_{sgs}$ and SGS heat flux are used to close the energy equation. Simulation results are compared with the experimental measurements and with the results obtained by using simple SGD model with three different subgrid scale-turbulent Prandtl numbers: $Pr_{sgs} = 0.1, 0.9$ and $2$ and one that uses a temperature dependent $Pr_{sgs}$. Conclusions

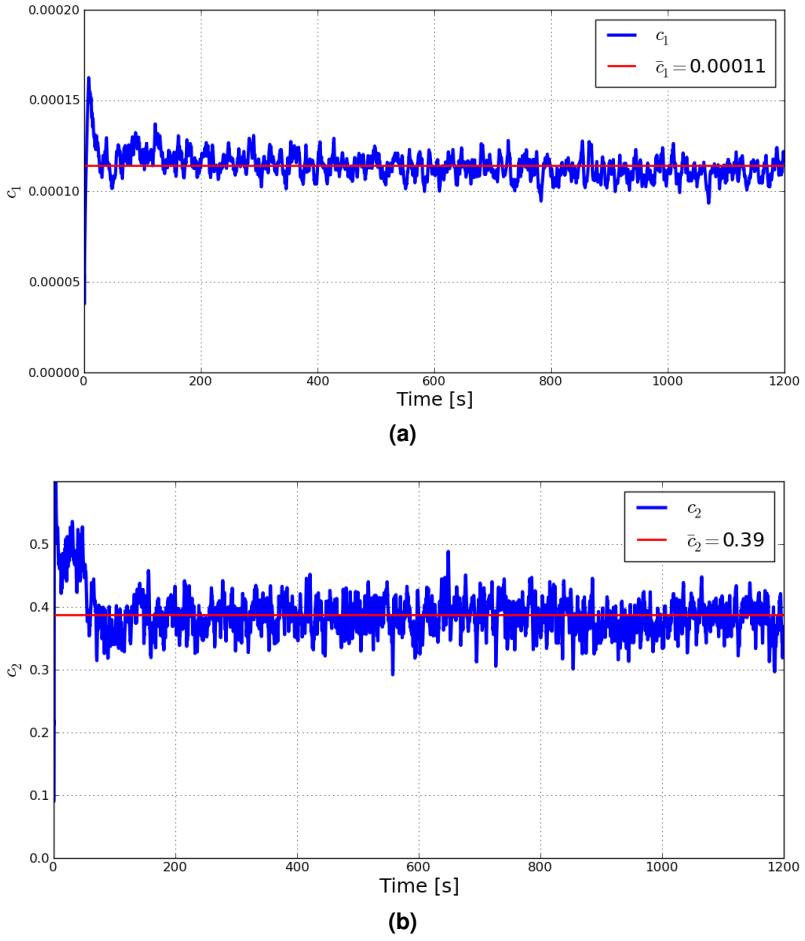


**Fig. 4.42:** Dynamic behavior of $c_1$ and $c_2$.

from the simulation results can be divided into two groups, one considering subgrid-scale turbulent Prandtl number and the other considering the dynamic model for subgrid-scale heat flux.

- **A value for** $Pr_{sgs}$. As it was expected, $Pr_{sgs}$ significantly affects both velocity and temperature fields. Values that are too low lead to the wrong prediction of time-averaged temperature distribution, see Fig. 4.25 and 4.36. Effectiveness of heat transfer is also affected, see Fig. 4.30, 4.31, 4.39 and 4.40. In Q1, effectiveness of heat transfer was reduced when low values for $Pr_{sgs}$ were used. Contrary, heat transfer was more effective for low $Pr_{sgs}$ values in Q2. The velocity field was especially affected by $Pr_{sgs}$ in Q1, where the buoyancy effects were more important. This is shown in Fig. 4.24. Low $Pr_{sgs}$ values produced very high velocities in the near-wall region, up to four times higher that the value in the duct center ($Pr_{sgs} = 0.1$). Dynamic models for $Pr_{sgs}$ improved simulation results and showed that with higher buoyancy influence, a higher value for $Pr_{sgs}$ may be required, see Fig. 4.32 and 4.41.

- **Dynamic model for SGS heat flux**. Models based on an algebraic relation for subgrid-scale heat flux showed improvement over the models with fixed $Pr_{sgs}$. Results are close to those obtained with the dynamic models for $Pr_{sgs}$, which is probably a consequence of relatively small changes in fluid temperature (less than $20\,°C$). This is expected to be changed for higher oscillations in temperature field. Model coefficients $c_1$ and $c_2$ showed a stable behavior and converged very fast to some constant values. Higher oscillations were observed only at the beginning of the simulation and this is because the simulations were started from previously developed velocity and temperature fields. Some

preliminary testes showed that computations started from the uniform (zero-gradient) velocity and temperature fields can become unstable. This can be avoided by "clipping" very high or very low values of model coefficients.

# Chapter 5

# Conclusions and Outlook

The goal of the present study was to propose a new approach for determination of the subgrid-scale heat flux for turbulent flows which are significantly influenced by the buoyancy force. For that purpose, the dynamic procedure is used to model subgrid-scale turbulent Prandtl number and heat flux. The new model was implemented in an open source computational fluid dynamics toolbox, OpenFOAM. Two different type of models for SGS heat flux are derived

- Dynamic model for subgrid-scale turbulent Prandtl number
- Dynamic model for subgrid-scale heat flux.

The idea of using the dynamic procedure to evaluate $Pr_{sgs}$ was previously used by some researchers (see Chapter 2). In this work, the same approach is adopted do derive a model for $Pr_{sgs}$ which is based on the one equation model for momentum equation. Depending on how the model coefficients are trated, there are two possibilities to evaluate $Pr_{sgs}$: either as a volume-averaged, time-dependent single value which is constant for the whole computational domain, or as a spatially and time dependent value. The dynamic $Pr_{sgs}$ model was validated by simulating the T-junction benchmark test case. The simulations results showed fairly good agreement with the experimental measurements. Even though high oscillations of $Pr_{sgs}$ occurred in the initial period, the computational stability was not affected. The time-averaged $Pr_{sgs}$ value was $0.65$, which is within the suggested range for $Pr_{sgs}$ found in the literature.

A more robust approach to calculate SGS heat flux is to use an algebraic relation which combines gradient diffusion hypothesis and the buoyancy production term. By doing so, the buoyancy effects can be explicitly included in the SGS heat flux model.

In the next step, a new algebraic model for SGS heat flux is proposed. The new model explicitly includes the buoyancy production term from the transport equation for SGS heat flux. Temperature variance, which appears in the buoyancy production term, is modeled by a new term which is proportional to the production term from the transport equation for temperature variance and some constant of proportionality, named $c_2$ in the present work. As a result, the new model for subgrid-scale heat flux contains two parts: a gradient diffusion hypothesis and production due to the buoyancy effects. Eventually, the dynamic procedure is applied in order to evaluate model coefficients, denoted as $c_1$ and $c_2$, which multiply each of the terms in model. In the previous part of the work, this procedure was successfully applied to evaluate $Pr_{sgs}$. Since the dynamic model for SGS heat flux includes two separate terms, a system of two linear algebraic equations has to be solved in order to calculate the model coefficients. An alternative approach is to treat the model terms independently of each other which leads to two separate equations for each of the model coefficients. Depending on the treatment of the model coefficients, two variants of the model are possible: volume averaged

(each of the model coefficients has a single value for the whole computational domain) and locally dependent (model coefficients depend on the local flow and heat transfer conditions). A detailed derivation of the model is given in Chapter 3.

For validation of the dynamic model for SGS heat flux, chosen is an experiment where the aiding flow of water through a vertical duct is investigated. Beside this model, which is based on an algebraic relation for SGS heat flux, the simple gradient diffusion model was also tested. In order to check how $Pr_{sgs}$ affects velocity and temperature fields, three different constant values were used: $Pr_{sgs} = 0.1, 0.9$ and $2$. In addition, two models for $Pr_{sgs}$ were also tested. The first one is the temperature dependent model which was described in Chapter 2. Here, $Pr_{sgs}$ depends on the local fluid temperature. The second model is the dynamic model $P_{sgs}$, derived in Chapter 3.

Results showed that $Pr_{sgs}$ value has significant influence both on time averaged and rms values. Small $Pr_{sgs}$ value results in smoother temperature gradient which is a consequence of higher effective thermal diffusivity. By increasing the $Pr_{sgs}$, the temperature gradient becomes sharper and the time averaged temperature shows a good agreement with experimental measurements. Therefore, when the simple gradient diffusion model is used, the choice of $Pr_{sgs}$ is very important when simulating a turbulent flow with significant influence of buoyancy (or some other heat transfer regime, where temperature field acts as an active scalar). Moreover, $Pr_{sgs}$ has a significant effect on the velocity field. These effects are more important if the buoyancy force is higher. By increasing the inlet velocity, the forced convection becomes the dominant mechanism of heat transfer, thereby reducing the influence of $Pr_{sgs}$ on the velocity field.

Temperature dependent $Pr_{sgs}$ model showed very good agreement with the experimental measurements in the case of forced convection (T-junction test case). However, in the case of buoyancy dominated heat transfer, it turned out the $Pr_{sgs}$ calculated on this way has rather small values, which caused excessive transport of heat from the heated wall to the bulk region. This resulted in a smoother temperature gradient in the near wall region.

Instead of prescribing a value for $Pr_{sgs}$, the dynamic approach is applied and results showed improvements over the standard method. $Pr_{sgs}$ is self-calibrating to different flow and heat transfer conditions. The simulation was started from the previously developed velocity and temperature fields, thereby preventing strong oscillations and potential computational instabilities. For a fixed wall heat flux, it is shown that inlet velocity significantly affects $Pr_{sgs}$. In addition, it is also found out that higher influence of buoyancy also requires a higher value for $Pr_{sgs}$. For the considered experimental configurations and computational mesh, no significant difference between the volume averaged and locally dependent versions of the model was observed.

The main contribution of this work is the dynamic model for subgrid-scale heat flux. The proposed model performed as well or better than dynamic $Pr_{sgs}$ model. In both experimental configurations improvements over the gradient diffusion model with constant $Pr_{sgs}$ are achieved. Behavior of the model coefficients was also monitored. For the fixed heating (same wall heat flux is used in both experimental configurations), the model coefficient $c_1$ (multiplies the gradient diffusion term) varied more than $c_2$ (multiplies the buoyancy production term). The change in $c_1$ is mainly caused by an increase or a decrease (depending on the inlet velocity) of velocity fluctuations. Because of the low variations in fluid temperature, $c_2$ stayed almost constant for the both experimental configurations. However, in order to get a better understanding in the behavior of the model coefficients, it is necessary to perform more test cases with different configurations (different working fluids, higher temperature variations within the fluid, etc).

Overall, the present validation test showed that the dynamic model for subgrid-scale heat flux can be successfully applied to calculate buoyancy dominated flows. It is expected that

the model is able to perform equally well for the purely forced or natural convection; therefore, additional simulation tests are required.

# Bibliography


[1] *www.openfoam.org*.

[2] *Ansys ICEM CFD 12.1 User Manual*.

[3] http://webbook.nist.gov/chemistry/fluid/.

[4] H. I. Abu-Mulaweh. Investigations on the effect of backward-facing and forward-facing steps on turbulent mixed-convection flow over a flat plate. *Experimental Heat Transfer*, 22:117–127, 2009.

[5] G. B. Arfken, H. J. Weber, and F. Harris. *Mathematical Methods for Physicists, Fifth Edition*. Harcourt/Academic Press, 2001.

[6] J. Bardina, J. H. Ferziger, and W. C. Reynolds. Improved subgrid scale models for large eddy simulation. In *AIAA 13th Fluid & Plasma Dynamics Conference July 14-16, 1980/Snowmass, Colorado*, 1980.

[7] J. Bardina, J. H. Ferziger, and W. C. Reynolds. *Improved turbulence models based on large eddy simulation of homogenepus, incompressible, turbulent flows*. PhD thesis, Stanford University, 1983.

[8] G. K. Batchelor. Diffusion in a field of homogeneous turbulence. Technical report, Trinity College, Cambridge, 1949.

[9] M. L. Boas. *Mathematical Methods in the Physical Sciences*. John Wiley & Sons, Inc., 2006.

[10] W. Cabot. Large eddy simulations of time-dependent and buoyancy-driven channel flows. Technical report, Center for Turbulence Research, Stanford University/NASA Ames, 1992.

[11] A. D. Carr, M. A. Connor, and H. O. Buhr. Velocity, temperature, and turbulence measurements in air for pipe flow with combined free and forced convection. *Journal of Heat Transfer*, pages 445–452, 1973.

[12] H. Choi and P. Moin. Grid-point requirements for large eddy simulation: Chapman's estimates revisited. *Physics of Fluids*, 24:011702, 2012.

[13] S. Corrsin. On the spectrum of isotropic temperature fluctuations in an isotropic turbulence. *Journal of Applied Physics*, 22:469–473, 1951.

[14] L. D. Dailey, N. Meng, and R. H. Pletcher. Large eddy simulation of constant heat flux turbulent channel flow with property variations: Quasi-developed model and mean flow results. *Journal of Heat Transfer*, 125:27–38, 2003.

[15] B. J. Daly and F. H. Harlow. Transport equations in turbulence. *Physics of Fluids*, 13: 2634, 1970.

[16] P. A. Davidson. *Turbulence: An Introduction for Scientists and Engineers*. Oxford University Press, 2004.

[17] E. de Villiers. *The Potential of Large Eddy Simulation for the Modeling of Wall Bounded Flows*. PhD thesis, Imperial College of Science, Technology and Medicine, 2006.

[18] J. W. Deardorff. On the magnitude of the subgrid scale eddy coefficient. *Journal of Computational Physics*, 7:120–133, 1971.

[19] J. W. Deardorff. Numerical investigation of neutral and unstable planetary boundary layers. Technical report, National Center for Atmospheric Research, Boulder, Colo. 80302, 1972.

[20] P. A. Durbin and B. A. P. Reif. *Statistical Theory and Modeling for Turbulent Flows -2nd ed.* John Wiley & Sons Ltd, 2011.

[21] S. Dutta, X. Zhang, J. A. Khan, and D. Bell. Adverse and favorable mixed convection heat transfer in a two-side heated square channel. *Experimental Thermal and Fluid Science*, 18:314–322, 1999.

[22] T. M. Eidson. Numerical simulation of the turbulent rayleigh-benard problem using subgrid modelling. *Journal of Fluid Mechanics*, 158:245–268, 1985.

[23] A. Fabregat, J. Pallarès, I. Cuesta, and F. X. Grau. Dispersion of a buoyant plume in a turbulent pressure-driven channel flow. *International Jouranl of Heat and Mass Transfer*, 52:1827–1842, 2009.

[24] Alexandre Favre. Turbulence: Spacetime statistical properties and behavior in supersonic flows. *Physics of Fluids*, Vol. 26:2851, 1983.

[25] J. H. Ferziger and M. Peric. *Computational Methods for Fluid Dynamics*. Springer-Verlag, 2002.

[26] P. Forooghi and K. Hooman. Numerical study of turbulent convection in inclined pipes with significant buoyancy influence. *International Jouranl of Heat and Mass Transfer*, 61:310–322, 2013.

[27] Th. Frank, C. Lifante, H.-M. Prasser, and F. Menter. Simulation of turbulent and thermal mixing in t-junctions using urans and scale-resolving turbulence models in ansys cfx. *Nuclear Engineering and Design*, 240:2313?2328, 2010.

[28] J. Fröhlich. *Large Eddy Simulation turbulenter Strömungen*. B.G. Teubner Verlag / GWV Fachverlage GmbH, 2006.

[29] K. Fukui and M. Nakajima. Unstable stratification effects on turbulent flow in the wall region. *International Jouranl of Heat and Mass Transfer*, 28:2343–2352, 1985.

[30] C. Fureby, G. Tabor, H. G. Weller, and A. D. Gosman. A comparative study of subgrid scale models in homogeneous isotropic turbulence. *Physics of Fluids*, 9(5):1416, 1997.

[31] E. Garnier, N. Adams, and P. Sagaut. *Large Eddy Simulation for Compressible Flows*. Springer Science+Business Media B.V., 2009.

[32] M. Germano. A proposal for a redefinition of the turbulent stresses in the filtered navier stokes equations. *Physics of Fluids*, 29:2323, 1986.

[33] M. Germano. *Modern Simulation Strategies for Turbulent Flow*, chapter Ten years of the dynamic model, pages 173–190. 2001.

[34] M. Germano, U. Piomelli, P. Moin, and W. H. Cabot. A dynamic subgrid-scale eddy viscosity model. *Physics of Fluids*, 3:1760, 1991.

[35] S. Ghosal and P. Moin. The basic equations for the large eddy simulation of turbulent flows in complex geometry. *Journal of Computational Physics*, 118(118):24–37, 1995.

[36] S. Ghosal, T. S. Lund, P. Moin, and K. Akselvoll. A dynamic localization model for large-eddy simulation of turbulent flows. *Journal of Fluid Mechanics*, 286:229–255, 1995.

[37] A. Hadjadj and A. Kudryavtsev. Computation and flow visualization in high-speed aerodynamics. *Journal of Turbulence*, 6:1–25, 2005.

[38] M. H. C. Hannink and F. J. Blom. Numerical methods for the prediction of thermal fatigue due to turbulent mixing. *Nuclear Engineering and Design*, 241:681–687, 2011.

[39] H. Hattori and Y. Nagano. Direct numerical simulation of turbulent heat transfer in plane impinging jet. *International Journal of Heat and Fluid Flow*, 25:749–758, 2004.

[40] J. Hinze. *Turbulence*. McGraw-Hill, 1975.

[41] S. M. Hosseini, K. Yuki, and H. Hashizume. Classification of turbulent jets in a t-junction area with a 90-deg bend upstream. *International Journal of Heat and Mass Transfer*, 51:2444–2454, 2008.

[42] O. Iida and N. Kasagi. Direct numerical simlation of unstably stratified turbulent channel flow. *Journal of Heat Transfer*, 119:53–61, 1997.

[43] J. D. Jackson. Turbulent mixed convection heat transfer to liquid sodium. *International Jouranl of Heat and Fluid Flow*, 4:107–111, 1983.

[44] J. D. Jackson, M. A. Cotton, and B. P. Axcell. Studies of mixed convection in vertical tubes. *International Jouranl of Heat and Fluid Flow*, 10:2–15, 1989.

[45] J. D. Jackson, B. P. Axcell, and A. Walton. Mixed convection heat transfer to sodium in a vertical pipe. *Experimental Heat Transfer*, 7:71–90, 1994.

[46] H. Jasak. *Error Analysis and Estimation for the Finite Volume Method with Applications to Fluid Flows*. PhD thesis, Imperial College of Science, Technology and Medicine, 1996.

[47] S. T. Jayaraju, E. M. J. Komen, and E. Baglietto. Suitability of wall-functions in large eddy simulation for thermal fatigue in a t-junction. *Nuclear Engineering and Design*, 240:2544–2554, 2010.

[48] C. Jiménez, L. Valiño, and C. Dopazo. A priori and a posteriori tests of subgrid scale models for scalar transport. *Physics of Fluids*, 13:2433, 2001.

[49] A. K. Karna and D. V. Papavassiliou. Near-wall velocity structures that drive turbulent transport from a line source at the wall. *Physics of Fluids*, 24:035102, 2012.

[50] N. Kasagi and M. Nishimura. Direct numerical simulation of combined forced and natural turbulent convection in a vertical plane channell. *International Jouranl of Heat and Fluid Flow*, 18:88–99, 1997.

[51] F. Kawamura, Y. Seki, K. Iwamoto, and H. Kawamura. Dns of heat transfer in turbulent and transitional channel flow obstructed by rectangular prisms. *International Jouranl of Heat and Fluid Flow*, 28:1291–1301, 2007.

[52] J. Kim and J. J. Jeong. Large eddy simulation of turbulent flow in a t-junction. *Numerical Heat Transfer*, 61:180–200, 2012.

[53] J. Kim and P. Moin. Transport of passive scalars in turbulent channel flow. Technical report, NASA, 1987.

[54] W. W. Kim and S. Menon. A new dynamic one-equation subgrid-scale model for large eddy simulations. In *33rd Aerospace Sciences Meeting and Exhibit*, 1995.

[55] K. Kitamura and T. Inagaki. Turbulent heat and momentum transfer of combined forced and natural convection along a vertical flat plate-aiding flow. *International Jouranl of Heat and Mass Transfer*, 30:23–41, 1987.

[56] J. U. Knebel, L. Krebs, U. Müller, and P. B. Axcell. Experimental investigation of a confined heated sodium jet in a co-flow. *Journal of Fluid Mechanics*, 368:51–79, 1998.

[57] A. N. Kolmogorov. The local structure of turbulence in incompressible viscous fluid for very large reynolds numbers. *Dokl. Akad. Nauk SSSR*, 30:9–13, 1941.

[58] S. Komori and H. Ueda. Turbulence structure in unstably-stratified open-channel flow. *Physics of Fluids*, 25:1539, 1982.

[59] M. Kree, J. Duplat, and E. Villermaux. The mixing of distant sources. *Physics of Fluids*, 25:091103, 2013.

[60] N. Kruse and P. R. von Rohr. Structure of turbulent heat flux in a flow over a heated wavy wall. *International Journal of Heat and Mass Transfer*, 49:3514–3529, 2006.

[61] G.M. Laskowski, S.P. Kearney, G. Evans, and R. Greif. Mixed convection heat transfer to and from a horizontal cylinder in cross-flow with heating from below. *International Journal of Heat and Fluid Flow*, 28:454–468, 2007.

[62] G.M. Laskowski, S.P. Kearney, G. Evans, and R. Greif. Mixed convection heat transfer to and from a horizontal cylinder in cross-flow with heating from below. *International Journal of Heat and Fluid Flow*, 28:454–468, 2007.

[63] B. E. Launder. On the computation of convective heat transfer in complex turbulent flows. *Journal of Heat Transfer*, 110, 1988.

[64] E.W. Lemmon, M.O. McLinden, and D.G. Friend. *NIST Standard Reference Database Number 69*, chapter Thermophysical Properties of Fluid Systems. 2013.

[65] A. Leonard. Energy cascade in large eddy simulations of turbulent fluid flow. *Advances in Geophysics*, 18:237–248, 1974.

[66] D. K. Lilly. A proposed modification of the germano subgrid-scale closure method. *Physics of Fluids*, 4:633, 1992.

[67] D. A. Lysenko, I. S. Ertesvag, and K. E. Rian. Large-eddy simulation of the flow over a circular cylinder at reynolds number 3900 using the openfoam toolbox. *Flow Turbulence Combustion*, 89:491–518, 2012.

[68] L. Marocco, A. Loges, T. Wetzel, and R. Stieglitz. Experimental investigation of the turbulent heavy liquid metal heat transfer in the thermal entry region of a vertical annulus with constant heat flux on the inner surface. *International Jouranl of Heat and Mass Transfer*, 55:6435–6445, 2012.

[69] L. Marstorp, G. Brethouwer, O. Grundestam, and A. V. Johansson. Explicit algebraic subgrid stress models with application to rotating channel flow. *Journal of Fluid Mechanics*, 639:403–432, 2009.

[70] K. Matsubara, A. Sakurai, T. Miura, and T. Kawabata. Spanwise heat transport in turbulent channel flow with prandtl numbers ranging from 0.025 to 5.0. *Journal of Heat Transfer*, 134:041701, 2012.

[71] T. W. Mattner. Large-eddy simulations of turbulent mixing layers using the stretched-vortex model. *Journal of Fluid Mechanics*, 671:507–534, 2011.

[72] L. Maudou, G. H. Choueiri, and S. Tavoularis. An experimental study of mixed convection in vertical, open-ended, concentric and eccentric annular channels. *Journal of Heat Transfer*, 135:072502, 2013.

[73] E.R. Meinders and K. Hanjalic. Vortex structure and heat transfer in turbulent fow over a wall-mounted matrix of cubes. *International Jouranl of Heat and Fluid Flow*, 20:255–267, 1999.

[74] Y. Miyake, K. Tsujimoto, and M. Nakaji. Direct numerical simulation of rough-wall heat transfer in a turbulent channel flow. *International Jouranl of Heat and Fluid Flow*, 22: 237–244, 2001.

[75] P. Moin, K. Squires, W. Cabot, and S. Lee. A dynamic subgridscale model for compressible turbulence and scalar transport. *Physics of Fluids*, 3:2746, 1991.

[76] Y. S. Mori. Buoyancy effects on the wake behind a heated obstacle immersed in a turbulent boundary layer. *International Jouranl of Heat and Fluid Flow*, 16:405–416, 1995.

[77] Y. Nagano, H. Hattori, and T. Houra. Dns of velocity and thermal fields in turbulent channel flow with transverse-rib roughness. *International Journal of Heat and Fluid Flow*, 25:393–403, 2004.

[78] J. M. Ndombo and R. J.A. Howard. Large eddy simulation and the effect of the turbulent inlet conditions in the mixing tee. *Nuclear Engineering and Design*, 241:2172–2183, 2011.

[79] D. G. Osborne and F. P. Incropera. Experimental study of mixed convection heat transfer for transitional and turbulent flow between horizontal, parallel plates. *International Jouranl of Heat and Mass Transfer*, 28:1337–1344, 1985.

[80] I. Otic. Direct numerical simulation and rans modeling of turbulent natural convection for low prandtl number fluids. *In Proc. of 5th Inter. Bi-annual ASME/JSME Symp. on comp. technology for fluid/thermal/chemical/stressed systems with industrial appl, San Diego, USA, July 25-29 2004.*, 2004.

[81] I. Otic. One equation subgrid model for liquid metal forced convection. *The 8th International Topical Meeting on Nuclear Reactor Thermal Hydraulics, Operation and Safety (NUTHOS-8) Shanghai, China, October 10-14 2010*, 2010.

[82] J. Pallares and L. Davidson. Large-eddy simulations of turbulent heat transfer in stationary and rotating square ducts. *Physics of Fluids*, 14:2804, 2002.

[83] N. Park, S. Lee, J. Lee, and H. Choi. A dynamic subgrid-scale eddy viscosity model with a global model coefficient. *Physics of Fluids*, 18:125109, 2006.

[84] S. H. Peng and L. Davidson. Large eddy simulation for turbulent buoyant flow in a confined cavity. *International Jouranl of Heat and Fluid Flow*, 22:323–331, 2001.

[85] S. H. Peng and L. Davidson. On a subgrid-scale heat flux model for large eddy simulation of turbulent thermal flow. *International Journal of Heat and Mass Transfer*, 45: 1393–1405, 2002.

[86] U. Piomelli and J. Liu. Large-eddy simulation of rotating channel flows using a localized dynamic model. *Physics of Fluids*, 7:839, 1995.

[87] A. F. Polyakov and S. A. Shindin. Development of turbulent heat transfer over the length of vertical tubes in the presence of mixed air convection. *International Jouranl of Heat and Mass Transfer*, 31:987–992, 1988.

[88] S. B. Pope. *Turbulent Flows*. Cambridge University Press, 2000.

[89] F. Porte-Agel, M. Pahlow, C. Meneveau, and M. B. Parlange. Atmospheric stability effect on subgrid-scale physics for large-eddy simulation. *Advances in Water Resources*, 24: 1085–1102, 2001.

[90] F. Porte-Agel, M. B. Parlange, C. Meneveau, and W. E. Eichinger. A priori field study of the subgrid-scale heat fluxes and dissipation in the atmospheric surface layer. *Journal of the Atmospheric Sciences*, 58:2673–2698, 2001.

[91] P. Poskas, R. Poskas, and A. Sirvydas A. Smaizys. Experimental investigation of opposing mixed convection hear transfer in the vertical flat channel in a laminar-turbulent transition region. *International Jouranl of Heat and Mass Transfer*, 54:662–668, 2011.

[92] D. I. Pullin. A vortex-based model for the subgrid flux of a passive scalar. *Physics of Fluids*, 12:2311, 2000.

[93] A. Rasam, G. Brethouwe, and A. V. Johansson. An explicit algebraic model for the subgrid-scale passive scalar fux. *Journal of Fluid Mechanics*, 721:541–577, 2013.

[94] P. Sagaut. *Large Eddy Simulation for Incompressible Flows*. Springer, 2006.

[95] A. Sakurai, K. Matsubara, K. Takakuwa, and R. Kanbayashi. Radiation effects on mixed turbulent natural and forced convection in a horizontal channel using direct numerical simulation. *International Journal of Heat and Mass Transfer*, 55:2539–2548, 2012.

[96] M. V. Salvetti and S. Banerjee. A priori tests of a new dynamic subgridscale model for finitedifference largeeddy simulations. *Physics of Fluids*, 7:2831, 1995.

[97] H. Schmidt and U. Schumann. Coherent structure of the convective boundary layer derived from large-eddy simulations. *Journal of Fluid Mechanics*, 200:511–562, 1989.

[98] J. Smagorinsky. General circulation experiments with the primitive equations. *Monthly weather review*, 91:99–164, 1963.

[99] B. L. Smith, J. H. Mahaffy, K. Angele, and J. Westin. Report of the oecd/nea-vattenfall t-junction benchmark exercise. Technical report, Paul Scherrer Institute, Switzerland, Wheelsmith Farm, United States, Vattenfall Research and Development, Sweden, Vattenfall Research and Development, Sweden, 2011.

[100] B. L. Smith, J. H. Mahaffy, and K. Angele. A cfd benchmarking exercise based on flow mixing in a t-junction. *Nuclear Engineering and Design*, 264:80–88, 2013.

[101] A. Steiner. On the reverse transition of a turbulent flow under the action of buoyancy forces. *Journal of Fluid Mechanics*, 47:503–512, 1971.

[102] P.P. Sullivan and C.-H. Moeng. An evaluation of the dynamic subgrid scale model in buoyancy driven flows. In *10th Symposium on Turbulence and Diffusion, Portland, OR, American Meteorological Society*, 1992.

[103] H. Suzuki, S. Kid, T. Nakamae, and K. Sutuki. Flow and heat transfer over a backward-facing step with a cylinder mounted near its top cornr. *International Journal of Heat and Fluid Flow*, 12:353–359, 1991.

[104] H. Tanaka, S. Maruyama, and S. Hatano. Combined forced and natural convection heat transfer for upward flow in a uniformly heated, vertical pipe. *International Jouranl of Heat and Mass Transfer*, 30:165–174, 1987.

[105] H. Tennekes and J. L. Lumley. *A first course in turbulence*. The MIT Press, 1972.

[106] A. Tokuhiro and N. Kimura. An experimental investigation on thermal striping mixing phenomena of a vertical non-buoyant jet with two adjacent buoyant jets as measured by ultrasound doppler velocimetry. *Nuclear Engineering and Design*, 188:49–73, 1999.

[107] A. W. Vreman. An eddy-viscosity subgrid-scale model for turbulent shear flow: Algebraic theory and applications. *Physics of Fluids*, 16:3670, 2004.

[108] C. Walker, M. Simiano, R. Zboray, and H.-M. Prasser. Investigations on mixing phenomena in single-phase flow in a t-junction geometry. *Nuclear Engineering and Design*, 239:116–126, 2009.

[109] B. C. Wang, E. Yee, J. Yin, and D. J. Bergstrom. A general dynamic linear tensor-diffusivity subgrid-scale heat flux model for large-eddy simulation of turbulent thermal flows. *Numerical Heat Transfer, Part B*, 51:205–227, 2007.

[110] B. C. Wang, J. Yin, E. Yee, and D. J. Bergstrom. A complete and irreducible dynamic sgs heat-flux modelling based on the strain rate tensor for large-eddy simulation of thermal convection. *International Journal of Heat and Fluid Flow*, 28:1227–1243, 2007.

[111] B. C. Wang, E. Yee, D. J. Bergstrom, and O. Ilda. New dynamic subgrid-scale heat flux models for large-eddy simulation of thermal convection based on the general gradient diffusion hypothesis. *Journal of Fluid Mechanics*, 604:125–163, 2008.

[112] J. Wang, J. Li, and J. D. Jackson. A study of the influence of buoyancy on turbulent flow in a vertical plane passage. *International Jouranl of Heat and Fluid Flow*, 25:420–430, 2004.

[113] Johan Westin, Carsten 't Mannetje, Farid Alavyoon, Pascal Veber, Lars Andersson, Urban Andersson, Jan Eriksson, Mats Henriksson, and Claes Andersson. High-cycle thermal fatigue in mixing tees. large-eddy simulations compared to a new validation experiment, icone16-48731, 16th international conference on nuclear engineering, orlando, florida, usa, may 11-15, 2008. 2008.

[114] D. C. Wilcox. *Turbulence Modeling for CFD*. DCW Industries, Inc., 1994.

[115] V. C. Wong and D. K. Lilly. A comparison of two dynamic subgrid closure methods for turbulent thermal convection. *Physics of Fluids*, 6:1016, 1994.

[116] D. You and P. Moin. A dynamic global-coefficient subgrid-scale eddy-viscosity model for large-eddy simulation in complex geometries. Technical report, Center for Turbulence Research, 2006.

[117] D. You and P. Moin. A dynamic global-coefficient subgrid-scale eddy-viscosity model for large-eddy simulation in complex geometries. *Physics of Fluids*, 19:065110, 2007.

[118] J. You, J. Y. Yoo, and H. Choi. Direct numerical simulation of heated vertical air flows in fully developed turbulent mixed convection. *International Jouranl of Heat and Mass Transfer*, 46:1613–1627, 2003.

[119] Y. Zang, R. L. Street, and J. R. Koseff. A dynamic mixed subgrid-scale model and its application to turbulent recirculating flows. *Physics of Fluids*, 5:3186, 1993.

[120] X. Zhang and S. Dutta. Heat transfer analysis of buoyancy-assisted mixed convection with asymmetric heating conditions. *International Jouranl of Heat and Mass Transfer*, 41:3255–3264, 1997.

[121] F. Zonta and A. Soldati. Effect of temperature dependent fluid properties on heat transfer in turbulent mixed convection. *Journal of Heat Transfer*, 136:022501, 2014.